Springer ThesesRecognizing Outstanding Ph.D. Research

Satoru Ichinokura

Observation of Superconductivity in Epitaxially Grown Atomic Layers

In Situ Electrical Transport Measurements



Springer Theses

Recognizing Outstanding Ph.D. Research

Aims and Scope

The series "Springer Theses" brings together a selection of the very best Ph.D. theses from around the world and across the physical sciences. Nominated and endorsed by two recognized specialists, each published volume has been selected for its scientific excellence and the high impact of its contents for the pertinent field of research. For greater accessibility to non-specialists, the published versions include an extended introduction, as well as a foreword by the student's supervisor explaining the special relevance of the work for the field. As a whole, the series will provide a valuable resource both for newcomers to the research fields described, and for other scientists seeking detailed background information on special questions. Finally, it provides an accredited documentation of the valuable contributions made by today's younger generation of scientists.

Theses are accepted into the series by invited nomination only and must fulfill all of the following criteria

- They must be written in good English.
- The topic should fall within the confines of Chemistry, Physics, Earth Sciences, Engineering and related interdisciplinary fields such as Materials, Nanoscience, Chemical Engineering, Complex Systems and Biophysics.
- The work reported in the thesis must represent a significant scientific advance.
- If the thesis includes previously published material, permission to reproduce this must be gained from the respective copyright holder.
- They must have been examined and passed during the 12 months prior to nomination.
- Each thesis should include a foreword by the supervisor outlining the significance of its content.
- The theses should have a clearly defined structure including an introduction accessible to scientists not expert in that particular field.

More information about this series at http://www.springer.com/series/8790

Satoru Ichinokura

Observation of Superconductivity in Epitaxially Grown Atomic Layers

In Situ Electrical Transport Measurements

Doctoral Thesis accepted by the University of Tokyo, Tokyo, Japan



Author
Dr. Satoru Ichinokura
The University of Tokyo
Tokyo
Japan

Supervisor Prof. Shuji Hasegawa The University of Tokyo Tokyo Japan

ISSN 2190-5053 ISSN 2190-5061 (electronic) Springer Theses ISBN 978-981-10-6852-2 ISBN 978-981-10-6853-9 (eBook) https://doi.org/10.1007/978-981-10-6853-9

Library of Congress Control Number: 2017955257

© Springer Nature Singapore Pte Ltd. 2018

This work is subject to copyright. All rights are reserved by the Publisher, whether the whole or part of the material is concerned, specifically the rights of translation, reprinting, reuse of illustrations, recitation, broadcasting, reproduction on microfilms or in any other physical way, and transmission or information storage and retrieval, electronic adaptation, computer software, or by similar or dissimilar methodology now known or hereafter developed.

The use of general descriptive names, registered names, trademarks, service marks, etc. in this publication does not imply, even in the absence of a specific statement, that such names are exempt from the relevant protective laws and regulations and therefore free for general use.

The publisher, the authors and the editors are safe to assume that the advice and information in this book are believed to be true and accurate at the date of publication. Neither the publisher nor the authors or the editors give a warranty, express or implied, with respect to the material contained herein or for any errors or omissions that may have been made. The publisher remains neutral with regard to jurisdictional claims in published maps and institutional affiliations.

Printed on acid-free paper

This Springer imprint is published by Springer Nature
The registered company is Springer Nature Singapore Pte Ltd.
The registered company address is: 152 Beach Road, #21-01/04 Gateway East, Singapore 189721, Singapore



Supervisor's Foreword

It is my great pleasure and honor to deliver Foreword for the present monograph which is Doctor Thesis of Dr. Satoru Ichinokura, one of my former students. His thesis reports the first observations of superconductivity in three different kinds of materials having one- or two-atomic-layer thickness, the thinnest superconductors ever found. Such atomic-layer superconductivity has attracted considerable interest since 2010 as a different stream of research from bulk superconducting materials. It can provide fertile soil of physics due to large fluctuation, symmetry breaking, controllability, influence of the substrates, and so on. This book involves a historical overview of physics of surface electronic systems on crystals and two-dimensional superconductivity of granular thin films, which meet with other to produce the new field of atomic-layer superconductivity.

The material systems studied in his thesis are divided into two categories: metal atomic layers on a silicon surface and metal-intercalated bilayer graphene on a silicon carbide surface. The former is the first example of coexistence of giant Rashba effect and superconductivity which may result in the so-called parity-broken superconductivity. This means that heavy-element metals adsorbed onto semiconductor surfaces should be a novel platform for unconventional superconductivity, which is a counterpart of superconductivity in non-centrosymmetric bulk crystals. The latter material studied in this thesis is related to the most intensively studied two-dimensional material around the world, graphene. Graphene has been clarified to have various extraordinary electronic properties though the superconductivity is absent until now. The present study is the first direct observation of the superconductivity in a well-defined bilayer graphene, which represents a landmark in this direction of research.

The present thesis is based on the state-of-the-art experimental techniques of in situ measurements and sample preparation in ultrahigh vacuum (UHV), especially in situ four-point probe resistance measurements down to lower than 1K under magnetic field in UHV, combined with molecular beam epitaxy and electron diffraction capability. This kind of surface science techniques is essential for the

present study of well-defined samples; the samples are easily oxidized and destroyed in an ambient condition. I believe that Dr. Ichinokura's thesis opened up a new stage in surface science, which expands the forefront of condensed matter physics.

Tokyo, Japan May 2017 Prof. Shuji Hasegawa

Preface

Two-dimensional superconductivity (2DSC) has been studied for a long time. In 1980's, 2DSC was experimentally demonstrated in amorphous thin films, for the sake of fundamental physics, e.g., superconductor-insulator transitions and the Berezinskii-Kosterlitz-Thouless transition. Although they are important as two-dimensional physics, it is difficult to grow into engineering field because the characteristics of the material were almost absent from the superconducting properties. Recently, however, 2DSC is attracting renewed interest not only as condensed matter physics but as material science since it becomes possible to grow single-crystal-like epitaxial films even in one-atomic-layer thickness owing to the state-of-the-art ultraclean surface preparation methods, promising for the engineering capability based on band structures of the materials. Actually, in such ultrathin 2DSCs, it has been demonstrated experimentally that interfacial effect and breaking symmetry cause remarkable enhancement of critical temperature and magnetic field. In this thesis, they are called "atomic thick superconductors" (ATSCs) to be distinguished from conventional metallic thin films, which aims to expand this frontier by finding novel ATSCs using the combination of molecular beam epitaxy and in situ electrical transport measurement in an ultrahigh vacuum chamber.

This idea is described in Chap. 1 in detail with a historical overview of superconductivity and the electronic structure of two-dimensional materials. Their theoretical background is explained in the next chapter. Chapter 3 is devoted to showing the principle and actual setup of the experiments. Thereafter, the thesis moves its focus onto the implemented experiments. Chapters 4, 5, 6 are based on the results published in the peer-reviewed journals as follows:

Chapter 4 Thallium Biatomic Layer 2D Materials4, 025020 (2017).
Chapter 5 Thallium-lead Monatomic-layer Compound Phys. Rev. Lett.115, 147003 (2015).
Chapter 6 Intercalation Compounds of Bilayer Graphene ACS nano10, 2761–2765 (2016).

x Preface

These articles are reedited to include unpublished data and consideration, with inclusive discussion given in Chap. 7. At the end of the chapter, I comment on the directions for future research based on the current work. I would feel amply rewarded for my efforts if this book becomes a piece of human knowledge and serve as an aid to social progress.

Tokyo, Japan March 2017 Dr. Satoru Ichinokura

List of Published Articles

Parts of the thesis have been published in the following journal articles:

- "Superconductivity in thallium double atomic layer and transition into an insulating phase intermediated by a quantum metal state" S. Ichinokura, L. Bondarenko, A. Tupchaya, D. Gruznev, A. Zotov, A. Saranin, and S. Hasegawa: 2D Materials 4, 025020 (2017).
- "Two-dimensional superconductor with giant Rashba effect: One-atomic-layer Tl-Pb compound on Si(111)" A.V. Matetskiy, S. Ichinokura, L.V. Bondarenko, A. Y. Tupchaya, D.V. Gruznev, A.V. Zotov, A.A. Saranin, R. Hobara, A. Takayama, and S. Hasegawa: Physical Review Letters 115, 147003 (2015).
- 3. "Superconducting Calcium-Intercalated Bilayer Graphene" S. Ichinokura, K. Sugawara, A. Takayama, T. Takahashi and S. Hasegawa: ACS nano 10, 2761–2765 (2016).

Acknowledgements

Since I have ever achieved anything worthwhile without help, I would like to thank with the following lines all the people who made this thesis possible and supported my studies.

Professor Shuji Hasegawa accepted me so kindly, even though I was moved from another university without any knowledge about surface science. I appreciate and admire all the time his inspiration, sage advice, and steady motivation, which encouraged me every day. I will never forget his dedication to academic community and education.

The free- and open-minded culture in Hasegawa Laboratory, providing me a lot of curiosity and comfort throughout my student life, was created by the following kind people. Professor Toru Hirahara was the first assistant professor who guided me in the laboratory. He taught me the importance of fundamental and simple idea of physics as well as conscious of the cutting edge of the research to spend daily experimental studies. Mr. Rei Hobara always pleasantly accepted my question about the experimental technique. He devoted himself to any co-working with other students and researchers, which really surprised and impressed me. Professor Akari Takayama preached the difficulty in carrying out the experimental research projects and gave me an opportunity to review my attitude to the experiments. Professor Ryota Akiyama assisted me calmly even if I got frustrated and gave invaluable advice for continuing my research prospectively. Ms. Kyoko Tanaka dealt with daily administrative procedures as a secretary. She came to our laboratory without any hesitation and assisted all members individually. All the postdocs and students I met were so friendly and clever, giving me abundant knowledge and joy: Takeyuki Tono, Naoya Fukui, Masahiro Hanaduka, Dong Yoon Shin, Terufusa Shirai, Tomonori Nakamura, Takayuki Kubo, Hirotaka Ishihara, Yukihiro Endo, Di Fan, Ryosuke Nakanishi, Yasunori Takeuchi, Huang Hongrui, Tomi Vuoriheimo, JianLin Wang, Suguru Ito, Ryo Noguchi, Takahiro Hashimoto, and Takao Sangawa.

xiv Acknowledgements

I am also thankful to many other co-workers. Dr. Taku Suzuki at National Institute for Material Sciences helped me a lot through the study of ion scattering spectroscopy. This thesis is based on collaborating works with Prof. Takashi Takahashi, Prof. Katsuaki Sugawara at Tohoku University, and Prof. Alexander Saranin, Dr. Andrey Matetskiy at Institute of Automation and Control Processes FEB RAS. Their kind and invaluable guidance and advice from the sample fabrication to writing the papers were essential to complete this thesis. I am also grateful to Prof. Yoshiro Hirayama and his colleagues, Prof. Tsuyoshi Hatano, Prof. Wataru Izumida, and Mr. Katsumi Nagase for their great supervision in my master's course. The article on quantum point contacts is strongly supporting my career.

For the publication of this thesis, I really appreciate the staffs of Springer Japan, especially Dr. Akiyuki Tokuno and Ms. Taeko Sato. I was always encouraged by their lot of kind and patient support through the editorial process.

Finally, I would like to express my gratitude to the friends I met through the life and of course to my parents, who gave me a birthday same as Nicola Tesla and the first liquefaction of helium, by Kamerlingh Onnes!

Contents

1	Introduction				
	1.1	Histor	rical Background	1	
		1.1.1	Two-Dimensional Electron Systems	1	
		1.1.2	Surface Superstructures	2	
		1.1.3	Superconductivity	4	
		1.1.4	Two-Dimensional Superconductivity	5	
		1.1.5	Superconductivity in Surface States	7	
		1.1.6	Atomic Thick Superconductors	9	
	1.2	Direct	ion of This Study	11	
	1.3	Struct	ure of This Thesis	12	
	Refe	erences		12	
2	Fun	damen	tals	15	
-	2.1		the Electronic States and Spatial Inversion Symmetry	15	
	2.1	2.1.1		16	
	2.2		ical Transport	18	
		2.2.1	Drude Model	18	
		2.2.2	Boltzmann Equation	18	
		2.2.3	Matthiessen's Low	20	
		2.2.4	Loffe-Regel Limit	21	
	2.3	Basic	Properties of Superconductivity	21	
		2.3.1	London Equation	22	
		2.3.2	GL Theory	24	
		2.3.3	BCS Theory	30	
		2.3.4	Josephson Effect and Critical Current	40	
	2.4	Specia	al Cases of Superconductivity	41	
		2.4.1	Strong Coupled Superconductor	41	
		2.4.2	Two-Dimensional Superconductivity	43	
		2.4.3	Disorder-Induced Superconductor-Insulator Transition	46	
		2.4.4	Superconductivity Without Spatial Inversion Symmetry	47	

xvi Contents

	Refe	References				
3	3.1 3.2 3.3	Electrical Transport Measurement				
4	4.1 4.2 4.3 4.4	Background Structural Properties of Si(111)-6 × 6-Tl 4.2.1 Atomic Arrangement 4.2.2 Electronic Structure Purpose of This Study Electrical Transport Studies on Si(111)-6 × 6-Tl 4.4.1 Sample Preparation 4.4.2 Results 4.4.3 Discussion Summary rences	63 64 64 65 67 68 68 69 74 76			
5		Background	79 79 80 80 80 83 84 84 85			
	5.5 Refe	Summary	90 90			
6	Inte 6.1	Background	93 93 94 96			
	6.3 6.4	6.2.1 Graphene on SiC	98 98 102 104			

Contents xvii

		6.4.1	Sample Preparation	104				
		6.4.2	Results on Pristine Bilayer Graphene					
		6.4.3	Results on C_6LiC_6 and C_6CaC_6					
		6.4.4	Discussion					
			ary	112				
	····							
7	Conclusion							
	7.1	Genera	al Statement	115				
		7.1.1	Electronic Structure and Superconductivity	115				
			Two-Dimensionality					
	7.2		ok					
	References							
Cu	Curriculum Vitae							

Abbreviations and Constants

1D, 2D, 3D One-, two-, three-dimensional (dimension(s))

AL Aslamazov–Larkin

ARPES Angle-resolved photoemission spectroscopy

AT Atomic thick

BCS Bardeen–Cooper–Schrieffer
BKT Berezinskii–Kosterlitz–Thouless

BL Bilayer

CDW Charge density wave ES Electron system

FFLO Fulde-Ferrell-Larkin-Ovchinnikov

GL Ginzburg-Landau JJ Josephson junction

LEED Low-energy electron diffraction MBE Molecular beam epitaxy

MT Maki-Thompson

RHEED Reflection high-energy electron diffraction SC Superconductor (superconductivity)
SIT Superconductor-insulator transition

SL Single layer(ed)
SOC Spin-orbit coupling

STM Scanning tunneling microscopy (microscope)

STS Scanning tunneling spectroscopy

UHV Ultrahigh vacuum Elemental charge $e = 1.6 \times 10^{-19} \text{ C}$

Electron mass $m_e = 9.11 \times 10^{-31} \text{ kg} = 5.69 \times 10^{-12} \text{ eV} \cdot \text{s}^2/\text{m}^2 =$

511 MeV/c²

Plank constant $h = 4.14 \times 10^{-15} \text{ eV} \cdot \text{s}$

Dirac constant Boltzmann constant Magnetic flux quantum von Klitzing constant

$$\begin{split} \hbar &= h/2\pi = 6.58 \times 10^{-16} \; \mathrm{eV \cdot s} \\ k_B &= 8.62 \times 10^{-5} \; \; \mathrm{eV/K} \\ \phi_0 &= h/2e = 2.07 \times 10^{-15} \; \; \mathrm{Wb} \\ h/e^2 &= 25.8 \mathrm{k}\Omega \end{split}$$

Chapter 1 Introduction

Abstract This study aims to develop a kind of interdisciplinary field. The discoveries of "atomic thick superconductors", which are ultimately thin two-dimensional superconductors with well-defined atomic arrangements, are owing to technical development of the surface science: integration of the four-terminal measurement into the low-temperature and ultrahigh vacuum environment. Their properties can be understood by knowledge accumulated through the long research of superconductivity in bulk and thin film. In this chapter, first, by looking back of the history of the surface science and superconductivity, the substance of the present research field is definitised. Next, remarkable examples of the latest atomic thick superconductors are listed, which motivated this study as described at the end of this chapter.

Keywords Two-dimensional · Surface · Superconductivity

1.1 Historical Background

1.1.1 Two-Dimensional Electron Systems

In the two-dimensional systems, the electrons *always* localize in the presence of random potential—this is a consequence of a scaling theory by Abraham et al. 1979 [1]. For cleaner two-dimensional electron systems (2DES), their scaling theory expected a precursor of localization, described as "weak localization" later [2]. Since the weak localization is originated from the interference of time-reversal-symmetric backscattering paths, it is suppressed by application of the magnetic field. The theory of weak localization explained the negative magnetoresistance, which had been observed by Kawaguchi et al. [3, 4]. It was extended to the system with strong spin-orbit coupling (SOC) by Hikami-Larkin-Nagaoka, which resulted in the occurrence of weak *anti* localization [5]. In particular, the quantum Hall effect (QHE) [6] was the most striking because it was revealed to be an universal phenomenon for every two-dimensional system. Since the discovery of the QHE in 1980, people have noticed the amazing connection between *the topology and the electron physics*.

1

These phenomena were found at artificial 2DESs engineered in semiconductors. In 2004, however, a novel kind of two-dimensional system, *graphene* was discovered. It is the first example of not only a single atomic sheet material but a *Dirac electron system*, which shows insane electric properties, such as half integer QHE etc. [7–12]. The discovery of graphene stimulated enormous number of theoretical studies, including proposal of SOC induced Dirac material, topological insulator. Electrical transport properties including not only the QHE but also weak (anti) localization tell us deeper insite of them [13].

Looking back the technical history, these physics in 2DES was supported by development of crystal growth technique of semiconductor. Molecular beam epitaxy (MBE) makes it possible to fabricate atomically flat hetero junctions, e.g. GaAs/AlGaAs, where electron mobility exceeds 10⁶ cm/Vs [14]. Such interfaces are applied to microdevices like HEMT (high electron mobility transister), one of the important masterpieces of nanoscale engineering. The ordinal Si-FET (field effect transistor) also has miniturized for the desire to increase switching speeds and reduce energy consumption. Due to the drastic reduction of its size, *surface* of semiconductor has more and more important meaning in the context of electrical properties different from bulk and morphological information for developing crystal growth.

1.1.2 Surface Superstructures

In the bulk crystal of semiconductor, each atom has covalent bonds with next neighbor atoms. At the surface, on the other hand, the translational symmetry along the surface normal is broken and there are many lone pairs called dangling bonds arising from the breaking of bonds. This is a very unstable situation energetically and sometimes a reconstruction or a relaxation occurs so as to minimize the number of dangling bonds and the cohesive energy. This is particularly found on semiconductor surfaces forming superstructure whose periodicity is different from that of the bulk. In addition to superstructures formed on clean surfaces, more than 300 kinds of "adsorbate-induced surface superstructures" have been found on silicon [15]. The electronic structure is also different in line with the change in geometrical structure. Namely, there exist states called surface states that are two-dimensional and have wave functions localized at the surface. Since the surface state is novel 2DES, which is totally different from inversion layer or heterojunction, it has been one of the most important topics in the surface science for these three decades. Curiosity for the surface, which is very easy to be contaminated in the air, have been promoted invention of various surface sensitive tools, e.g. scanning probe microscopies/spectroscopies (SPM/Ss) and photoemission spectoroscopies (PESs), that work in ultrahigh vacuum (UHV) environment. The former tells us the atomic arrangements while the latter electron states, directly. Recently, development of PES makes it possible to direct mapping of band dispersion by the angle-resolved photoemission spectroscopy (ARPES).

The Rashba effect, one of the most dramatic phenomena on semiconductor surface was discovered by improvement in resolution of ARPES. The Rashba effect is

spin-spliting of band due to strong spin-orbit coupling and loss of space-inversion symmetry at the surface. Resulting spin texture becomes so complicated one, where both direction and magnitude of spin splitting depend on wavenumber vecter. In particular, heavy-element-adsorbed semiconductor surfaces often have strong Rashba effect. For instance, a giant spin splitting of 270 meV has been found on Ge(111)- $\sqrt{3} \times \sqrt{3}$ -Bi [16]. However, this surface state has *no* Fermi surface, namely, *insulating band* similar to many of other semiconductor surfaces with the Rashba effect. However, Ge(111)- $\sqrt{3} \times \sqrt{3}$ -Pb is the exception, which has metallic surface state with Rashba spin splitting of 200 meV [17] (Fig. 1.1a).

Thus, it is revearled that the surface of solid has its own atomic arrangement and electronic state, that are different from bulk, i.e. unique microscopic properties. *Macroscopic properties*, on the other hand, pecular for the surface states had been unexplored until the invention of the in situ electrical transport measurement technique in UHV. Since it is impossible to fix electrical contacts to MBE-grown samples without exposing them to air, movable tips like micro-four-point-probe (μ 4PP, shown in Fig. 1.1b) directly touch on the surface and act as electrodes in UHV [18]. This μ 4PP method has applied to measure conductivity on a lot of metal-induced reconstructions on Si(111) surface. However, many of them exhibit insulating behavior, where conductivities decrease with cooling even though the surfaces have metallic electronic state. It is unavoidable for metal-adsorbed surfaces to have defects due

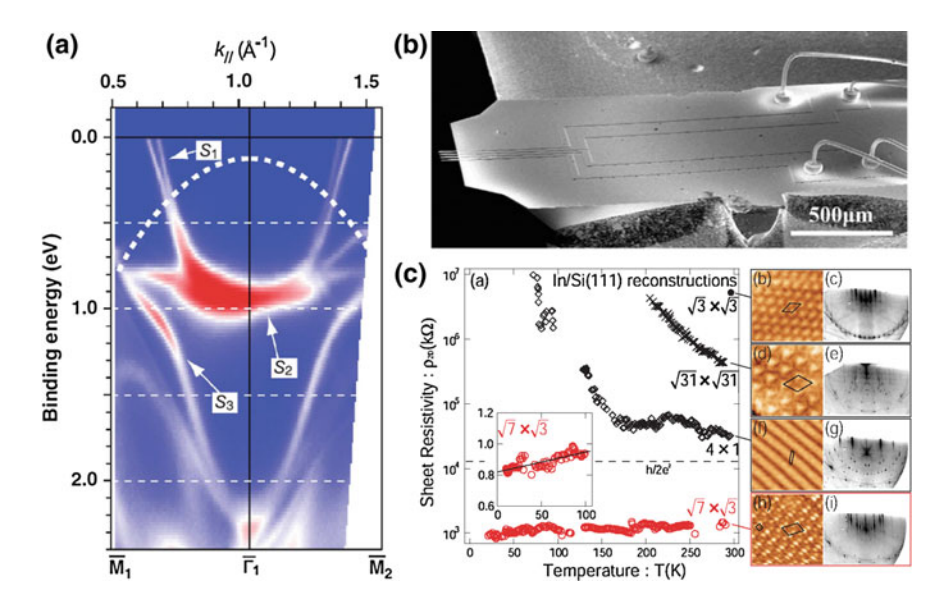


Fig. 1.1 a Band dispersion of Ge(111)- $\sqrt{3} \times \sqrt{3}$ -Pb obtained by an ARPES experiment [17]. b SEM image of the monolithic micro four-point probe [64]. c Temperature dependent sheet resistivities on different four kinds of indium-induced surface reconstruction of Si(111) [19]. The right panels display the atomic-resolved STM images and RHEED patterns for the reconstructions. Reprinted with permission from Refs. [17, 19, 64]

to atomic steps of bare surfaces, inhomogeneity of metallic coverages and contaminations from residual gases. Two-dimensional wave functions on surfaces are easy to be localized because of such defects in atomic scale. Si(111) $-\sqrt{7} \times \sqrt{3}$ -In is the first structure showing metallic conduction, where conductivity increases with cooling down to 10 K. This has been found by Yamazaki et al.They investigated transport properties on several In-induced reconstructions on Si(111) as displayed in Fig. 1.1c [19]. The electrical conductivities significantly varied over several orders for different structures. The electrical transport properties in Si(111) $-\sqrt{7} \times \sqrt{3}$ -In was *quantitatively* consistent to career density, mean free path and electron-phonon coupling obtained by ARPES. This suggests an advantage of 4PP methods in UHV. Transport properties in fragile materials (like *surfaces*) can be understood based on ARPES-obtained band structures without considering contamination. Thus, physical properties of surface superstructures have been proved by comprehensive studies using scanning tunnelling microscopy (STM), ARPES and electrical transport measurements.

Here, we have a natural question about the ground state of 2DES on surfaces—*Can superconductivity occur in these systems?* As mentioned above, weak localization often dominates transport behavior in 2DESs. In addition, according to Mermin-Wagner's theory, long range order is prohibited in the ideal 2DESs at finite temperature [20]. Surface systems have also been regarded to be unexceptional for a long time.

1.1.3 Superconductivity

Since the discovery by Kamerlingh Onnes [21] in 1911, superconductivity has been the hottest topic in solid state physics. Its significant but insane properties of zero-resistance and perfect diamagnetism had confused theorests for a long time. However, BCS theory by Bardeen–Cooper–Schrieffer solved the problem [22]. According to the basic idea of BCS, superconductivity is regarded as a Bose-Einsutain condensed state. Electrons on Fermi surface form *Cooper pairs* isotropically due to attractive interaction mediated by phonon and act as boson.

The transition temperature grows in accordance with enhancement of electron-phonon coupling, but 30–40 K seemed to be a limit. However, *Cuplates* found by Bednorz and Müller in 1986 opened up a way to higher temperature superconductivity by anisotropic Cooper pairing without phononic origin, namely, exotic superconductivity [23]. After that, critical temperature kept rising up to 133 K, reported in $HgBa_2Ca_2Cu_3O_{8+\delta}$ under ambient pressure [24]. Although they are bulk superconductors, the surface-sensitive techniques have contributed for understanding the mechanism of exotic superconductivity. A good compatibility of STM with cryostat and superconducting magnet makes it possible to image the anisotropies of Cooper pairs [25, 26] and vortex lattices [27] in the superconductors. Since the critical temperature of these materials are in the range of low-temperature ARPESs, anisotropic superconducting gap can be directly observable [28, 29]. In the ARPES-obtained

band dispersions, we can find another sign of many-body interaction. When the gradient of dispersion discontinuously change near the Fermi level, quasi particle is generated by many-body effect such as electron-phonon or electron-electron coupling. We can discuss the origin of pairing by temperature-dependent width of the spectrum near these "kink" structures.

If the crystal is non-centrosymmetric, an exotic superconductivity is expected. In centrosymmetric materials, if the orbital factor of Cooper pair is even (*s- or d-wave*, etc.), the spin factor must be singlet. If the orbital factor is odd (*p-wave*, etc.), the spin factor must be triplet. However, lack of space inversion symmetry (SIS) causes the *mixing* of singlet and triplet, together with remarkable enhancement of critical field [30]. For example, a tetragonal BaNiSn₃ type crystal, CeRhSi₃ belongs to a space group of 14 mm (No. 107) without centrosymmetry [31]. Under high pressure of 26 kbar, the upper critical field along a- and c-axis are 7.5 T and over 20 T, respectively [32]. Even though the relationship between this enhancement and symmetry is still under discussion, relatively large critical fields are reported in other non-centrosymmetric materials [32].

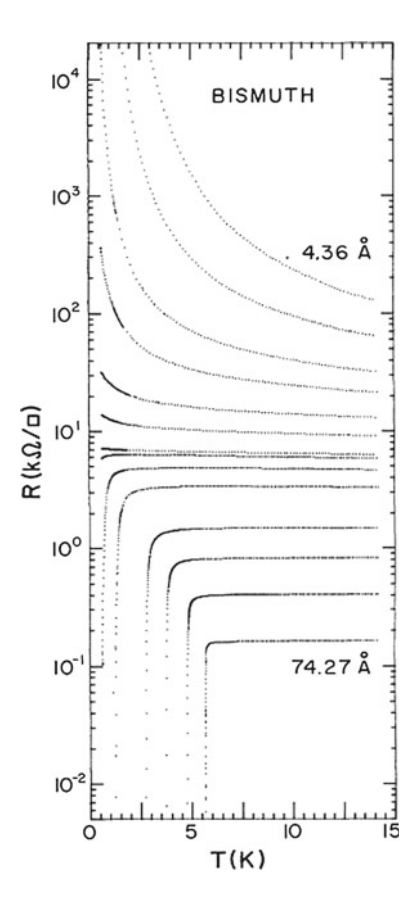
Strong anisotropy often arise from layered structure of the materials such as cuprates. It leads to another important aspect of them—*quasi* two-dimensionality. Behind the huge movement of this so-called high temperature superconductors, investigation for *true* two-dimensionality advanced step by step.

1.1.4 Two-Dimensional Superconductivity

A possible emergence of two-dimensional superconductivity (2DSC) was pointed out by Ginzburg in 1964 [33]. However, they had to wait for experimental verification til 1980s, when it became possible to fabricate metallic thin films with high qualities. Goldman et al.played principal role to establish 2DSC in films thinner than 1 nm. They produced amorphous Bi films by the vapor deposition onto liquid-He-cooled substrates. The substrates were first coated with a wetting layer of Ge, which contributed to remarkable uniformity and homogeneity of the Bi films [34]. Figure 1.2 shows the evolution of R(T) curves with thickness for a Bi film. Onsets of superconductivity, in the form of downturn in R(T) were observed for the films thicker than 6.73 Å. For the thinner films, R(T) shows insulating behavior down to the lowest temperature. Here, the separatrix occurred very close to $h/4e^2 = 6.5 \text{ k}\Omega$, which is the quantised resistance of Cooper pairs. Thus, the separatrix is lower than quantised resistance of normal electron, $h/2e^2$, which is the upper limit where wavenumber loses its meaning as good quantum number. This transition called disorder-induced superconductor-insulator transition (SIT), has attracted much attention as quantum phase transition [35].

Disorder is a spatial fluctuation of electrical potential. Even in clean 2DES, electron feels thermal fluctuation. For the case of 2DSC, both amplitude and phase of order parameter are affected by fluctuations. The former appears as gradual onset of resistance drop of R(T) curve at higher than T_c . On the one hand, the latter appears

Fig. 1.2 Evolution of the temperature dependence of the sheet resistivity with thickness for an amorphous Bi thin film. Film thicknesses shown range from 4.36 to 74.27 Å [34]. The superconductor-insulator transition occurs when the sheet resistivity of the film exceeds $6.45 \text{ k}\Omega$. Reprinted with permission from Ref. [34]



as residual tail of resistance curve slightly below $T_{\rm c}$. This is the problem of long range order in 2DES, pointed by Mermin-Wagner's theorem. Phase fluctuation can be regarded as topological disorder, which causes finite resistance and is reduced at lower temperature than $T_{\rm c}$ in mean field theory. This is a kind of "topological phase transition", proposed by Berezinskii-Kosterlitz-Thouless (BKT). Topology is one of the fundamental idea of modern physics, expecially for two-dimensional one including QHE, etc. [36–40].

Thus, metallic thin films opened up a way to investigate the quantum phase transitions. Since they are general consequence of the dimensionality, they affect every low-dimensional superconductor, including quasi two-dimensional cases in high temperature superconductors like copper oxides. Development of growth technique of oxides leads to another unique 2DSC, *interfacial superconductivity*. Superconductivity at LaAlO₃/SrTiO₃ hetero junction, which was discovered in 2007, is remarkable because 10 nm thick superconducting state locate surround the interface of insulators [41].

Now we have found 2DSC in various kinds of 2D systems—layered quasi two-dimensional crystals, thin films and interfaces. It had been unclear that 2DSC occurs even in *surface states*, until Qin et al. reported superconducting gap in Pb-induced surface reconstructions on Si(111) by ultralow-temperature STM/S below 3.6 K in 2009 [42]. The averaged coverage of Pb on Si(111) was 2 ML (monolayer). Here, ML means density of atoms at the surface [1ML = 7.84×10^{14} /cm² for Si(111)], not directly thickness of Pb because surface reconstructions are very sensitive to coverage of metals. In fact, two periodicity of $\sqrt{3} \times \sqrt{3}$ and $\sqrt{7} \times \sqrt{3}$ existed on 2 ML-Pb-induced Si(111) surface.

1.1.5 Superconductivity in Surface States

In 2010, Zhang et al.reported that uniform Si(111)- $\sqrt{7} \times \sqrt{3}$ -Pb surface exhibits superconductivity below 1.52 K as shown in Fig. 1.3a–c [43]. Since this is a surface structure where 6/5 ML of Pb form a flat layer on Si(111), it is regarded as a first example of superconductivity in single atomic layer. In this paper, superconductivity in Si(111)-SIC-Pb (4/3 ML, $T_c = 1.83$ K, Fig. 1.3d), and $\sqrt{7} \times \sqrt{3}$ -In (6/5 ML, $T_c = 3.18$ K, Fig. 1.3f) were also reported.

Coincidentally, it became possible to cool electrical transport measurement system down to 1 K even in UHV [44, 45]. Transitions to zero-resistance state are reported in Si (111)- $\sqrt{7}$ × $\sqrt{3}$ -In ($T_{\rm c}=2.8$ K, Fig. 1.3f and g) [44] and Si(111)-SIC-Pb ($T_{\rm c}=1.1$ K, Fig. 1.3d and e) [46]. These results indicate the emergence of macroscopic superconductivity even in single atomic layer systems. Yamada et al.pointed that the resistance starts to decrease *above* the superconducting transition temperature without magnetic field (fitting in Fig. 1.3e) due to the fluctuation conductivity in reduced dimensions. On the other hand, Uchihashi et al.discussed "tail" of the resistance drop *below* $T_{\rm c}$ (Fig. 1.3g) [47]. They discussed the origin of this residual resistance in terms of BKT transition. However, they did not conclude that the phase fluctuation is the only factor of the tail because of the possible residual magnetic field in environment.

Thus, it has been shown that superconductivity survives even in the systems with single atomic layer thickness. Now let us move onto next question—do these surface superconductors have something beyond thin films? Superconductivity in metallic induced surface reconstructions was a breakthrough to reach single layer thickness due to their wettability on surface. However, it did not directly connected to discovery of unusual superconductivity; nothing has been found other than BCS superconductors in thin films and no structure has $T_{\rm c}$ higher than bulk counterpart. However, these findings on silicon are regarded as the origin of a new fashion because they were followed by remarkable superconductors in atomic layer systems epitaxial grown on other semiconductor surfaces. In this thesis, these kind of 2DSCs are called atomic thick superconductors (ATSCs).

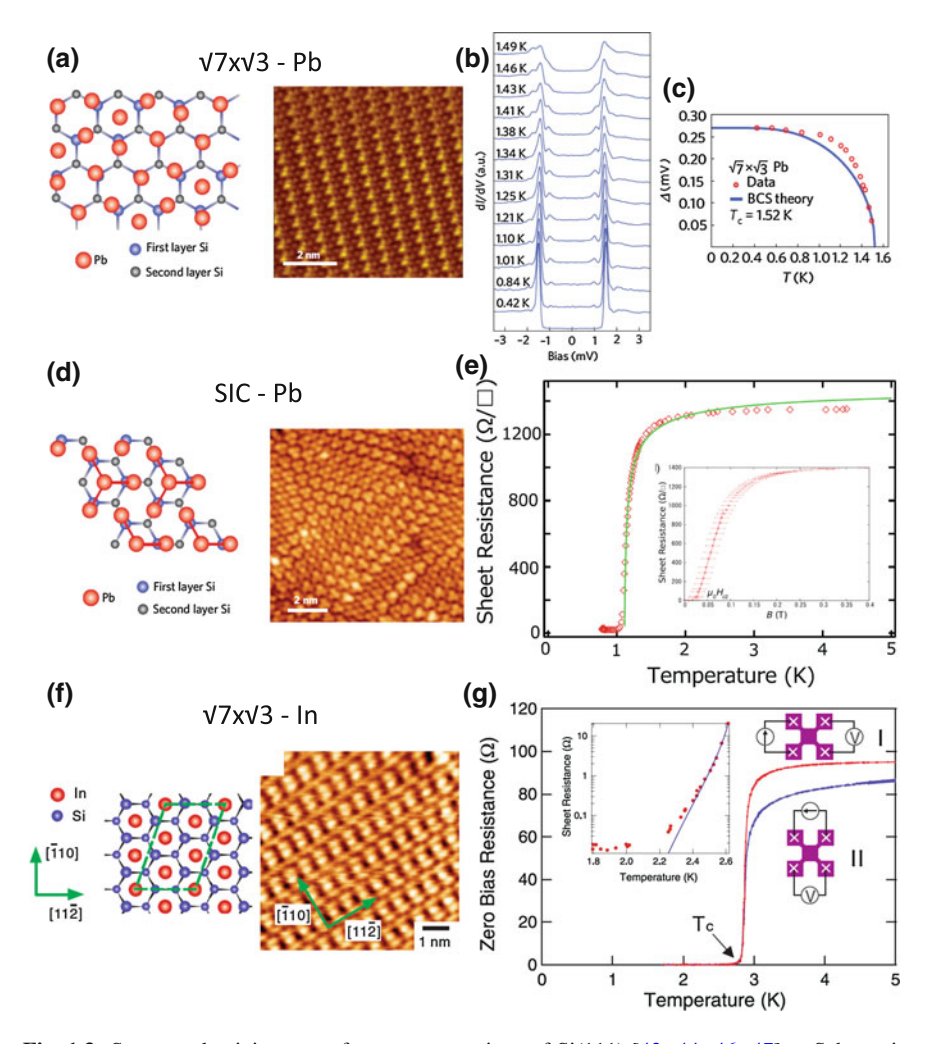


Fig. 1.3 Superconductivity on surface reconstructions of Si(111) [43, 44, 46, 47]. a Schematic structure model and a STM image, b Differential conductance of single-particle tunnelling as a function of temperature and c Superconducting gap as a function of temperature of the $\sqrt{7} \times \sqrt{3}$ -Pb. The open circles show the measured gap, and the solid curve shows the fitting by the BCS gap function [43]. d Schematic structure model and a STM image of the SIC-Pb [43]. e First observation of zero-resistance state of the SIC-Pb in the in situ electrical transport measurement by Yamada et al. [46]. The inset shows the magnetoresistance at low temperature [46]. f Schematic structure model and a STM image of the $\sqrt{7} \times \sqrt{3}$ -In [44], g First observation of zero-resistance state of the $\sqrt{7} \times \sqrt{3}$ -In in the in situ electrical transport measurement by Uchihashi et al. [44]. The insets shows terminal configurations (right) and a close up of a resistance-temperature curve near zero resistance (left) [47]. Reprinted with permission from Refs. [43, 44, 46, 47]

1.1.6 Atomic Thick Superconductors

On GaN substrate, one can grow double or triple layered Ga atomic films, where superconductivity was found by STM and ex citu transport measurements (Fig. 1.4a) [48, 49]. The bilayer Ga film has $T_c = 5.4$ K and the uppercritical field $\mu_0 H_{c2} = 3.3$ T for perpendicular magnetic field, which are larger than those of bulk Ga. Its two-dimensionality is reflected to large $\mu_0 H_{c2}$ of 15 T for magnetic field parallel to the film and thickness of superconducting state (5.5 nm), which is ten times larger than thickness of the Ga bilayer film (0.55 nm). In this example, they deposited Ag on the Ga film at 110 K with a thickness of 80 nm to as a protective and capping layer for the measurement in ambient condition. Since this capping layer does not affect T_c , superconducting state seems to be embedded to the interface of Ga and GaN [48].

Epitaxial growth of layered superconductors with exotic properties is also in progress. In particular, single unit cell films FeSe on SrTiO₃ substrates stimulated large interest in the superconductivity community because of remarkable enhancement of T_c from less than 10 K (in bulk) to more than 60 K [50–56]. According to an in situ electrical transport measurement, T_c can reach 100 K as shown in Fig. 1.4b. The origin of this enhancement is now intensively investigated. It is said that *the interface* between FeSe and SrTiO₃ should play a important role because it induces strain, charge transfer and modification of electron-phonon coupling [57].

These studies opened up a new avenue higher superconducting critical temperature by interface engineering of epitaxial growth. Critical magnetic field, on the other hand, strongly depend on more general idea—symmetry and spin-orbit interaction. Sekihara et al.employed quench condense technique to fabricate Pb film. Although this is a renewal of old method by Goldman et al. [34], but they could thinned the superconducting Pb film down to atomic scale of 2.2 Å on atomically flat surface of cleaved GaAs substrate. They found that the superconductivity is robust against in-plane magnetic field up to 14 T, beyond the Pauli paramagnetic limit (Fig. 1.4c) [58]. As mentioned in Sect. 1.1.3, similar enhancement of $\mu_0 H_{c2}$ has been observed in bulk superconductor without centrosymmetry, i.e. without SIS. This effect become important expecially in the system with strong spin-orbit coupling. Since Pb is heavy element, its ultrathin film on semiconductor meets these requirements. However, it is still unclear that the large $\mu_0 H_{c2}$ is derived from lack of SIS because Rashba spin splitting, which mediates broken SIS and strange magnetic response, has not been confirmed by quantative experiment in this system.

In the context of symmetry-broken 2DSC, single layered (SL-) transition metal dichalcogenides (TMDs) attract much attention. The SL-TMDs are two-dimensional materials which consist of graphene-like hexagonal layers of metal atoms sandwiched between two layers of chalcogen atoms. Since the chalcogen layer is three fold symmetry, an important difference arises between graphene and SL-TMD; *In-plane inversion symmetry is conserved in graphene but not in SL-TMD*. The breaking of symmetry makes graphene-like K and K' valley structures spin splitting. In particular, SL-TMD including heavy elements such as MoS₂, valleys have out-of-plane spin polarization together with strong effective Zeeman fields. While this polarization is

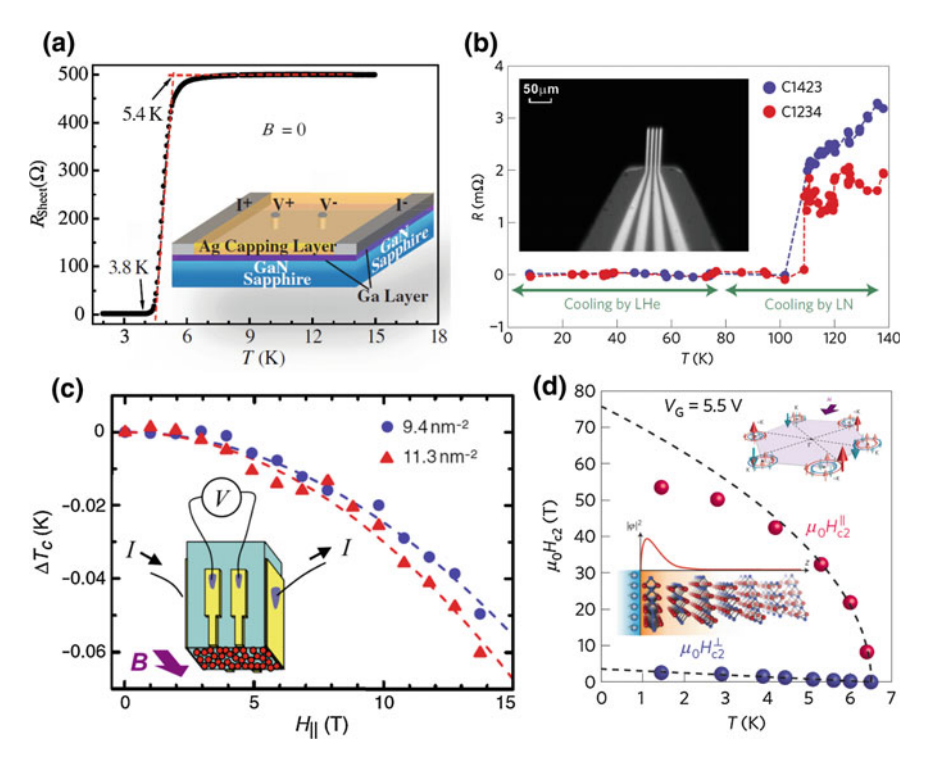


Fig. 1.4 Recent examples of atomic thick superconductors [48, 55, 58, 63]. **a** First observation of zero-resistance on the Ag-capped double atomic layer of Ga grown on the GaN substrate in the *ex situ* electrical transport measurement [48]. The inset shows the schematic illustration of the experimental setting. **b** The temperature-dependent resistance property of the FeSe with one-unit-cell-thickness epitaxially grown on SrTiO₃ obtained by the in situ four-point-probe technique in UHV. One can see a transition to the zero-resistance state above 100 K [55]. The inset shows a SEM image of the micro four-point-probe used in the experiment. **c** In-plane magnetic field dependence of the superconducting transition temperature of Pb ultrathin film which prepared by deposition of 1 ML Pb on GaAs cleavage surface at low temperature and evaluated by in situ electrical transport measurement schematically described in the inset [58]. Even so strong magnetic field of 15T makes the little change in the critical temperature. **d** Temperature dependence of the upper critical magnetic field in the superconducting 2DES in MoS₂ induced by the electrical double layer transister [63]. The upper critical field exceeds 52T for in-plane magnetic field. The insets show a schematic of the Fermi surface (upper) and the distribution of 2DES (lower). Reprinted with permission from Refs. [48, 55, 58, 63]

neutralized in multipul layered TMD, spin and valley degree of freedom are coupled in SL-TMD, leading to the formation of singlet Cooper pairing between the K and K' valleys. Since the direction of spins in a pair are locked by out-of plane spin polarization, the singlet pairs are considered to be robust against external magnetic field. This spin-valley locking effect was demonstrated by Saito et al.. They induced 2DSC in a single crystal of MoS₂ near the surface by electric-double-layer- transistor

technique using ionic liquid [59–63]. The effective 2DSC layer was compressed into 1.5 nm, where $\mu_0 H_{c2}$ is enhanced more than 52 T by the spin-valley locking effect [63].

1.2 Direction of This Study

Thus, since 2010, ATSCs began to attract considerable attention as a new stream of superconductors in the context of broken symmetry and effect of substrates. In other words, the importance of these 2DSCs is *deviation from pure two-dimensionality*.

In this sense, the surface system on the semiconductor is one of the ideal platforms. First, typical semiconductors like silicon and diamond have higher Debye temperature than most of bulk metals. This can raise the critical temperature in metallic overlayer; Cooper pair formation on surface can be mediated by phonon in substrate with high Debye frequency. Second, as mentioned in Sect. 1.1.2, SIS is always broken on surface. Therefore, if the overlayer has strong spin-orbit coupling and metallic band, it is expected to be a non-centrosymmetric superconductor. For instance, heavy-metal adsorbed semiconductor surfaces such as Ge(111)- $\sqrt{3} \times \sqrt{3}$ -Pb shows Rashba effect, which is the direct consequence of spin-orbit coupling and broken SIS and quantitatively evaluated by a state-of-the-art surface sensitive spectroscopy, ARPES. This is a technical advantage of the surface system, compared with bulk materials and amorphous films.

From the viewpoint of material designing, metallic surface overlayer can be regarded as a kind of artificial hetero junction. Recent developing another stream of two-dimensional system is, of course, single layered materials like graphene and TMDs. Their host materials, graphite and some of the bulk TMDs can be superconductivity by intercalating other metals. These systems attract physical attention because of the interplay between charge density wave and superconductivity. Single layered ones are also expected to be superconductivity by doping metals. Such ATSCs is free from substrate, i.e. self-standing ATSCs which have been desired to widen the possibility of architecting devices based with ATSCs.

In this study, in order to establish Rashba-ATSC and self-standing ATSC, transport properties at low temperature are investigated in the following three systems.

- 1. Si(111)-6 \times 6-Tl: Nobel double atomic layer system
- 2. Si(111)- $\sqrt{3} \times \sqrt{3}$ -(Tl, Pb): Monatomic layer compound with Rashba effect
- 3. C₆CaC₆: Ca-intercalated bilayer graphene

This study was conducted as joint researches with Saranin group in Far Eastern Federal University, Vladivostok and Takahashi group in Tohoku university, Sendai. Saranin group provided low-energy electron diffraction (LEED), STM and ARPES data on 6×6 -Tland $\sqrt{3} \times \sqrt{3}$ -(Tl, Pb). Takahashi group supplied bilayer graphene grown on SiC substrate and ARPES data. The data are included in the background section in each chapter from 4 to 6. All of the experimental results summarized in the

result sections were obtained in Hasegawa group in University of tokyo by the author. The author fabricated all the samples and measured/analysed transport properties.

1.3 Structure of This Thesis

In the next chapter (Chap. 2), basic concepts and some formulas needed to understand the main discussion of the thesis is described. Chapter 3 is devoted to show the principle of electron diffraction and transport measurements, together with actual experimental setting. In Chaps. 4 and 5, two different metallic overlayers on Si(111) starting from 1×1 -Tl; 6×6 -Tland $\sqrt{3} \times \sqrt{3}$ -(Tl, Pb)will be presented. The results of transport measurements will be discussed based on the experimentally obtained morphologies and electrical structures. Chapter 6 begins with historical background of carbon superconductor: from graphite to graphene. Recent reports on electrical structures of metal-intercalated bilayer graphene will be presented in detail, in order to discuss the results of transport tests. Finally, overview of these three systems, conclusions and outlooks are given in Chap. 7.

References

- 1. E. Abrahams, P. Anderson, D. Licciardello, T. Ramakrishnan, Phys. Rev. Lett. 42, 673 (1979)
- 2. L.P. Gor'kov, A.I. Larkin, D.E. Khmel'nitskii, JETP Lett. 30, 228 (1979)
- 3. Y. Kawaguchi, H. Kitahara, S. Kawaji, Surf. Sci. 73, 520 (1978)
- 4. Y. Kawaguchi, S. Kawaji, J. Phys. Soc. Jpn. 48, 699 (1980)
- 5. S. Hikami, A.I. Larkin, Y. Nagaoka, Prog. Theor. Phys. **63**, 707 (1980)
- 6. K.v. Klitzing, G. Dorda, M. Pepper, Phys. Rev. Lett. 45, 494 (1980)
- K.S. Novoselov, A.K. Geim, S. Morozov, D. Jiang, Y. Zhang, S. Dubonos, I. Grigorieva, A. Firsov, Science 306, 666 (2004)
- 8. K. Novoselov, A.K. Geim, S. Morozov, D. Jiang, M. Katsnelson, I. Grigorieva, S. Dubonos, A. Firsov, Nature 438, 197 (2005)
- 9. Y. Zhang, Y.W. Tan, H.L. Stormer, P. Kim, Nature 438, 201 (2005)
- K. Novoselov, E. McCann, S. Morozov, V.I. Fal'ko, M. Katsnelson, U. Zeitler, D. Jiang, F. Schedin, A. Geim, Nat. Phys. 2, 177 (2006)
- K.S. Novoselov, Z. Jiang, Y. Zhang, S. Morozov, H. Stormer, U. Zeitler, J. Maan, G. Boebinger, P. Kim, A. Geim, Science 315, 1379 (2007)
- 12. C. Lee, X. Wei, J.W. Kysar, J. Hone, Science 321, 385 (2008)
- 13. Y. Ando, J. Phys. Soc. Jpn. 82, 102001 (2013)
- 14. R. Dingle, H. Störmer, A. Gossard, W. Wiegmann, Appl. Phys. Lett. 33, 665 (1978)
- 15. V.G. Lifshits, A. Saranin, A. Zotov, Surface Phases on Silicon: Preparation, Structures, and Properties (Wiley, New York, 1995)
- 16. S. Hatta, T. Aruga, Y. Ohtsubo, H. Okuyama, Phys. Rev. B 80, 113309 (2009)
- 17. K. Yaji, Y. Ohtsubo, S. Hatta, H. Okuyama, K. Miyamoto, T. Okuda, A. Kimura, H. Namatame, M. Taniguchi, T. Aruga, Nat. Commun. 1, (2010)
- 18. T. Tanikawa, I. Matsuda, T. Kanagawa, S. Hasegawa, Phys. Rev. Lett. 93, 016801 (2004)
- S. Yamazaki, Y. Hosomura, I. Matsuda, R. Hobara, T. Eguchi, Y. Hasegawa, S. Hasegawa, Phys. Rev. Lett. 106, 116802 (2011)

References 13

- 20. N.D. Mermin, H. Wagner, Phys. Rev. Lett. 17, 1133 (1966)
- 21. H.K. Onnes, Commun. Phys. Lab. Univ. Leiden 12, 1 (1911)
- 22. J. Bardeen, L.N. Cooper, J.R. Schrieffer, Phys. Rev. 106, 162 (1957)
- 23. J.G. Bednorz, K.A. Müller, Zeitschrift für Physik B Condensed Matter 64, 189 (1986)
- 24. A. Schilling, M. Cantoni, J. Guo, H. Ott, Nature 363, 56 (1993)
- 25. H. Kambara, Y. Niimi, M. Ishikado, S. Uchida, H. Fukuyama, Phys. Rev. B 76, 052506 (2007)
- 26. S. Pan, E. Hudson, K. Lang, H. Eisaki, S. Uchida, J. Davis, Nature 403, 746 (2000)
- 27. K. Matsuba, H. Sakata, N. Kosugi, H. Nishimori, N. Nishida, J. Phys. Soc. Jpn. 72, 2153 (2003)
- 28. A. Fujimori, E. Takayama-Muromachi, Y. Uchida, B. Okai, Phys. Rev. B 35, 8814 (1987)
- 29. Z.X. Shen, W. Spicer, D. King, D. Dessau, B. Wells, Science **267**, 343 (1995)
- 30. S. Fujimoto, J. Phys. Soc. Jpn. **76**, 051008 (2007)
- N. Kimura, K. Ito, K. Saitoh, Y. Umeda, H. Aoki, T. Terashima, Phys. Rev. Lett. 95, 247004 (2005)
- 32. N. Kimura, K. Ito, H. Aoki, S. Uji, T. Terashima, Phys. Rev. Lett. 98, 197001 (2007)
- 33. V. Ginzburg, Phys. Lett. 13, 101 (1964)
- 34. D. Haviland, Y. Liu, A. Goldman, Phys. Rev. Lett. **62**, 2180 (1989)
- 35. A.M. Goldman, N. Marković, Phys. Today **51**, 39 (1998)
- 36. K. Epstein, A. Goldman, A. Kadin, Phys. Rev. Lett. 47, 534 (1981)
- 37. A. Kadin, K. Epstein, A. Goldman, Phys. Rev. B 27, 6691 (1983)
- 38. A. Fiory, A. Hebard, W. Glaberson, Phys. Rev. B 28, 5075 (1983)
- 39. A. Hebard, A. Fiory, Phys. Rev. Lett. 50, 1603 (1983)
- 40. J. Garland, H.J. Lee, Phys. Rev. B **36**, 3638 (1987)
- N. Reyren, S. Gariglio, A. Caviglia, D. Jaccard, T. Schneider, J. Triscone, Appl. Phys. Lett. 94, 112506 (2009)
- 42. S. Qin, J. Kim, Q. Niu, C.K. Shih, Science **324**, 1314 (2009)
- 43. T. Zhang, P. Cheng, W.J. Li, Y.J. Sun, G. Wang, X.G. Zhu, K. He, L. Wang, X. Ma, X. Chen et al., Nat. Phys. 6, 104 (2010)
- 44. T. Uchihashi, P. Mishra, M. Aono, T. Nakayama, Phys. Rev. Lett. 107, 207001 (2011)
- 45. M. Yamada, T. Hirahara, R. Hobara, S. Hasegawa, H. Mizuno, Y. Miyatake, T. Nagamura, E-J. Surf. Sci. Nanotechnol. **10**, 400 (2012)
- 46. M. Yamada, T. Hirahara, S. Hasegawa, Phys. Rev. Lett. 110, 237001 (2013)
- 47. T. Uchihashi, P. Mishra, T. Nakayama, Nanoscale Res. Lett. 8, 1 (2013)
- 48. H.M. Zhang, Y. Sun, W. Li, J.P. Peng, C.L. Song, Y. Xing, Q. Zhang, J. Guan, Z. Li, Y. Zhao et al., Phys. Rev. Lett. **114**, 107003 (2015)
- 49. Y. Xing, H.M. Zhang, H.L. Fu, H. Liu, Y. Sun, J.P. Peng, F. Wang, X. Lin, X.C. Ma, Q.K. Xue et al., Science **350**, 542 (2015)
- W. Qing-Yan, L. Zhi, Z. Wen-Hao, Z. Zuo-Cheng, Z. Jin-Song, L. Wei, D. Hao, O. Yun-Bo,
 D. Peng, C. Kai et al., Chin. Phys. Lett. 29, 037402 (2012)
- D. Liu, W. Zhang, D. Mou, J. He, Y.B. Ou, Q.Y. Wang, Z. Li, L. Wang, L. Zhao, S. He, et al., Nat. Commun. 3, (2012)
- 52. S. He, J. He, W. Zhang, L. Zhao, D. Liu, X. Liu, D. Mou, Y.B. Ou, Q.Y. Wang, Z. Li et al., Nat. Mater. 12, 605 (2013)
- 53. S. Tan, Y. Zhang, M. Xia, Z. Ye, F. Chen, X. Xie, R. Peng, D. Xu, Q. Fan, H. Xu et al., Nat. Mater. 12, 634 (2013)
- Y. Sun, W. Zhang, Y. Xing, F. Li, Y. Zhao, Z. Xia, L. Wang, X. Ma, Q.K. Xue, J. Wang, Sci. Rep. 4, (2014)
- J.F. Ge, Z.L. Liu, C. Liu, C.L. Gao, D. Qian, Q.K. Xue, Y. Liu, J.F. Jia, Nat. Mater. 14, 285 (2015)
- 56. Y. Miyata, K. Nakayama, K. Sugawara, T. Sato, T. Takahashi, Nat. Mater. 14, 775 (2015)
- 57. L. Wang, X. Ma, Q.K. Xue, Supercond. Sci. Technol. **29**(12), 123001 (2016)
- 58. T. Sekihara, R. Masutomi, T. Okamoto, Phys. Rev. Lett. 111, 057005 (2013)
- K. Ueno, S. Nakamura, H. Shimotani, A. Ohtomo, N. Kimura, T. Nojima, H. Aoki, Y. Iwasa, M. Kawasaki, Nat. Mater. 7, 855 (2008)

 K. Ueno, T. Nojima, S. Yonezawa, M. Kawasaki, Y. Iwasa, Y. Maeno, Phys. Rev. B 89, 020508 (2014)

- 61. W. Shi, J. Ye, Y. Zhang, R. Suzuki, M. Yoshida, J. Miyazaki, N. Inoue, Y. Saito, Y. Iwasa, Sci. Rep. 5, (2015)
- 62. Y. Saito, Y. Kasahara, J. Ye, Y. Iwasa, T. Nojima, Science **350**, 409 (2015)
- 63. Y. Saito, Y. Nakamura, M.S. Bahramy, Y. Kohama, J. Ye, Y. Kasahara, Y. Nakagawa, M. Onga, M. Tokunaga, T. Nojima et al., Nat. Phys. 12, 144 (2015)
- 64. T. Tanikawa, I. Matsuda, R. Hobara, S. Hasegawa, E-J. Surf. Sci. Nanotechnol. 1, 50 (2003)

Chapter 2 Fundamentals

Abstract In this chapter, basic theories are described for interpreting and considering the experimental results obtained in this research. First, the Rashba effect is described because it has an important influence on the physical properties of the electronic state on the surface two-dimensional system. The latter part is devoted to fundamental matters of electron transport and superconductivity, which is the main issue of this research. The section of superconductivity contains the phenomenology, the BCS theory and the ideas of some non-BCS case arised from two-dimensionality.

Keywords Rashba effect · Superconductivity

2.1 Surface Electronic States and Spatial Inversion Symmetry

The surface can be regarded as bulk-cut plane. Hence, at the topmost surface of the covalent crystal, there are many lone pairs called dangling bonds. Dangling bonds are so energetically unstable that sometimes a reconstruction or a relaxation of atomic structure occurs so as to minimize the number of dangling bonds and the total cohesive energy. This make the electronic structure also different one, which is called surface states that are two-dimensional and have wave functions localized at the surface. In particular, novel surface states can be created on semiconductor surfaces by metal adsorption, which rearranges surface structure. Such reconstructed semiconductor surfaces have been one of the main issues of surface science for three decades due to their diversity.

However, there is a so simple difference between surface and bulk; *Symmetry* has a dramatic effect on physical properties of surface. In the bulk material with space inversion symmetry (SIS), $\varepsilon(\mathbf{k},\uparrow)=\varepsilon(-\mathbf{k},\uparrow)$ is required. In addition, $\varepsilon(\mathbf{k},\uparrow)=\varepsilon(-\mathbf{k},\downarrow)$ holds in the presence of time reversal symmetry. These relations lead to $\varepsilon(\mathbf{k},\uparrow)=\varepsilon(\mathbf{k},\downarrow)$, namely, every electronic state should have spin degeneracy. In the system without space inversion symmetry, on the other hand, spin degeneracy can be lifted, i.e. $\varepsilon(\mathbf{k},\uparrow)\neq\varepsilon(\mathbf{k},\downarrow)$. Even for the crystals with centrosymmetry inside,

16 2 Fundamentals

SIS is always broken on the surface. This is why we have spin-related phenemona such as Rashba effect on the surface.

2.1.1 Rashba Effect

Spin splitting arising from broken SIS is important in the system with strong SOC. Hamiltonian of free electron with SOC is described as:

$$\hat{\mathcal{H}} = \hat{\mathcal{H}}_0 + \hat{\mathcal{H}}_{SO} = -\frac{\hbar^2}{2m^*} \nabla^2 + \frac{\hbar}{4m^{*2}c^2} \sigma \cdot (\nabla V \times \mathbf{p}). \tag{2.1}$$

Here, σ is spin operator. In the presence of SIS, average of $\hat{\mathscr{H}}_{SO}$ is zero because $\nabla V=0$. However, once SIS is broken, it effectively acts as magnetic field. For instance, when electron on surface 2DEG has in-plane momentum \mathbf{p} and feels strong confinement potential normal to surface $\nabla V=(0,0,E_{\perp})$, the vector product $\nabla V\times\mathbf{p}$ is parallel to surface and perpendicular to momentum $\mathbf{p}=\hbar\mathbf{k}$ as shown in Fig. 2.1a. Hence, electron spin is quantized and parallel to the effective magnetic field (spin-momentum locking). The magnitude of spin splitting is proportional to $k=|\mathbf{k}|$ so that energy band splits into two blanches depending on its spin state:

$$\varepsilon(k) = \frac{\hbar^2}{2m^*} k^2 \pm \frac{\hbar^2 E_\perp}{4m^{*2}c^2} k = \varepsilon_0(k) \pm \alpha_R k \tag{2.2}$$

Here, $\alpha_R = (\hbar^2 E_\perp)/(4m^{*2}c^2)$ is called Rashba parameter, which is used to indicate the phenomenological magnitude of spin splitting in each material system. Up and down spin states cross at k = 0, namely, they degenerate at k = 0 and the lower energy spin state is reversed depending on the sign of k (Fig. 2.1b).

The surface confinement potential of typical metal is ca. 1 eV, which corresponds to $\alpha_R \sim 10^{-6} \text{eV}$ Å. However, actual crystal surfaces show much larger spin splitting. Au(111) is the first surface system which spin splitting by the Rashba effect is observed [1]. It has a 2D free electron like surface band in the projected bulk band

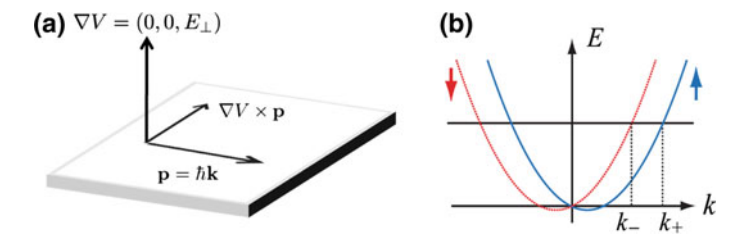


Fig. 2.1 Schematic drawing of (a) a free electron confined in a surface two-dimensional state and (b) the band dispersion of one-dimensional free electron with the Rashba effect

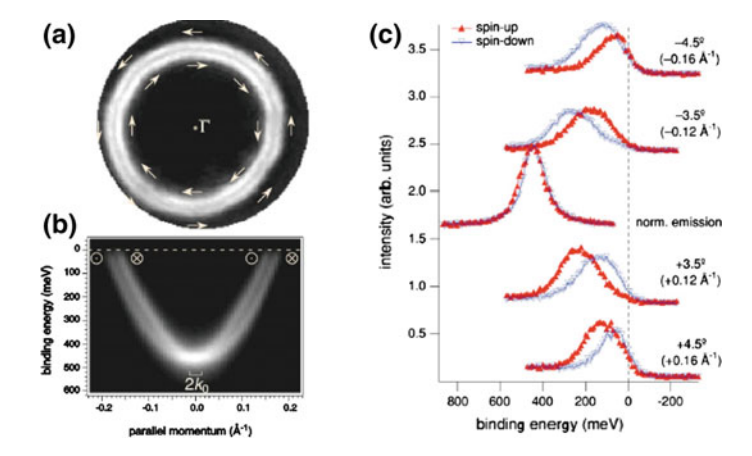


Fig. 2.2 Experimental evidences of the Rashba spin splitting on Au(111) surface provided by ARPES [2]. **a** The Fermi surface, **b** the band dispersion and **c** the spectra of spin-resolved ARPES. Reprinted with permission from Ref. [2]

gap at around $\overline{\varGamma}$ point. Owing to the resolutional improvement of ARPES, La Shell et al. found the surface band is split in accordance with the prediction of the model above. The Rashba parameter estimated by the experiment is $\alpha_R=0.33\,\mathrm{eV}$ Å, larger than the simple estimation above by over orders of magnitude. Since the surface bands of Au(111) is free-electron like, Rashba-type split states are two parabolas shifting in the wavenumber direction (Fig. 2.2b). Consequently, the Fermi contours are observed as two concentric circles as seen in Fig. 2.2a. Spin vector is predicted to rotate in the same direction as the motion along the circles but opposite for different blanch. For the inner branch, the spin rotates in the clockwise direction, while for the outer branch they rotate in the counterclockwise direction. In fact, such spin texture is shown by Hoesch et al. from spin-resolved ARPES measurements (Fig. 2.2c) [2]. Now the idea of the Rashba effect is widely accepted and the surface of crystal is regarded as a model system for it.

Why can surfaces have such large Rashba spin splitting? Peterson et al. calculated the electronic state derived from 6p in the topmost layer of Au(111) surface by tight-binding method including SOC [3]. Their result showed that the Rashba effect is caused by not only breaking symmetry but SOC in the nucleus on surface. This is why magnitude of the Rashba effect depend on atomic numbers of surface elements. Nagano et al. performed *ab initio* calculations for various surfaces, indicating importance of concentration and asymmetry (or distortion) of wavefunction near the surface [4].

These theories tell us the intricate nature of the Rashba effect. Actually, the systems with especially large Rashba splits are surface alloys like Bi/Ag(111) [5], which have more complicated atomic structure than simple metals.

18 2 Fundamentals

2.2 Electrical Transport

In this thesis, superconducting transport properties in two-dimensional systems with metallic state will be discussed. Although superconductivity is carried by Cooper paired electrons, it inherits normal state electronic properties e.g. coupling strength with phonon and mean free path. Such physical quantities are defined here by Drude and Boltzman formulas.

2.2.1 Drude Model

Carrier is driven by electrical field. When a constant force acts on electrons, they show Bloch oscillation in a perfect crystal while steady uniform motion in a natural crystal due to scattering by defects.

Drude constructed a model to describe electron motion in classical sense. In the Drude model, it is assumed that an electron travels for a time τ since its last collision, namely, scattering rate per unit of time is $1/\tau$ in average. The τ is called relaxation time. The equation of motion for an electron under electric field of ${\bf E}$ is

$$m^* \frac{d\mathbf{v}(t)}{dt} = e\mathbf{E} - m^* \frac{\mathbf{v}(t)}{\tau},\tag{2.3}$$

where m^* is electron mass. Then, velocity of electron in steady state is

$$\mathbf{v} = \frac{e\tau}{m^*} \mathbf{E} = \mu \mathbf{E}. \tag{2.4}$$

 $\mu = e\tau/m^*$ is called mobility. Current density of carriers with density of n is

$$\mathbf{j} = ne\mathbf{v} = \frac{ne^2\tau}{m^*}\mathbf{E} = ne\mu\mathbf{E}.$$
 (2.5)

Electrical conductivity σ is defined by $\mathbf{j} = \sigma \mathbf{E}$. From Eq. (2.5),

$$\sigma = \frac{ne^2\tau}{m^*} = ne\mu. \tag{2.6}$$

2.2.2 Boltzmann Equation

Although the Drude model assumes independent motion of electrons in a classical way, the idea of the relaxation time and the mobility can be used to describe macroscopic properties of the real systems. However, in order to estimate conductivity by

quantum mechanical states in solids, we have to use the Boltzmann model. In equilibrium condition, electrons occupy states in energy bands (1, 2, ..., i, j, ...) according to the Fermi distribution function, which is modified by application of the electrical field. By adopting the relaxation time approximation, the distribution function returns to equilibrium after time τ . Then, conductivity tensor σ_{ij} ($j_i = \sigma_{ij} E_j$) can be written as [6]

$$\sigma_{ij} = \frac{2e^2\tau}{(2\pi)^d\hbar} \int dS_F \frac{v_i v_j}{v}.$$
 (2.7)

In two-dimensional case,

$$\sigma_{ij} = \frac{e^2 \tau}{2\pi^2 \hbar} \int dk_F \frac{\nu_i \nu_j}{\nu}.$$
 (2.8)

If current is uniform and isotropic, $v_{i(j)}$ can be rewritten by the Fermi velocity v_F ;

$$\sigma = \frac{e^2 \tau v_F}{4\pi^2 \hbar} \int dk_F. \tag{2.9}$$

In 2D free electron, density of state at the Fermi surface per square unit is

$$N = \frac{1}{2\pi^2} \int \frac{dk_F}{\partial E/\partial k} = \frac{1}{2\pi^2 \hbar} \int \frac{dk_F}{v_F} = \frac{m^*}{\pi \hbar^2}.$$
 (2.10)

Here m^* is the effective mass. Therefore σ is simplified as

$$\sigma = \frac{e^2}{2} l v_F N = \frac{e^2 \tau k_F^2}{2\pi m^*},\tag{2.11}$$

where $l = \tau v_F$ is the mean free path. Using $m^* v_F = \hbar k_F$,

$$\sigma = \frac{e^2}{h} k_F l. \tag{2.12}$$

Hence, we can estimate mean free path from sheet resistivity $R_{\text{sheet}} = 1/\sigma$ as

$$l = \frac{1}{k_F} \cdot \frac{h/e^2}{R_{\text{sheet}}}. (2.13)$$

Namely, the mean free path is proportinal to the Fermi wavelength $1/k_F$ and $1/R_{\text{sheet}}$. $h/e^2 = 25.8 \,\mathrm{k}\Omega$ is the quantized resistance of electron.

Note that the Boltzmann picture results in the Drude model [Eq. (2.6)] by adopting free electron approximation. First,

$$\int dk_F = 2\pi k_F \tag{2.14}$$

$$n = \frac{k_F^2}{2\pi}. (2.15)$$

By using $v_F = \hbar k_F/m^*$, electrical conductivity

$$\sigma = \frac{e^2 \tau n}{m^*} = e \mu n. \tag{2.16}$$

Though the electrical transport occurs only near the Fermi surface, the conductivity involves the total number of electrons occupying the band from the bottom to the Fermi energy, same as the Drude formula.

Conductivity and band structure

Now we can get relations between transport properties and band dispersions based on the Boltzmann picture as follows.

From the Fermi wavenumber k_F and the gradient of band dispersion near the Fermi surface $\partial E/\partial k(k=k_F)$, The Fermi velocity is written as

$$v_F = \frac{1}{\hbar} \left(\frac{\partial E}{\partial k} \right)_{k_E}. \tag{2.17}$$

The effective mass:

$$m^* = \frac{\hbar k_F}{v_F} = \frac{\hbar^2 k_F}{\left(\frac{\partial E}{\partial k}\right)_{k_F}} \tag{2.18}$$

On the one hand, the career density n is estimated by

$$n = \frac{\text{spin degeneracy factor} \times \text{area of the Fermi surface}}{(2\pi)^2}.$$
 (2.19)

2.2.3 Matthiessen's Low

In a solid, the electron repeatedly scatters off crystal defects, phonons, impurities, etc. According to the Matthiessen's low, the inverse of the relaxation time τ (scattering probability) is the sum of that from electron-phonon coupling, electron-electron interaction, and impurity scattering $(\tau_{e-p}, \tau_{e-e}, \tau_{imp})$.

$$\frac{1}{\tau} = \frac{1}{\tau_{e-p}} + \frac{1}{\tau_{e-e}} + \frac{1}{\tau_{imp}}.$$
 (2.20)

Here R_{sheet} is defined as the sheet resistance, the inverse of Eq. (2.11). Applying the Matthiessen's low.

$$R_{\text{sheet}} = \frac{2\pi m^*}{e^2 k_F^2} \left(\frac{1}{\tau_{e-p}} + \frac{1}{\tau_{e-e}} + \frac{1}{\tau_{imp}} \right). \tag{2.21}$$

At the temperature much lower than Debye temperature, the contributions from electron-electron interaction and impurity scattering are dominant. Since electron-electron scattering does not frequently occur in normal metals, resistance decrease with cooling, saturating in residual resistance due to impurity. Such monotonic behavior is broken by several reasons: Kondo effect, Mott transition and Anderson localization.

2.2.4 Loffe-Regel Limit

Anderson localization is understood as the absence of diffusion of electrons in a crystal due to too many impurities. Namely, the Bloch picture itself is destroyed by strong randomness. Bloch wave spreads thorough the system when the mean free path is enough longer than the Fermi wavelength;

$$k_F l > 1. (2.22)$$

Equation (2.13) gives us a relation

$$R_{\text{sheet}} < \frac{h}{e^2} = 25.8 \text{ (k}\Omega).$$
 (2.23)

This is what we call *Ioffe-Regel limit*, 25.8 k Ω . Namely, metallic behavior (*monotonic decrease of resistance*) is expected when $R_{\text{sheet}} < 25.8 \, \text{k}\Omega$, unless insulating behavior (*increase of resistance*) or *metal-insulator transition* is predicted.

2.3 Basic Properties of Superconductivity

Many of the metals become superconductivity when cooled below a characteristic critical temperature T_c . There are two elementary properties of superconductors;

- Zero resistance: sustaining currents in superconducting rings with no power source.
- Perfect diamagnetism (Meissner effect): complete ejection of magnetic field lines from the interior of the superconductor.

A superconductor can be Type I, meaning that it has a single critical field H_{c1} , above which Meissner state is completely lost; or Type II, meaning that it has two critical

fields (H_{c1} and H_{c2}), between which it allows partial penetration of the magnetic field. $H_{c1} < H < H_{c2}$ is called mixed state where an increasing amount of magnetic flux penetrates the material, but there remains no resistance to the flow of electric current as long as the current is not too large. Elemental metals such as Hg, Sn and Al are classified in the former case: Type I, while most of the alloys and compounds are Type II.

2.3.1 London Equation

The first phenomenological theory of superconductivity was the London theory [7]. The London theory separates the conducting electrons within a superconductor into two fluids. According to this two-fluid model, one fluid consists of 'normal' electrons with number density n_n , which behave exactly in the same way as the free electrons in a normal metal. The current density $\mathbf{J}_n = n_n e \mathbf{v}_n$ due to flow of these electrons obeys Ohm's low:

$$\mathbf{J}_n = \sigma_n \mathbf{E}. \tag{2.24}$$

The others are the superconducting electrons (or superelectrons), which form a fluid with number density n_s . The superconducting electrons are assumed to be freely accelerated by an electric field i.e. not scattered by impurities, defects or thermal vibrations. When the velocity and charge of a superconducting electron are \mathbf{v}_s and e_s , then its equation of motion is written as

$$\frac{d\mathbf{v}_s}{dt} = -e_s \mathbf{E}.\tag{2.25}$$

Since the expression for the current density is $\mathbf{J}_s = n_s e_s \mathbf{v}_s$, we find that

$$\frac{d\mathbf{J}_s}{dt} = \frac{n_s e_s^2}{m_s} \mathbf{E}.$$
 (2.26)

This is the first formula of London equation. If we consider a constant current flowing in the superconductor, then $d\mathbf{J}_s/dt = 0$, so $\mathbf{E} = 0$ i.e. no electric field or potential difference in the superconductor. This indicates *zero resistance* state.

To account for the Meissner effect in a superconductor, additional assumptions are needed;

$$\nabla \times \mathbf{J}_s = -\frac{n_s e_s^2}{m_s} \mathbf{h}. \tag{2.27}$$

This is the second formula of London equation. Displacement current and normal current decrease so rapidly that can be ignored to consider effect in steady condition. So the Ampère-Maxwell law can be written as $\nabla \times \mathbf{h} = \mu_0 \mathbf{J}_s$. Here, \mathbf{h} is local magnetic field. Taking rotation of both side, we have

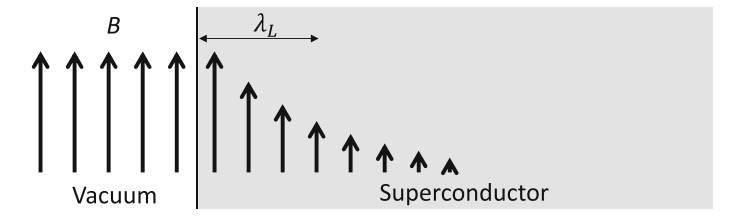


Fig. 2.3 Schematic illustration of the Meissner effect. The magnetic flux density parallel to the surface attenuated exponentially with distance below the surface of the superconductor. The inside of superconductor has perfect diamagnetism

$$\nabla \times (\nabla \times \mathbf{h}) = \mu_0 \nabla \times \mathbf{J}_s. \tag{2.28}$$

Inserting Eq. (2.27) gives us a second-order differential equation of **h**.

$$\nabla^2 \mathbf{h} = \frac{1}{\lambda_L^2} \mathbf{h}. \tag{2.29}$$

Here, we define London penetration depth λ_L by

$$\lambda_L \equiv \sqrt{\frac{m_s}{\mu_0 n_s e_s^2}}. (2.30)$$

By solving Eq. (2.29), we obtain

$$h_{\parallel} \propto \exp\left(-\frac{x}{\lambda_L}\right).$$
 (2.31)

This indicates that the external magnetic field is attenuated exponentially with distance below the surface of the superconductor. $h_{\parallel} \rightarrow 0$ within the bulk; This is qualitative explanation of Meissner effect (see Fig. 2.3).

If Eq. (2.27) is rewritten by vector potential **A** instead of local magnetic field **h**,

$$\mathbf{J}_s = -\frac{n_s e_s^2}{m_s} \mathbf{A}. \tag{2.32}$$

This is another expression of London equation, since Eq. (2.26) is obtained by temporal differentiation of Eq. (2.32). The laws of physics governing electricity and magnetism should be invariant under gauge transformation. Hence, Eq. (2.32) requires a specific gauge as **A**, indicating that the gauge symmetry is broken accompanied with superconducting transition. In superconducting system, $\nabla \cdot \mathbf{J}_s = 0$. Therefore, we have to fix the gauge as following *Coulomb gauge*.

$$\nabla \cdot \mathbf{A} = 0. \tag{2.33}$$

2.3.2 GL Theory

The second order phase transition is accompanied by the spontaneous symmetry breaking. As mentioned above, London equation results in breaking of the gauge symmetry. Actually, superconducting phenomenon is explained as a second order phase transition in the Ginzburg-Landau (GL) theory.

The most typical example of the second order phase transition is magnetization in ferromagnetic materials. Above the Curie temperature, there is no order of spin direction (paramagnetism). Below the Curie temperature, every spin aim to be parallel in specific direction and the system has finite magnetization (ferromagnetism). Although the magnetic order has microscopic origin: exchange interaction with next neighbor spins, it can be described by macroscopic phenomenology using free energy $\mathscr{F}(M,T)$ without detailed mechanism. Here, M is magnetization: a kind of order parameter. In quantum statistical mechanics, Bose-Einstein condensate (BEC) is an example of the spontaneous phase transition. Then, a large fraction of bosons occupy the lowest quantum state called macroscopic wavefunction;

$$\Psi(\mathbf{r}) = |\Psi(\mathbf{r})|e^{-i\Phi}, \tag{2.34}$$

at which macroscopic quantum phenomena become apparent. Here, the gauge symmetry is broken: the phase of macroscopic wavefunction is ordered.

Superconducting order parameter

To treat superconductivity in the same way, Ginzburg and Landau argued that the free energy, \mathscr{F} , of the superconductor near the superconducting transition can be expressed in terms of a complex order parameter field Ψ , which is nonzero below the phase transition into the superconducting state and is related to the density of the superconducting electron n_s ;

$$\Psi = \sqrt{n_s} e^{-i\Phi}. \tag{2.35}$$

Therefore,

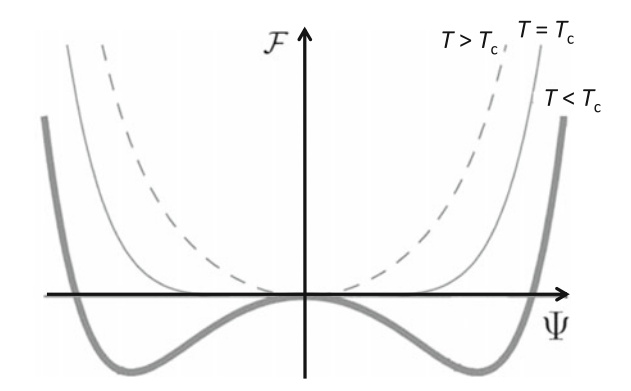
$$|\Psi|^2 = n_s. \tag{2.36}$$

Here, the spatial dependence is ignored for simplification. In the superconducting phase, the gauge symmetry is broken so that the phase of superconducting state has physical meaning. The charge flux density is written in the following form.

$$\mathbf{J}_{s} = \frac{ie_{s}\hbar}{2m_{s}}(\Psi\nabla\Psi^{*} - \Psi^{*}\nabla\Psi) = \frac{e_{s}\hbar}{m_{s}}n_{s}\nabla\Phi. \tag{2.37}$$

This equation indicates that the superconducting current is driven by the phase of macroscopic wavefunction.

Fig. 2.4 Temperature dependence of the free energy $\mathscr{F}(\Psi)$ in Ginzburg-Landau theory. There is an unique minimum at the origin when $T > T_{\rm c}$, while there are two minima when $T > T_{\rm c}$



According to the general discussion of the second order phase transition, the free energy has a form of thr field theory using $|\Psi|^2$ as order parameter.

$$\mathscr{F}[\Psi] = \mathscr{F}_0 + \alpha |\Psi|^2 + \frac{\beta}{2} |\Psi|^4, \qquad (2.38)$$

where $\alpha(T) = a(T - T_c)$ and a, β is positive constant. \mathcal{F}_0 indicates the free energy in normal state. This equation has a trivial solution: $|\Psi| = 0$. This corresponds to the normal state of the superconductor, that is for temperatures above the superconducting transition temperature, $(T > T_c)$. Below the superconducting transition temperature, the above equation has non-trivial solutions:

$$|\Psi| = \pm \sqrt{\frac{a(T_{\rm c} - T)}{\beta}}.$$
 (2.39)

The temperature dependent behaviors of free energy is summrized in Fig. 2.4. This type is called *Higgs potential*. When $T > T_c$, there is an unique solution at the origin. On the other hand, when $T < T_c$, the mimimums can be solution. This is so-called sponteneous symmetry breaking at $T = T_c$.

GL equation

Here, let us consider the spatial variation in amplitude of macroscopic wavefunction: $\Psi(\mathbf{r}) = |\Psi(\mathbf{r})|e^{-i\Phi}$. By minimizing the free energy with respect to variations in the order parameter and the vector potential, one arrives at the GL equations:

$$-\frac{\hbar^2}{2m_s} \left[\nabla - \frac{ie_s}{\hbar} \mathbf{A}(\mathbf{r}) \right]^2 \Psi(\mathbf{r}) + \alpha \Psi(\mathbf{r}) + \beta |\Psi(\mathbf{r})|^2 \Psi(\mathbf{r}) = 0, \quad (2.40)$$

$$\mathbf{J}_{s}(\mathbf{r}) = \frac{-ie_{s}\hbar}{2m_{s}} \left[\Psi^{*}(\mathbf{r})\nabla\Psi(\mathbf{r}) - \Psi(\mathbf{r})\nabla\Psi^{*}(\mathbf{r}) \right] - \frac{e_{s}^{2}}{m_{s}} |\Psi(\mathbf{r})|^{2} \mathbf{A}(\mathbf{r}). \quad (2.41)$$

When $\mathbf{A}(\mathbf{r}) = 0$, easy solutions can be find: the minimums in Fig. 2.4. $[\nabla - (ie_s/\hbar)\mathbf{A}(\mathbf{r})]\Psi(\mathbf{r}) = 0$ in Eq. (2.40) also gives solutions with the same energy.

Next, by considering the spatial variation of phase $\Psi(\mathbf{r}) = |\Psi(\mathbf{r})|e^{-i\Phi(\mathbf{r})}$, we obtain the following equations.;

$$\nabla |\Psi(\mathbf{r})| = 0, \tag{2.42}$$

$$\nabla \Phi(\mathbf{r}) - \frac{e_s}{\hbar} \mathbf{A}(\mathbf{r}) = 0. \tag{2.43}$$

The former requires $|\Psi(\mathbf{r})|$ to be spatially constant. The latter gives a relation between vector potential \mathbf{A} and $\Phi(\mathbf{r})$ as

$$\mathbf{A}(\mathbf{r}) = \frac{\hbar}{e_s} \nabla \Phi(\mathbf{r}). \tag{2.44}$$

Here, arbitrary $\mathbf{A}(\mathbf{r})$ satisfying the Eq. (2.33) (Coulomb gauge) is possible. Namely, the solution of GL equation (2.40) infinitely degenerates with respect to the phase of macroscopic wavefunction. The ground state Ψ is given by Higgs potential curve shown in Fig. 2.4. The phase degree of freedom of Ψ corresponds to rotation in complex plane $[\text{Re}(\Psi), \text{Im}(\Psi)]$ (indicated by the white arrow in Fig. 2.5). Therefore, Higgs potential form symmetrical upward dome with a trough circling the bottom in $[\text{Re}(\Psi), \text{Im}(\Psi), F]$ as shown in Fig. 2.5. At high temperature phase, the solution locates at the peak of this "Mexican hat", and the system is rotational symmetric, corresponding to conservation of gauge symmetry. Phase transition from this symmetric state to low-temperature phase is regarded as rolling down the dome into the trough (indicated by the black arrow in Fig. 2.5), a point of the lowest energy. Afterward, the ball has come to a rest at some fixed point, namely, phase of macroscopic

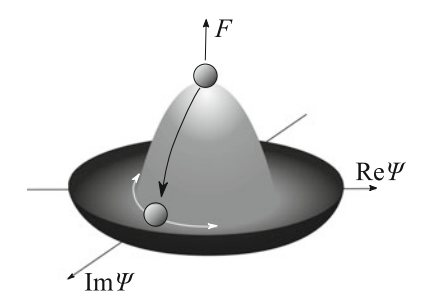


Fig. 2.5 Schematic illustration of the Higgs potential. At high temperature phase, the solution locates at the peak of the dome. Phase transition to low-temperature phase is indicated by the black arrow, rolling down the dome into the trough. The phase degree of freedom of Ψ corresponds to rotation in complex plane $[Re(\Psi), Im(\Psi)]$, which is indicated by the white arrow

wavefuction is determined. At the point, rotational symmetry is no longer conserved: gauge symmetry is *spontaneously* broken.

GL coherence length

Let us consider the spatial variation of macroscopic quantum state $|\Psi(\mathbf{r})|$ in a specific situation, in which a superconductor occupies x > 0 semi-infinit space. We solve the one dimensional GL equation (2.40)

$$-\frac{\hbar^2}{2m_s}\frac{d^2}{dx^2}\Psi(x) + \alpha\Psi(x) + \beta\Psi^3(x) = 0$$
 (2.45)

with a boundary condition $\Psi(0) = 0$. We can simplify this formula by defining

$$\xi_{\rm GL}^2 \equiv \frac{\hbar^2}{2m_s|\alpha|} \tag{2.46}$$

and a normalization $\psi \equiv \Psi/\Psi_0$, $\Psi_0 = \sqrt{|\alpha|/\beta}$;

$$-\xi_{GL}^2 \frac{d^2}{dx^2} \psi(x) - \psi(x) + \psi^3(x) = 0.$$
 (2.47)

This is rearranged to

$$\frac{d}{dx} \left[-\xi_{GL}^2 \left(\frac{d\psi(x)}{dx} \right)^2 - \psi(x)^2 + \frac{1}{2} \psi^4(x) \right] = 0.$$
 (2.48)

Hence,

$$-\xi_{\rm GL}^2 \left(\frac{d\psi(x)}{dx}\right)^2 - \psi(x)^2 + \frac{1}{2}\psi^4(x) = \text{const.}$$
 (2.49)

At the interior of superconductor, $(x \to +\infty)$, $\Psi \to \Psi_0$. Then,

$$\xi_{\rm GL}^2 \left(\frac{d\psi(x)}{dx}\right)^2 = \frac{1}{2}[1 - \psi^2(x)]^2,$$
 (2.50)

leading to

$$\psi(x) = \tanh\left(\frac{x}{\sqrt{2}\xi_{\text{GI}}}\right). \tag{2.51}$$

Even though $\Psi(0, y, z) = 0$ at the interface, superconducting state recover it equilibrium according to the characteristic exponent ξ_{GL} . It is called *GL coherence length*, which gives the length scale the variations of the density of superconducting component against small perturbations. Using $\alpha = a(T - T_c)$, we obtain

$$\xi_{\rm GL}(T) = \left(\frac{\hbar^2}{2m_s a T_c}\right)^{1/2} \left(1 - \frac{T}{T_c}\right)^{-1/2},\tag{2.52}$$

indicating that GL coherence length depends on temperature and diverges at T_c . By replacing n_s with $|\Psi|^2$ in Eq. (2.30),

$$\lambda_L = \sqrt{\frac{m_s}{\mu_0 |\Psi|^2 e_s^2}} = \left(\frac{m_s \beta}{\mu_0 e_s^2 a T_c}\right)^{1/2} \left(1 - \frac{T}{T_c}\right)^{-1/2}.$$
 (2.53)

Applying Eq. (2.51) gives us

$$\kappa \equiv \frac{\lambda_L}{\xi_{GL}} = \frac{m_s}{e_s \hbar} \sqrt{\frac{2\beta}{\mu_0}}.$$
 (2.54)

Here definded κ is GL parameter which determines classification of superconductor as shown in Fig. 2.6; When $\kappa < 1/\sqrt{2}$, penetration of magnetic flux can be ignored so that the system is type-I. $\kappa > 1/\sqrt{2}$ means that the coherence length is smaller than the penetration depth. This manifests that magnetic flux passing through the material, which is the characteristic of type-II superconductor. Most of the compounds are classified to this case.

Qauntum vortex

Magnetic flux penetrating to type-II superconductors is called *vortex*. At the center of vortex (vortex core), superconductivity is broken into normal state. The decay length ξ_{GL} gives diameter of vortex. Superconducting current circulates around the flux to cancel it (Fig. 2.7). Because the wavefunction must return to its same value after an integer number of turns around the vortex, circulation around vortex is quantised;

$$\oint_C \nabla \Phi \cdot d\mathbf{l} = 2\pi n,\tag{2.55}$$

where n is integer. Using Eq. (2.43),

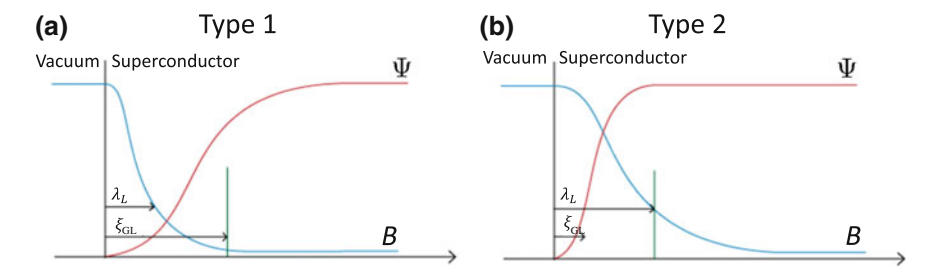
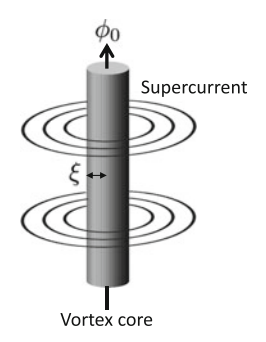


Fig. 2.6 a Schematically drawn coherence length and magnetic penetration length in a, type-I and **b** type-II superconductors

Fig. 2.7 Schematic picture of the vortex in type-II superconductor



$$\frac{e_s}{\hbar} \oint_C \mathbf{A} \cdot d\mathbf{l} = 2\pi n. \tag{2.56}$$

Here, circlulation of vector potential equals to penetrating magnetic flux. Then

$$\oint_C \mathbf{A} \cdot d\mathbf{l} = \int_S \mathbf{B} \cdot d\mathbf{S} = \phi. \tag{2.57}$$

This results in magnetic flux quantum;

$$\phi = n \frac{h}{e_s} = n\phi_0. \tag{2.58}$$

Temperature dependence of upper critical field

Here we see the upper critical field H_{c2} of type-II superconductor. At the vicinity of H_{c2} , higher order term of Ψ can be ignored. Then we have linearized GL equation:

$$-\frac{\hbar^2}{2m_s} \left[\nabla - \frac{ie_s}{\hbar} \mathbf{A}(\mathbf{r}) \right]^2 \Psi(\mathbf{r}) + \alpha \Psi(\mathbf{r}) = 0.$$
 (2.59)

This equation has the same format as Schrödinger equation; $-\alpha$ corrensoonds to energy. When an uniform magnetic field is applied along z axis, by taking a vector potential $\mathbf{A} = (0, Bx, 0)$ we obtain

$$-\frac{\hbar^2}{2m_s} \left[\frac{\partial^2}{\partial x^2} + \left(\frac{\partial}{\partial y} - \frac{ie_s B}{\hbar} x \right)^2 + \frac{\partial^2}{\partial z^2} \right] \Psi = -\alpha \Psi, \tag{2.60}$$

which has the same format as the one to describe free electron motion in magnetic field. By separation of valuable $\Psi(x, y, z) = u_n(x)e^{ik_yy+ik_zz}$, this equation is arranged into:

$$\left[-\frac{\hbar^2}{2m_s} \frac{\mathrm{d}^2}{\mathrm{d}x^2} + \frac{1}{2} m_s \omega_c^2 (x - x_0)^2 \right] u_n(x) = \frac{\hbar^2}{2m_s} \left(\frac{1}{\xi_{\mathrm{GL}}(T)^2} - k_z^2 \right) u_n(x). \quad (2.61)$$

Here, $\omega_c = e_s B/m_s$, $x_0 = \hbar k_y/e_s B$. This equation can be solved as hermonic oscillator.

$$\varepsilon_n = \left(n + \frac{1}{2}\right)\hbar\omega_c = \left(n + \frac{1}{2}\right)\hbar\left(\frac{e_s B}{m_s}\right),$$
(2.62)

where *n* is zero or positive integer. This equals to $(\hbar/2m_s)(\xi_{\rm GL}(T)^{-2}-k_z^2)$, so

$$B = \frac{\phi_0}{2\pi(2n+1)} \left(\frac{1}{\xi_{GL}(T)^2} - k_z^2 \right). \tag{2.63}$$

 H_{c2} is defined as the maximum of the field. Therefore, we obtain

$$\mu_0 H_{c2} = \frac{\phi_0}{2\pi \xi_{GL}(T)^2} = \frac{\phi_0}{2\pi \xi_{GL}(0)^2} \left(1 - \frac{T}{T_c} \right). \tag{2.64}$$

The temperature dependence of upper critical field can be acquired experimentally. We can estimate the GL coherence length at zero Kelvin by extrapolation.

2.3.3 BCS Theory

London and GL theory were postulated as phenomenological models which could describe macroscopic properties of superconductors. However, no one examined the microscopic origin why macroscopic amount of career can be stored in one quantum state. The superconducting state is fundamentally different than any possible normal metallic state; The free electron system without any impurity can have a perfect conductivity but not a Meissner state at zero-temperature limit, Thus, the transition from the normal metal state to the superconducting state must be a phase transition resulting from some many body effect.

However, direct coulomb interaction between electrons is repulsive so that it raises the total energy of systems. To reduce the energy requires some *attractive* force. We have seen the effect of phonon scattering to electrical resistance at the Sect. 2.2.3. An intuitive picture of electron-phonon interaction is described as follows; As an electron moves through the lattice, it attracts neighboring nucleus via a Coulomb interaction. The attraction leads to a local distortion of the lattice, cause the excess of the positive charge, which attracts another electron nearby. This process is taken into account to electron-electron interaction via lattice deformations, described by a phonon exchange (Fig. 2.8a). The net effect of the phonons is then to create an attractive interaction and generate quasiparticle states. This is in other words *bosonic* electron pairs, predicted to exhibit BEC.

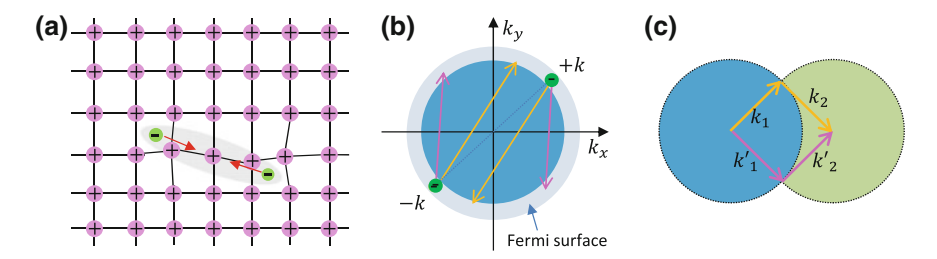


Fig. 2.8 Conceptual figures of Cooper pair formation in the BCS theory. **a** The attracting interaction between two electrons via lattice distortion. **b** The Cooper pair formation on a Fermi surface. The pink and yellow arrows indicate scattering paths which cause the attractive interaction. **c** The possible scattering paths to form Cooper pairs with nonzero center of mass of momentum. As the final state, k'_1 is forbidden except the crossing point of the spheres with the radius of $|k_1|$ centered on k_1

However, it is not easy to treat considerable amount of electron. Instead, Cooper considered to add electrons above a filled Fermi sphere as form in attracting pairs (Fig. 2.8b). Here, the total energy is minimized when two electrons with $(\mathbf{k}, -\mathbf{k})$ form bound state, namely, center of mass of a pair $\mathbf{K}=0$. (Two electrons chase each other around the lattice.) If $\mathbf{K}=0$, there are various scattering paths to cause attracting force conserving the total momentum as Fig. 2.8b. On the one hand, if $\mathbf{K}\neq 0$, such scattering paths are limited (Fig. 2.8c). Thus, Cooper quantified the superconducting ground state assuming $\mathbf{K}=0$.

Cooper instability

A wavefunction of the two electrons above Fermi sphere can be written as

$$\Psi(\mathbf{r}_1, \sigma_1, \mathbf{r}_2, \sigma_2) = \psi(\mathbf{r}_1, \mathbf{r}_2) \chi(\sigma_1, \sigma_2). \tag{2.65}$$

Here, ψ is spatial and χ is spin part. Since the pair in a zero center of mass state by the assumption, $\psi(\mathbf{r}_1, \mathbf{r}_2)$ is a function of $\mathbf{r} = \mathbf{r}_1 - \mathbf{r}_2$. By a Fourier expansion,

$$\psi(\mathbf{r}) = \frac{1}{L^3} \sum_{k} g(\mathbf{k}) e^{i\mathbf{k}\cdot\mathbf{r}},$$
 (2.66)

where $g(\mathbf{k})$ is probability amplitude to find the electron pair in $(\mathbf{k}, -\mathbf{k})$. The spatial part must obey the Schrödinger equation of

$$\left[-\frac{\hbar^2}{2m^*} (\nabla_1^2 + \nabla_2^2) + V(\mathbf{r}) \right] \psi(\mathbf{r}) = (E + 2\varepsilon_F) \psi(\mathbf{r}). \tag{2.67}$$

Here $V(\mathbf{r})$ denotes attractive potential, E is a additional energy of two electrons and ε_F is Fermi energy. By substituting the Fourier-expanded wavefunction, we obtain

$$\frac{\hbar^2 \mathbf{k}^2}{m^*} g(\mathbf{k}) + \sum_{\mathbf{k}'} g(\mathbf{k}') V_{\mathbf{k}\mathbf{k}'} = (E + 2\varepsilon_F) g(\mathbf{k}). \tag{2.68}$$

Here,

$$V_{\mathbf{k}\mathbf{k}'} = \frac{1}{L^3} \int d\mathbf{r} V(\mathbf{r}) e^{-i(\mathbf{k} - \mathbf{k}') \cdot \mathbf{r}}$$
 (2.69)

is Fourier transform of $V(\mathbf{r})$.

 $V_{\mathbf{k}\mathbf{k}'}$ indicates the attractive interaction via phonon exchange. However, the maximum energy which may be exchanged in this way is $\sim \hbar \omega_D$. (ω_D is the Debye frequency.) Thus the scattering in phase space is restricted in energy width

$$\varepsilon_F - \hbar \omega_D < \varepsilon_{\mathbf{k}} < \varepsilon_F + \hbar \omega_D,$$
 (2.70)

where $\varepsilon_{\bf k}=\hbar^2k^2/2m^*$. Since $\varepsilon_F\gg\omega_D$ in typical metal, this region is just a narrow shell on the Fermi sphere. Here, isotropic attractive interaction is described as

$$V_{\mathbf{k}\mathbf{k}'} = \begin{cases} -V_0 & (\varepsilon_F - \hbar\omega_D < \varepsilon_{\mathbf{k}} < \varepsilon_F + \hbar\omega_D) \\ 0 & \text{(otherwise)}. \end{cases}$$
 (2.71)

Then, Eq. (2.68) is simplified as

$$(-2\varepsilon_{\mathbf{k}} + E + 2\varepsilon_F) g(\mathbf{k}) = -V_0 \sum_{\mathbf{k}'} g(\mathbf{k}'). \tag{2.72}$$

Here, when spin part of wavefunction $\chi(\sigma_1, \sigma_2)$ is singlet (i.e. antisymmetric), spatial part is symmetric. Then, $g(\mathbf{k}) = g(-\mathbf{k})$ and

$$1 = V_0 \sum_{\mathbf{k}} \frac{1}{2\varepsilon_{\mathbf{k}} - E - 2\varepsilon_F} \tag{2.73}$$

$$=V_0 \int_0^{\hbar\omega_D} d\varepsilon N(\varepsilon_F + \varepsilon) \frac{1}{2\varepsilon - E}$$
 (2.74)

$$= V_0 N(\varepsilon_F) \ln \frac{E - 2\hbar\omega_D}{E}, \qquad (2.75)$$

where, $N(\varepsilon)$ is density of state, which is almost constant around Fermi energy. When $V_0N(\varepsilon_F)\ll 1$,

$$E = -2\hbar\omega_D \exp\left(-\frac{2}{V_0 N(\varepsilon_F)}\right). \tag{2.76}$$

This indicates that the weak phonon-mediated attractive interaction $-V_0$ promote the formation of a spin-singlet pair $(k \uparrow, -k \downarrow)$, which is called Cooper pair. No matter

how small attracting force is sufficient to destabilize the Fermi sea, and creates a new ground state.

On the other hand, when spin part is triplet, spatial part is antisymmetric. Then, $g(\mathbf{k}) = -g(-\mathbf{k})$, which make the right hand of Eq. (2.72) equals to zero and

$$E = 2(\varepsilon_{\mathbf{k}} - \varepsilon_F) > 0. \tag{2.77}$$

Therefore there is no instability of Fermi sphere.

From above discussion, following three assumptions are used in the BCS theory.

- 1. Cooper pairs take zero center-of-mass momentum.
- 2. Cooper pairs are spin singlet states.
- 3. Cooper pairs are created by isotropic attractive interaction.

BCS ground state

As discussioned in the preceding section, attractive interaction modifies distribution of electron in the ground state; All electrons are stored in Fermi sphere in free electronic ground state, while some of the electrons occupy the states above the Fermi surface as pairs in BCS one. Let us simplify the notations of pairing states; $|1\rangle_{\mathbf{k}}$ ($|0\rangle_{\mathbf{k}}$) represents occupation (unoccupation) of ($\mathbf{k} \uparrow, -\mathbf{k} \downarrow$), whose probability amplitude is defined as $v_{\mathbf{k}}$ ($u_{\mathbf{k}}$). They satisfy

$$v_{\mathbf{k}}^2 + u_{\mathbf{k}}^2 = 1. (2.78)$$

BCS wavefunction is written as

$$|\Psi\rangle = \prod_{k} \left[u_{k} |0\rangle_{k} + v_{k} |1\rangle_{k} \right]. \tag{2.79}$$

Normal ground state is represented by

$$\begin{cases} v_{\mathbf{k}} = 1, & u_{\mathbf{k}} = 0 \ (|\mathbf{k}| < k_F) \\ v_{\mathbf{k}} = 0, & u_{\mathbf{k}} = 1 \ (|\mathbf{k}| > k_F). \end{cases}$$
 (2.80)

Creation and annihilation operators for pairs are definded as $\eta_{\mathbf{k}}^{\dagger}$ and $\eta_{\mathbf{k}}$, respectively.

$$\eta_{\mathbf{k}}^{\dagger}|1\rangle_{\mathbf{k}} = 0 \tag{2.81}$$

$$\eta_{\mathbf{k}}^{\dagger}|0\rangle_{\mathbf{k}} = |1\rangle_{\mathbf{k}} \tag{2.82}$$

$$\eta_{\mathbf{k}}|1\rangle_{\mathbf{k}} = |0\rangle_{\mathbf{k}} \tag{2.83}$$

$$\eta_{\mathbf{k}}|0\rangle_{\mathbf{k}} = 0 \tag{2.84}$$

By using these operators, phonon mediated electron-electron scattering $(\mathbf{k}\uparrow,-\mathbf{k}\downarrow)\to(\mathbf{k}'\uparrow,-\mathbf{k}'\downarrow)$ is described as $\eta_{\mathbf{k}'}^{\dagger}\eta_{\mathbf{k}}$. Thus its Hamiltonian is

$$V = -V_0 \sum_{\mathbf{k}\mathbf{k}'} \eta_{\mathbf{k}'}^{\dagger} \eta_{\mathbf{k}}. \tag{2.85}$$

where V_0 is energy gain due to the interaction. Here **k** is limited by $\varepsilon_F - \hbar\omega_D < \varepsilon_{\mathbf{k}} < \varepsilon_F + \hbar\omega_D$. The expected value of the energy reduction is described as follows;

$$\langle \Psi | V | \Psi \rangle = -V_0 \left[\prod_{p} \left(u_{\mathbf{p}} \langle 0 |_{\mathbf{p}} + v_{\mathbf{p}} | 1 \rangle_{\mathbf{p}} \right) \left(\sum_{\mathbf{k}\mathbf{k}'} \eta_{\mathbf{k}'} \right) \prod_{\mathbf{p}'} \left(u_{\mathbf{p}'} | 0 \rangle_{\mathbf{p}'} + v_{\mathbf{p}'} | 1 \rangle_{\mathbf{p}'} \right) \right]. \tag{2.86}$$

Since $\langle 1|1\rangle_{\mathbf{k}\mathbf{k}'} = \delta_{\mathbf{k}\mathbf{k}'}, \langle 0|0\rangle_{\mathbf{k}\mathbf{k}'} = \delta_{\mathbf{k}\mathbf{k}'}, \langle 0|1\rangle_{\mathbf{k}\mathbf{k}'} = 0,$

$$\langle \Psi | V | \Psi \rangle = -V_0 \sum_{\mathbf{k}\mathbf{k}'} v_{\mathbf{k}} u_{\mathbf{k}'} u_{\mathbf{k}} v_{\mathbf{k}'}. \tag{2.87}$$

On the other hand, Cooper pair formation increases kinetic energy E_{kin} of the system.

$$E_{\rm kin} = 2\sum_{\bf k} \varepsilon_{\bf k} v_{\bf k}^2. \tag{2.88}$$

Here, $\varepsilon_{\mathbf{k}} = \varepsilon_{\mathbf{k}} - \varepsilon_F$. Thus, we obtain the expected value of total energy W as

$$W = 2\sum_{\mathbf{k}} \varepsilon_{\mathbf{k}} v_{\mathbf{k}}^2 - V_0 \sum_{\mathbf{k}\mathbf{k}'} v_{\mathbf{k}} u_{\mathbf{k}'} u_{\mathbf{k}} v_{\mathbf{k}'}. \tag{2.89}$$

By minimizing W with respect to variations in v_k , u_k ,

$$2\varepsilon_{\mathbf{k}} - V_0 \frac{1 - 2v_{\mathbf{k}}^2}{v_{\mathbf{k}} u_{\mathbf{k}}} \sum_{\mathbf{k}'} u_{\mathbf{k}'} v_{\mathbf{k}'} = 0.$$
 (2.90)

Here we used $\partial W/\partial v_{\mathbf{k}}^2 = 0$. The summation about \mathbf{k}' is constant so that we define a constant Δ by

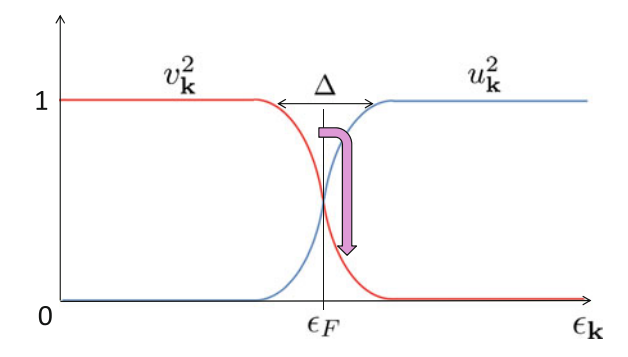
$$\Delta \equiv V_0 \sum_{\mathbf{k}'} u_{\mathbf{k}'} v_{\mathbf{k}'}. \tag{2.91}$$

Then,

$$\frac{v_{\mathbf{k}}u_{\mathbf{k}}}{1-2v_{\mathbf{k}}^2} = \frac{\Delta}{2\varepsilon_{\mathbf{k}}} \tag{2.92}$$

From Eq. (2.78), we obtain a quadratic

Fig. 2.9 Schematic drawing of the probability amplitude of the BCS ground state as a function of energy. The $v_{\bf k}$ is the probability amplitude as a Cooper pair. Electrons in an energy window $\varepsilon_F \pm \Delta$ are redistributed from the ground state of free electron model



$$v_{\mathbf{k}}^4 - v_{\mathbf{k}}^2 + \frac{\Delta^2}{4E_{\mathbf{k}}^2} = 0, \tag{2.93}$$

$$E_{\mathbf{k}} = \sqrt{\varepsilon_{\mathbf{k}}^2 + \Delta^2},\tag{2.94}$$

which can be solved to yield

$$\begin{cases} u_{\mathbf{k}}^2 = \frac{1}{2} \left(1 + \frac{\varepsilon_{\mathbf{k}}}{E_{\mathbf{k}}} \right), \\ v_{\mathbf{k}}^2 = \frac{1}{2} \left(1 - \frac{\varepsilon_{\mathbf{k}}}{E_{\mathbf{k}}} \right). \end{cases}$$
 (2.95)

This indicates that electrons slightly below the Fermi surface $(\varepsilon_F - \Delta < \varepsilon < \varepsilon_F)$ redistribute above the Fermi surface $(\varepsilon_F < \varepsilon < \varepsilon_F + \Delta)$ in the BCS ground state. (Fig. 2.9).

Superconducting gap

Subtracting Eqs. (2.91) to (2.95) leads to

$$\Delta = V_0 \sum_{\mathbf{k}} \left[\frac{1}{2} \left(1 - \frac{\varepsilon_{\mathbf{k}}}{E_{\mathbf{k}}} \right) \frac{1}{2} \left(1 + \frac{\varepsilon_{\mathbf{k}}}{E_{\mathbf{k}}} \right) \right]^{1/2}$$
 (2.96)

$$= \frac{1}{2} V_0 \sum_{\mathbf{k}} \left(\frac{E_{\mathbf{k}}^2 - \varepsilon_{\mathbf{k}}^2}{E_{\mathbf{k}}^2} \right)^{1/2} \tag{2.97}$$

$$= \frac{\Delta}{2} V_0 \sum_{\mathbf{k}} \frac{1}{(\varepsilon_{\mathbf{k}}^2 + \Delta^2)^{1/2}}.$$
 (2.98)

The summation about k' is able to be replaced by integral;

$$1 = \frac{N(\varepsilon_F)V_0}{2} \int_{-\hbar\omega_D}^{\hbar\omega_D} \frac{1}{(\varepsilon^2 + \Delta^2)^{1/2}} d\varepsilon \tag{2.99}$$

$$= N(\varepsilon_F) V_0 \int_0^{\hbar\omega_D} \frac{1}{(\varepsilon^2 + \Delta^2)^{1/2}} d\varepsilon \tag{2.100}$$

$$= N(\varepsilon_F) V_0 \sinh^{-1} \left(\frac{\hbar \omega_D}{\Delta} \right). \tag{2.101}$$

Hence

$$\frac{\hbar\omega_D}{\Delta} = \sinh\left(\frac{1}{N(\varepsilon_F)V_0}\right). \tag{2.102}$$

In weak coupling superconductor, $N(\varepsilon_F)V_0 \ll 1$. So

$$\Delta = 2\hbar\omega_D \exp\left(-\frac{1}{N(\varepsilon_F)V_0}\right) \tag{2.103}$$

$$=2k_B\Theta_D\exp\left(-\frac{1}{N(\varepsilon_F)V_0}\right),\tag{2.104}$$

where Θ_D is the Debye temperature.

The approximation of $N(\varepsilon_F)V_0 \ll 1$ cannot be applied to strong coupled superconductors. Some of the results here are modified by analytical solution of electronphonon coupling Hamiltonian (described later).

In the BCS ground state, electrons are above Fermi energy as pairs. Thus, elemental excitation (or *quesiparticle*) is half filling of a pair state. Then the system gets kinetic energy of an unpaired electron

$$\delta E = \varepsilon_{\mathbf{k}} - \left(2\varepsilon_{\mathbf{k}} v_{\mathbf{k}}^2 - 2V_0 v_{\mathbf{k}} u_{\mathbf{k}} \sum_{\mathbf{k}'} v_{\mathbf{k}'} u_{\mathbf{k}'} \right). \tag{2.105}$$

Here Eq. (2.89) is used. From Eqs. (2.91) and (2.95), one can find that δE corresponds to $E_{\bf k}$ in Eq. (2.94). This leads to the dispersion relation of superconducting state;

$$E_{\mathbf{k}} = \sqrt{\varepsilon_{\mathbf{k}}^2 + \Delta^2}.\tag{2.106}$$

It has an energy gap of 2Δ as seen in Fig. 2.10a. Since normal electronic states turn into superconducting states one-to-one, the density of state in superconducting phase $N_s(E)$ has easy relationship with normal density of state $N_n(\varepsilon)$;

$$N_s(E)dE = N_n(\varepsilon)d\varepsilon.$$
 (2.107)

Then,

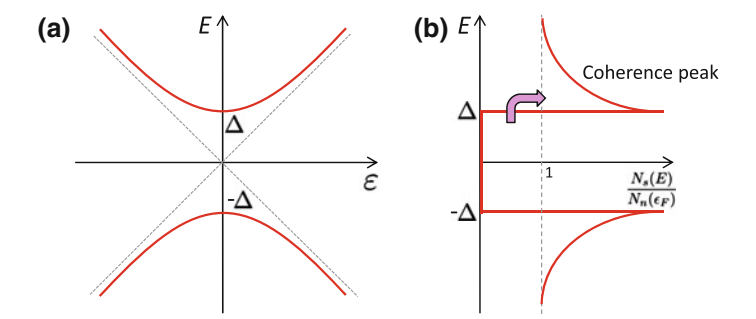


Fig. 2.10 Schematic pictures describing the BCS ground state. a The dispersion relationship of quasi particles. There opens a gap of 2Δ centering on ε_F . b The energy distribution of density of state. The states inside of the gap are moved and stacked to form coherence peaks at $E=\pm\Delta$ with Cooper pair generation

$$N_s(E) = N_n(\varepsilon) \frac{d\varepsilon}{dE}$$
 (2.108)

$$=N_n(\varepsilon)\frac{d}{dE}\sqrt{E^2-\Delta^2}.$$
 (2.109)

Around the Fermi energy, $N_n(\varepsilon_F)$ is approximately constant. Then we obtain

$$\frac{N_s(E)}{N_n(\varepsilon_F)} = \begin{cases} 0 & (|E| < \Delta), \\ \frac{|E|}{\sqrt{E^2 - \Delta^2}} & (|E| > \Delta). \end{cases}$$
 (2.110)

As shown in Fig. 2.10b, the energy gap of 2Δ is clearly opened. The normal states within $\varepsilon_F - \Delta < E < \varepsilon_F + \Delta$ are stacked at $E = \pm \Delta$, resulting in sharp peaks (coherence peaks).

Superconducting gap at finite temperature

At finite temperature, thermal energy breaks Cooper pairs and creates quasi particles with the dispersion Eq. (2.106). Then, Δ decreases by heating the system and vanish at T_c .

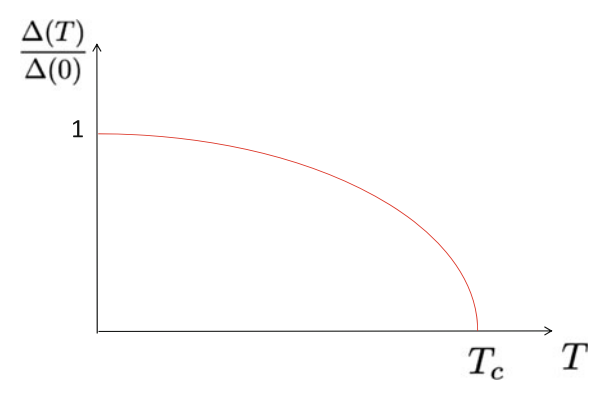
The quasi particles obey Fermi distribution.

$$f(E_{\mathbf{k}}) = \frac{1}{\exp(E_{\mathbf{k}}/k_B T) + 1}.$$
 (2.111)

Hence, the occupation probability of Cooper-paired states is described as $1-2f(E_k)$ at finite temperature. In order to obtain temperature-dependency of superconducting gap $\Delta(T)$, we consider the occupation probability in Eq. (2.100).

$$1 = N(\varepsilon_F) V_0 \int_0^{\hbar\omega_D} \frac{1 - 2f(E_{\mathbf{k}})}{(\varepsilon^2 + \Delta^2)^{1/2}} d\varepsilon.$$
 (2.112)

Fig. 2.11 Schematically drawn temperature dependence of superconducting gap in the BCS theory



In Fig. 2.11, numerically obtained $\Delta(T)$ is displayed. Around the T_c , approximately

$$\frac{\Delta(T)}{\Delta(0)} \sim 1.74 \sqrt{1 - \frac{T}{T_c}},\tag{2.113}$$

indicating rapid destruction of Cooper pairs.

Furthermore, from $\Delta(T_c) = 0$,

$$1 = N(\varepsilon_F) V_0 \int_0^{\hbar\omega_D} \frac{\tanh(\varepsilon/2k_B T_c)}{\varepsilon} d\varepsilon. \tag{2.114}$$

This leads to

$$k_B T_c = 1.14\hbar\omega_D \exp\left(-\frac{1}{N(\varepsilon_F)V_0}\right).$$
 (2.115)

In weak coupling superconductor, comparison between this equation and Eq. (2.104) give us an universal relation:

$$\frac{\Delta(0)}{k_B T_c} = 1.76. {(2.116)}$$

Connection to phenomenology

Once the BCS theory had been established [8], the phenomenologies by London, Gintzburg and Landau was confirmed, starting from the microscopic origin [9–11]. That is, what is called *superelectron* in London theory is actually Cooper pair with charge of $e_s = 2e$ and effective mass of $m_s = 2m^*$. Here I summarize the important results from the phenomenologies.

Penetration length
$$\lambda_L = \left(\frac{m^*\beta}{2\mu_0 e^2 a T_c}\right)^{1/2} \left(1 - \frac{T}{T_c}\right)^{-1/2}$$
 (2.117)

Quantized magnetic flux
$$\phi_0 = \frac{h}{2e} = 2.07 \times 10^{-15} \text{(Wb)}$$
 (2.118)

GL coherence length
$$\xi_{\text{GL}}(T) = \left(\frac{\hbar^2}{4m_* a T_{\text{c}}}\right)^{1/2} \left(1 - \frac{T}{T_{\text{c}}}\right)^{-1/2}$$
 (2.119)

GL parameter
$$\kappa \equiv \frac{\lambda_L}{\xi_{\rm GL}} = \frac{m^*}{e\hbar} \sqrt{\frac{2\beta}{\mu_0}}$$
 (2.120)

Upper critical field
$$\mu_0 H_{c2}(T) = \frac{\phi_0}{2\pi \xi_{GL}(0)^2} \left(1 - \frac{T}{T_c} \right)$$
 (2.121)

What is microscopic picture of magnetic decoupling of Cooper pairs? Since paired two electrons have opposit momentum each other, their binding is broken by Lorentz force. This is called *orbital pair breaking*. In ordinal superconductor, orbital breaking occurs at small magnetic field and determines the upper critical field. However, when it is supressed by some reason, Cooper pair survives until spin-singlet component becomes unstable by Zeeman effect. This is called *paramagnetic effect*. The BCS theory predict that this effect occurs at $\mu_0 H_p(T) = 1.86T_c(K)$ at 0 K (Pauli limit).

The BCS theory also gives microscopic interpretations of coherence length. In the real space, the length scale corresponding to superconducting gap is given by the uncertainty principle:

$$\xi_0 = \frac{\hbar \nu_{\rm F}}{\pi \, \Delta(0)}.\tag{2.122}$$

This is called Pippard's coherence length and regarded as *characteristic size of Cooper pair*. Namely, an electron feels the interaction from another one at the distance of ξ_0 or less and form bound state. This is why macroscopic superconducting state cannot variate within coherence length.

It should be note that, since ξ_0 is ideal coherence length, the effective coherence length ξ is suppressed by impurity scattering as

$$\frac{1}{\xi} = \frac{1}{\xi_0} + \frac{1}{l},\tag{2.123}$$

where l is mean free path of normal electrons. $\xi_0 \ll l$ is called clean limit while $\xi_0 \gg l$ is dirty limit. In dirty limit,

$$\xi = 0.85\sqrt{\xi_0 l}.\tag{2.124}$$

In usual case, the effective coherence length coincides to experimental obtained GL coherence length.

2.3.4 Josephson Effect and Critical Current

Let us consider two superconducting materials described by macroscopic wavefunctions: $\Psi_i = \Delta_i(0)e^{i\Phi_i}$ (i = 1, 2). When the two superconductors are coupled by a weak link (e.g. a thin insulating barrier), a current flows indefinitely long without any voltage applied, due to the difference in phase of the wavefunction. This is called *Josephson effect*. Current density driven by a Josephson junction (JJ) is given as

$$J = J_c \sin(\Phi_2 - \Phi_1), \tag{2.125}$$

$$J_c \equiv \gamma \frac{e\hbar}{m^*} \Delta_1(0) \Delta_2(0). \tag{2.126}$$

[12]. Here γ is strength of the coupling and J_c is the maximum current density. Sometimes JJ is naturally formed by defects and impurities. In superconducting thin films, superconducting regions tend to be patched and connected via JJs each other. It is pointed that even atomic steps on the surface act as JJs in superconducting surface systems on semiconductors [13]. If the current through JJ is applied more than Eq. (2.126), superconductivity is broken down [13–15]. Such threshold is called critical current I_c , which relates with normal state resistance R_n as follows.

$$I_c(T) = \frac{\pi \Delta(T)}{2eR_n} \tanh\left(\frac{\Delta(T)}{2k_B T}\right)$$
 (2.127)

For the interior of cleaner superconductor, on the other hand, I_c is determined by pair breaking current [16]; When superconducting current is flowing with group velocity v_s , the center-of-mass of Cooper pair's momentum **K** is non-zero and the energy of quasi particle is $\hbar k_F v_s$. The pair is broken when this shift reaches to $\Delta(T)$. Thus critical current is proportional to $\Delta(T)$;

$$I_s(T) \propto \left[1 - \left(\frac{T}{T_c}\right)^2\right]^{3/2}$$
 (2.128)

2.4 Special Cases of Superconductivity

2.4.1 Strong Coupled Superconductor

 $\lambda \equiv N(\varepsilon_F)V_0$ in Eq. (2.115) indicates how strongly electrons feel attractive interaction. If it is mediated by phonon, λ is called electron-phonon coupling constant. In the BCS theory above, it has been assumed that $\lambda \equiv N(\varepsilon_F)V_0 \sim 0$. Eliashberg expanded the discussion to strong coupling case and McMillan and Allen-Dynes calculated the critical temperature at $\lambda \sim 1$ [17, 18].

$$T_{c} = \frac{\hbar\omega_{D}}{1.45k_{B}} \exp\left[-\frac{1.04(1+\lambda)}{\lambda - \mu^{*}(1+0.62\lambda)}\right],$$
 (2.129)

where μ^* is a parameter of the direct repulsive interaction between electrons. Typically it is 0.1–0.15. Equation (2.129) is rewritten using the Debye temperature Θ_D as

$$T_{\rm c} = \frac{\Theta_D}{1.45} \exp\left[-\frac{1.04(1+\lambda)}{\lambda - \mu^*(1+0.62\lambda)}\right]. \tag{2.130}$$

Then, Eq. (2.116)

$$a \equiv \frac{\Delta(0)}{k_B T_c} = 1.76 \tag{2.131}$$

is also need to be modified. Experimentally, the constant a is enhanced. In typical example of bulk Pb with $\lambda=1.2-1.7$ [19], a=2.19 [20]. Since materials in this study also have large electron-phonon coupling, I considered the possible enhancement of a to convert $T_{\rm c}$ to the superconducting gap. Namely, the gap is estimated by

$$\Delta(0) = ak_B T_c, \tag{2.132}$$

where a is ranged from 1.76 to 2.2.

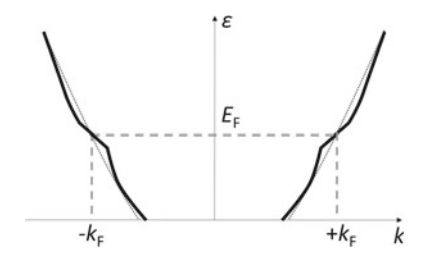
One can see the effect of strong electron-phonon coupling in enhancement of the effective mass of normal state electron as;

$$\lambda = \frac{m' - m^*}{m^*}. (2.133)$$

 m^* is effective mass without electron-phonon coupling while m' is enhanced one.

Since Fermi energy in metal is $\sim 10^5$ K while Debye temperature is in the order of several hundred Kelvin, the enhancement of effective mass occurs at only the neighborhood of Fermi surface. Thus, there appear *kink* structure in the band dispersion near Fermi surface (Fig. 2.12), which is a sign of strong electron-phonon

Fig. 2.12 Schematic picture of a kink structure in an electronic band dispersion, which induced by the electron-phonon interaction



interaction observed in recent studies on superconductivity by ARPES [21, 22]. The spectral function $A(\mathbf{k})$, ω measured by ARPES [23] provides information on both the single-particle electronic dispersion $\varepsilon_0(\mathbf{k})$ and the quasi particle self-energy $\Sigma(\mathbf{k},\omega) = \Sigma'(\mathbf{k},\omega) + i \Sigma''(\mathbf{k},\omega)$. The real and imaginary parts account for the renormalization of electron energy and lifetime due to many-body interactions e.g. electron-phonon coupling. Both of them are directly obtained by fiiting with a Lorentzian, the ARPES intensity profiles at constant energy (momentum distribution curve, MDC); The real and imaginary parts of self-energy can be determined by peak position and peak width, respectively. Here we define Eliashberg function $F(\omega)$, which is the phonon density of states weighted by the electron-phonon coupling strength;

$$\lambda \equiv 2 \int_0^\infty \frac{d\omega}{\omega} \alpha(\omega)^2 F(\omega) \tag{2.134}$$

Then Σ'' is described by the following equation.

$$\Sigma'' = \pi h \int_0^{\omega_D} d\omega' \alpha(\omega)^2 F(\omega') \left[1 - f(\omega - \omega') + f_B(\omega') + f(\omega + \omega') \right] + W_0.$$
(2.135)

Here, ω_D is the Debye frequency and W_0 is a constant. $f_B(\omega)$ and $f(\omega)$ are distribution function of phonon (boson) and electron (fermion), respectively. Therefore, the momentum resolved $\alpha(\omega)^2 F(\omega)$ function can be extracted from the $\Sigma''(\mathbf{k}, \omega)$ probed by ARPES by the integral inversion procedure, resulting in calculation of total electron-phonon coupling λ .

At temperature sufficiently higher than Debye temperature, Eq. (2.135) can be simplified as:

$$\Sigma'' = \pi \lambda k_B T + W_0. \tag{2.136}$$

This indicates that we can extract λ from temperature-dependent ARPES spectrum.

2.4.2 Two-Dimensional Superconductivity

As a general sense, the term "two-dimensional superconductor" does not necessarily mean true 2D system—it does mean that the thickness of superconducting electron/hole system is thinner than coherence length $\xi_{\rm GL}(0)$. The first notable property of 2DSC is anisotoropy in upper critical field [24–27]. Since the out-of-plane electron motion is prohibited, orbital breaking of Cooper pair is no longer dominant when magnetic field is applied for the in-plane direction. Instead, Pauli paramagnetic effect may determine the upper critical field. This is an experimental advantage to probe spin-related superconducting phenomena, which are predicted in exotic 2DSC systems introduced later.

The next point to be consider is effect of *fluctuation*. As is schematically shown in Fig. 2.13a, when a d-dimensional system is in normal conducting state, the superconducting condensation energy per unit volume required for the first pair is $\mu_0 H^{\parallel}_{c2}/2$. On the one hand, at finite temperature, a system has thermal fluctuation $k_B T$ due to the Fermi distribution function. The fluctuation promote the formation of Cooper pair, which cause gradual decrement of resistance from slightly above the critical temperature. On the other hand, when the system is in superconducting state, the thermal fluctuation create the vortex pairs, which induce residual resistance below T_c (Fig. 2.13b). These effects arise from amplitude and phase part of order parameter, respectively. They cannot be negligible when

$$k_B T \sim \xi^d \frac{\mu_0 H^{\parallel}_{c2}}{2},$$
 (2.137)

where the diameter of a Cooper pair ξ^d is considered. Equation (2.137) indicate that the required thermal energy is smaller in lower dimension. This is why we have to consider the thermal fluctuation in low-dimensional superconductors.

Amplitude fluctuation

The correction due to fluctuation in ampritude of order paramaeter near T_c is described as follows. [28, 29].

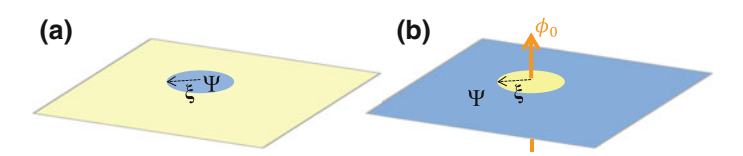


Fig. 2.13 Conceptual illustrations describing the effect of thermal fluctuation on the superconductivity. The yellow (blue) region indicates normal (superconducting) state. a amplitude fluctuation, where a Cooper pair is generated by thermal fluctuation even in $T > T_{\rm c}$. b Phase fluctuation, where a vortex is generated by thermal fluctuation even in $T < T_{\rm c}$

$$\rho = \frac{1}{\sigma_0 + \sigma_{AL} + \sigma_{MT}},\tag{2.138}$$

$$\sigma_{\rm AL} = \frac{e^2}{16\hbar} \cdot \frac{T_{\rm c}}{T - T_{\rm c}},\tag{2.139}$$

$$\sigma_{\rm MT} = \frac{e^2}{8\hbar} \cdot \frac{T_{\rm c}}{T - (1+\delta)T_{\rm c}} \ln \frac{T - T_{\rm c}}{\delta T_{\rm c}}.$$
 (2.140)

 σ_{AL} is called Aslamazov-Larkin (AL) term, corresponding to excess conductivity carried by thermally created Cooper pairs. σ_{MT} is Maki-Thompson (MT) term, which is contribution due to the coherent scattering of electrons forming a Cooper pair on the same elastic impurity. It includes material-dependent pair-breaking parameter δ , whose typical value is ca. 0.1. Particularly, the MT term is important in clean two-dimensional superconducting systems.

Phase fluctuation

The idea of phase fluctuation is originated from Berezinskii-Kosterlitz-Thouless transition (BKT transition). The BKT transition can be found in 2D condensed matter systems that are approximated by XY model. The XY model is a two-dimensional vector spin model, which is not expected to possess a long-range order except absolute zero-temperature because of transverse fluctuations (Mermin-Wagner theorem). At finite temperature, one finds a quasi-ordered phase called *topological order*, where spin waves with long wavelength are excited and the spin angle varies over long distance as shown in Fig. 2.14. Vortices, where the sum of angle changes along an arbitrary closed curve around it is kept $2\pi n(n)$ is integer) are topologically stable configurations. Here, generation of a single free vortex takes much higher energy than bound vortex-antivortex pairs (see Fig. 2.14b) because of topology. This bound antiparallel vortex pairs is dissociated thermodynamically into unbound vortices above a characteristic temperature $T_{\rm BKT}$. This kind of transition is called BKT transition.

It is noted that the 2D XY models can be applied to many cases of real 2DSC systems, where patched superconducting areas are connected each other by JJs and each area has own phase of order parameter. Since in type-II superconductor, penetrating magnetic flux gives additional phase of 2π surrounding superconducting order parameter, it directly means *vortex* as a topological defect. When fluctuation-induced free vortices are moved by external current in the transverse direction, the motion gives rise to a voltage drop in the longitudinal direction, resulting in finite energy dissipation. However, for $T < T_{\rm BKT}$, vortices appear as only bound pair states due to the topological order, namely, no free vortices exist, resulting in the true zero-resistance state. For $T_{\rm BKT} < T < T_{\rm c}$, more and more free vortices start to be generated and cause resistance described by Halperin-Nelson equation as follows [30]:

$$R \propto \exp\left[-2b\left(\frac{T_{\rm c} - T_{\rm BKT}}{T - T_{\rm BKT}}\right)^{1/2}\right]. \tag{2.141}$$

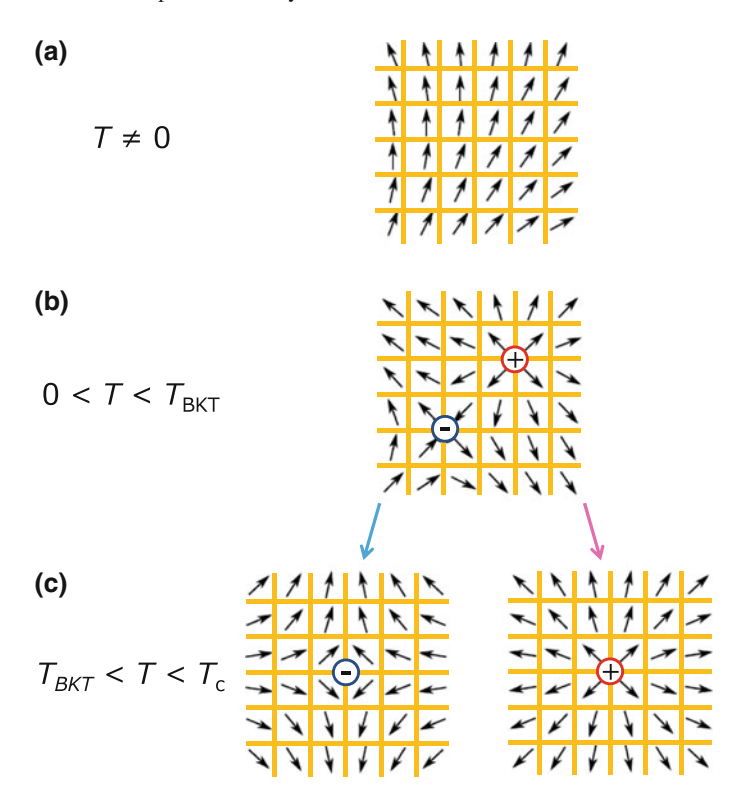


Fig. 2.14 Analogical explanation of the BKT transition in the two-dimensional spin system. **a** Topological order, which conserved in pure two-dimensional system at $T \neq 0$ despite of longrange spin wave. **b** and **c** Vortex as a defect of topological order. The pairs are excited by low energy, while depaired vortices move freely at higher temperature than $T_{\rm BKT}$

In the dirty limit 2D superconductor, following equation is also used to estimate T_{BKT} [31];

$$\frac{T_{\rm BKT}}{T_{\rm c}} \sim \frac{1}{1 + 0.17 \frac{R_n}{R_c}}.$$
 (2.142)

Here, R_n is normal state resistance and $R_c = \hbar/e^2 = 4.11 \text{ k}\Omega$.

The vortex-antivortex pairs become unbound under finite external current. This unbinding occurs progressively as the current is increased, leading to a current-voltage (I-V) characteristics of power law dependence. As temperature is lowered from above $T_{\rm BKT}$, exponent a jumps universally from 1 to 3 at $T=T_{\rm BKT}$ and increases further at lower temperatures, which is one of the hallmarks of the BKT transition. Since 1980's, current-voltage characteristics in superconducting thin films have been intensively studied in terms of BKT physics [25, 32–38]. However, no

results reproduced the theoretical prediction completely. It is still open question whether we can find BKT transition in quasi-2D systems.

2.4.3 Disorder-Induced Superconductor-Insulator Transition

In 2D superconductor, it is known that disorder plays important role. The most significant and general phenomena is disorder-induced SIT; 2D systems is transit from superconducting phase to insulating directly by introduction of disorder. This is in clear contrast to the 3D case where superconductivity is robust against disorder.

As mentioned in Sect.. 2.2.4, a normal metal transits into an insulator due to the Anderson localization when its resistance exceeds the quantized resistance of single electron;

$$\frac{h}{e^2} = 25.8 \text{ (k}\Omega).$$
 (2.143)

The disorder-induced SIT also occurs with respect to resistance at the quantized value of Cooper pair [39]

$$R_c = \frac{h}{4e^2} = 6.45(k\Omega),$$
 (2.144)

which is called quantum critical.

Close to the SIT, i.e., at $x = x_c$ and T = 0, where x is a control parameter, the linear response and the nonlinear response of the system are governed by the divergence of the correlation length ξ [40]. In the critical regime, the divergence of ξ is cut off by a length scale l_T , which is determined by the temperature as $l_T \sim T^{-1/z}$. One can derive a scaling relation for resistance R with temperature and a control parameter near x_c :

$$R(x,T) = F\left(\frac{|x - x_c|}{T^{z\nu}}\right),\tag{2.145}$$

where $F\left(\frac{|x-x_c|}{T^{zv}}\right)$ is an arbitrary scaling function. Scaling of the zero bias resistance with T and x determines the product zv. Experimentally, one can replot R(x,T) as a function of the scaling variable $\frac{|x-x_c|}{T^{zv}}$, and adjust the power zv to obtain the best visual coincidence of the data [40]. Generally speaking, the value of zv relates to universality class of the system. For example, zv=4/3 and z=2/3 correspond to the classical percolation and the 3D XY models, respectively. The most famous experimental demonstration of disorder-induced SIT was given by Goldman et al., where superconducting and insulating phases are clearly separated at z=2/30 for z=2/31. Even if a superconductor has slightly lower resistance than quantum critical, perpendicular magnetic field causes SIT (B-SIT) [42]. The transition field of B-SIT (z=2/32) appears as a crossing point of z=2/33 curves measured at various temperatures (see Fig. 2.15a).

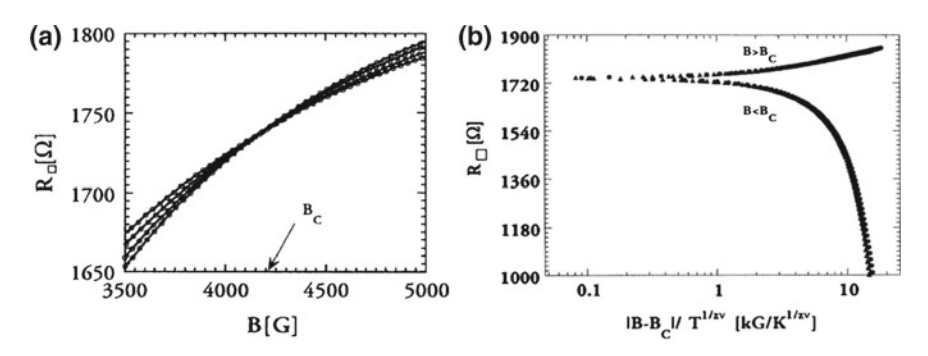


Fig. 2.15 Electrical transport properties of the amorphous MoGe thin film [42]. a Magnetic field dependence of sheet resistivity, where the curves cross at one point. b Scaling of sheet resistivity as a function of magnetic field and temperature. Reprinted with permission from Ref. [42]

Figure 2.15b shows a result of scaling procedure onto the B-SIT. The resistance curves collapse into two blanches: insulator on the high field side ($B > B_c$) and superconductor on low field side ($B < B_c$).

2.4.4 Superconductivity Without Spatial Inversion Symmetry

Since the discoverly of high- T_c cuprates, *exotic superconductors* has been intensively studied in the solid state physics community. Here "exotic" means "deviation from BCS theory". Namely, (at least) one of the following assumptions violates in it:

- 1. Cooper pairs take zero center-of-mass momentum.
- 2. Cooper pairs are spin singlet states.
- 3. Cooper pairs are created by isotropic attractive interaction.

From the third assumption, the superconducting gap $\Delta(0)$ obtained by the BCS theory is isotoropic. Such isotropic superconducting state is named s-wave after the analogy to the hydrogen atomic model. When the attractive interaction is not isotoropic, anisotoropic superconducting states $(p, d, f, \dots$ -wave) are possible, which have different parity.

Let us consider a Cooper pair originates from two electrons denoted by $(\mathbf{r}_{1,2}, \sigma_{1,2})$: $\Psi(\mathbf{r}, \sigma_1, \sigma_2) = \psi(\mathbf{r})\chi(\sigma_1, \sigma_2)(\mathbf{r} = \mathbf{r}_1 - \mathbf{r}_2)$: relative coordinate). Its orbital and spin parts are classified by their parities as follows;

Even function
$$\psi_{\text{even}}(-\mathbf{r}) = \psi_{\text{even}}(\mathbf{r}),$$
 (2.146)

Odd function
$$\psi_{\text{odd}}(-\mathbf{r}) = -\psi_{\text{odd}}(\mathbf{r}),$$
 (2.147)

Singlet
$$\chi_s(\sigma_2, \sigma_1) = -\chi_s(\sigma_1, \sigma_2),$$
 (2.148)

Triplet
$$\chi_t(\sigma_2, \sigma_1) = \chi_t(\sigma_1, \sigma_2)$$
. (2.149)

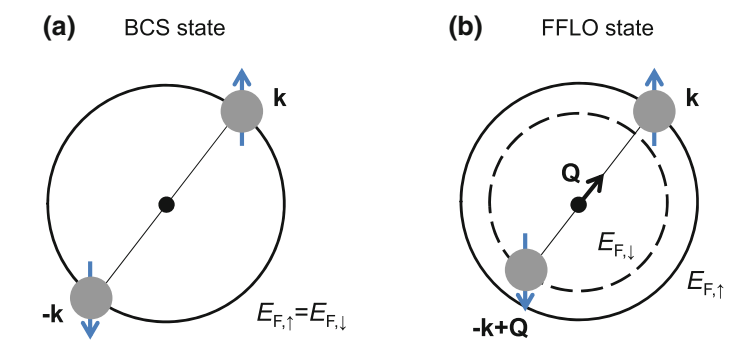


Fig. 2.16 a Conceptual illustration of the Cooper pair in a, BCS state and b FFLO state

According the Pauli exclusion principle, total wavefunction must be antisymmetric against the exchange of two electrons;

$$\Psi(-\mathbf{r}, \sigma_2, \sigma_1) = -\Psi(\mathbf{r}, \sigma_1, \sigma_2). \tag{2.150}$$

Hence, only two combinations below are allowed as pair states.

$$\Psi_{\text{even.s}}(\mathbf{r}, \sigma_1, \sigma_2) = \psi_{\text{even}}(\mathbf{r}) \chi_{\text{s}}(\sigma_1, \sigma_2)$$
 (2.151)

$$\Psi_{\text{odd},t}(\mathbf{r},\sigma_1,\sigma_2) = \psi_{\text{odd}}(\mathbf{r})\chi_t(\sigma_1,\sigma_2)$$
 (2.152)

The latter case is known as spin-triplet superconductor.

The first assumption violates when the system has Zeeman-type spin splitting. As mentioned in Sect. 2.3.3, spin-singlet and zero center-of-mass momentum pair is the most favorable on a spin-degenerate Fermi surface as shown in Fig. 2.16a. On the other hand, on a spin-splitting Fermi surface, spin singlet pair has nonzero center-of-mass momentum. Figure 2.16b shows such a state. This results in spatial variation of order parameter in macroscopic scale, called Fulde-Ferrell-Larkin-Ovchinnikov (FFLO) phase [43, 44].

When the spatial inversion symmetry (SIS) of the system is broken, Rashba-type spin spilit is expected. This cause another exotic phenomena as mentioned below.

Mixing of singlet and triplet

The first thing to be predicted in superconductors without SIS is generation of Cooper pairs with mixed state of singlet and triplet components [45, 46].

Here we define spatial inversion operator P. If the SIS is conserved, the wavefunction is eigenstate of P i.e. $P\Psi = \pm \Psi$. Actually, the operator P acts on the orbital factor as $P\psi_{\text{even}} = \psi_{\text{even}}$ or $P\psi_{\text{odd}} = -\psi_{\text{odd}}$. Then spatial inversion of a mixed state $\Psi = \Psi_{\text{even},s} + a\Psi_{\text{odd},t}$ is converted as

$$P\Psi = \Psi_{\text{even s}} - a\Psi_{\text{odd t}} \neq \pm\Psi. \tag{2.153}$$

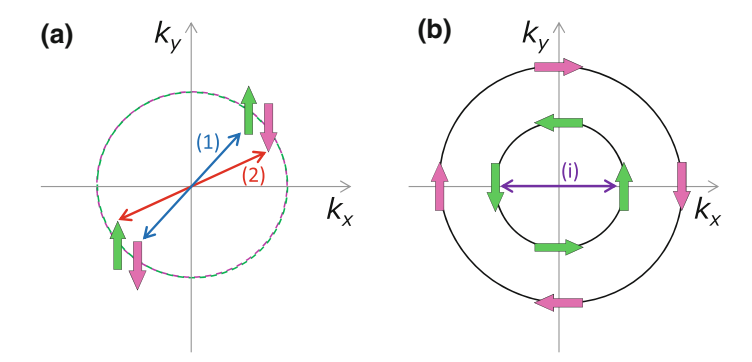


Fig. 2.17 a Schematic diagram of the Cooper pairing on a, a spin-degenerate Fermi circle and b a spin-split Fermi surface by Rashba effect

This indicates that parity is not conserved in the presence of SIS. However, once SIS is broken, mixed state becomes possible if the system has strong spin-orbit coupling.

In an usual spin-degenerate system, singlet Cooper pairs are formed at the Fermi level as

$$\frac{1}{\sqrt{2}}(\underbrace{|\mathbf{k},\uparrow\rangle|-\mathbf{k},\downarrow\rangle}_{(1)}-\underbrace{|\mathbf{k},\downarrow\rangle|-\mathbf{k},\uparrow\rangle}_{(2)}). \tag{2.154}$$

The term (1) and (2) are allowed to be taken from the spin-degenerate two states as shown in Fig. 2.17a. When the Rashba effect occurs, Fermi contour splits into two circles where spin rotates in opposite direction. Let us denote up spin as σ_{\uparrow} and down spin as σ_{\downarrow} when the spin quantization axis is parallel to $(-k_y, k_x, 0)$. Then, an electron pair with opposit momentums (i) $|\mathbf{k}, \sigma_{\uparrow}\rangle| - \mathbf{k}, \sigma_{\downarrow}\rangle$ (denoted as (i) in Fig. 2.17b) can be considered but the superposition with the counterpart state $|\sigma_{\downarrow}\rangle|\sigma_{\uparrow}\rangle$ is impossible when the energy separation due to Rashba effect E_{SO} is sufficiently large. Of course, the state (i) is not allowed actually because these are neither symmetric nor antisymmetric with respect to exchange of the two electrons, namely, parity is broken. In order to avoid this problem, we divide (i) $|\mathbf{k}, \sigma_{\uparrow}\rangle| - \mathbf{k}, \sigma_{\downarrow}\rangle$ into two term and add virtual states: $(-|\mathbf{k}, \sigma_{\downarrow}\rangle| - \mathbf{k}, \sigma_{\uparrow}\rangle + |\mathbf{k}, \sigma_{\downarrow}\rangle| - \mathbf{k}, \sigma_{\uparrow}\rangle)/2 \equiv 0$, leading to the pairing state of an admixture of a spin singlet state and a spin triplet state:

$$\underbrace{\left|\mathbf{k}, \sigma_{\uparrow}\rangle\right| - \mathbf{k}, \sigma_{\downarrow}\rangle}_{(i)} = \frac{1}{2} (\underbrace{\left|\mathbf{k}, \sigma_{\uparrow}\rangle\right| - \mathbf{k}, \sigma_{\downarrow}\rangle - \left|\mathbf{k}, \sigma_{\downarrow}\rangle\right| - \mathbf{k}, \sigma_{\uparrow}\rangle}_{\text{singlet}} + \frac{1}{2} (\underbrace{\left|\mathbf{k}, \sigma_{\uparrow}\rangle\right| - \mathbf{k}, \sigma_{\downarrow}\rangle + \left|\mathbf{k}, \sigma_{\downarrow}\rangle\right| - \mathbf{k}, \sigma_{\uparrow}\rangle}_{\text{triplet}}). \tag{2.156}$$

The first line in right hand is spin-singlet, while the second is a spin triplet state with with an in-plane spin projection equal to zero. If the quantization axis is redefined parallel to the *z*-axis, it corresponds to $|\mathbf{k},\uparrow\rangle|-\mathbf{k},\uparrow\rangle$ or $|\mathbf{k},\downarrow\rangle|-\mathbf{k},\downarrow\rangle$. So far, superconductivities have been found in several bulk materials with non-centrosymmetric crystal structures [47–51]. Though symmetry of the Cooper pair is discussed by nuclear magnetic resonance etc., there have is no clear evidence proving the mixing of singlet and triplet component.

Electromagnetic responses

Here we consider application of magnetic field to superconductors with strong Rashba effect. When the asymmetric potential gradient is parallel to the z-axis, for magnetic fields in same direction, Cooper pairs between electrons with the momenta \mathbf{k} and $-\mathbf{k}$ are always possible, because the spins in a branch of Fermi contour tilt to same direction as shown in Fig. 2.17a. This implies the suppression of the paramagnetic depairing effect. [52] However, this effect may not been observed because in most cases, orbital effect is dominant for perpendicular magnetic field.

For magnetic fields parallel to the *xy*-plane, on the other hand, the orbital pair breaking is prohibited in ultrathin 2D superconductors. The Fermi surfaces are deformed into asymmetric shapes as shown in Fig. 2.17b, resulting in the spatially non-uniform order parameter similar to the FFLO state called *stripe or helical phase* [53, 54]. Experimentally, the huge upper critical field observed in the Pb extreme thin film on GaAs seems to be originated from the helical phase [26].

References

- 1. S. LaShell, B. McDougall, E. Jensen, Phys. Rev. Lett. 77, 3419 (1996)
- M. Hoesch, M. Muntwiler, V. Petrov, M. Hengsberger, L. Patthey, M. Shi, M. Falub, T. Greber, J. Osterwalder, Phys. Rev. B 69, 241401 (2004)
- 3. L. Petersen, P. Hedegård, Surf. Sci. 459, 49 (2000)
- 4. M. Nagano, A. Kodama, T. Shishidou, T. Oguchi, J. Phys. Condens. Matter 21, 064239 (2009)
- C.R. Ast, J. Henk, A. Ernst, L. Moreschini, M.C. Falub, D. Pacilé, P. Bruno, K. Kern, M. Grioni, Phys. Rev. Lett. 98(18), 186807 (2007)
- 6. N.W. Ashcroft, N.D. Mermin, S. Rodriguez, Solid State Physics. (AAPT, 1978)
- F. London, H. London, Proceedings of the royal society of London a: mathematical. Phys. Eng. Sci. 149(866), 71 (1935)
- 8. J. Bardeen, L.N. Cooper, J.R. Schrieffer, Phys. Rev. 106, 162 (1957)
- 9. G. Rickayzen, Phys. Rev. **111**, 817 (1958)
- 10. G. Wentzel, Phys. Rev. 111, 1488 (1958)
- 11. L.P. Gorkov, Sov. Phys. JETP 9, 1364 (1959)
- 12. V. Ambegaokar, A. Baratoff, Phys. Rev. Lett. 10, 486 (1963)
- S. Yoshizawa, H. Kim, T. Kawakami, Y. Nagai, T. Nakayama, X. Hu, Y. Hasegawa, T. Uchihashi, Phys. Rev. Lett. 113, 247004 (2014)
- 14. T. Uchihashi, P. Mishra, M. Aono, T. Nakayama, Phys. Rev. Lett. 107, 207001 (2011)
- 15. S. Yoshizawa, H. Kim, Y. Hasegawa, T. Uchihashi, Phys. Rev. B 92, 041410 (2015)
- 16. J. Bardeen, Rev. Mod. Phys. **34**, 667 (1962)
- 17. W.L. McMillan, Phys. Rev. 167, 331 (1968)
- 18. P.B. Allen, R.C. Dynes, Phys. Rev. B **12**, 905 (1975)

References 51

 C.K. Poole, H.A. Farach, R.J. Creswick, Handbook of Superconductivity. (Academic Press, 1999)

- 20. C. Kittel, Introduction to Solid State Physics. (Wiley, 2005)
- 21. G.D. Mahan, Many-Particle Physics. (Springer Science & Business Media, 2013)
- 22. E. Plummer, J. Shi, S.J. Tang, E. Rotenberg, S. Kevan, Prog. Surf. Sci. 74, 251 (2003)
- J. Gayone, C. Kirkegaard, J. Wells, S. Hoffmann, Z. Li, P. Hofmann, Appl. Phys. A 80, 943 (2005)
- N. Reyren, S. Gariglio, A. Caviglia, D. Jaccard, T. Schneider, J. Triscone, Appl. Phys. Lett. 94, 112506 (2009)
- H.M. Zhang, Y. Sun, W. Li, J.P. Peng, C.L. Song, Y. Xing, Q. Zhang, J. Guan, Z. Li, Y. Zhao et al., Phys. Rev. Lett. 114, 107003 (2015)
- 26. T. Sekihara, R. Masutomi, T. Okamoto, Phys. Rev. Lett. 111, 057005 (2013)
- Y. Saito, Y. Nakamura, M.S. Bahramy, Y. Kohama, J. Ye, Y. Kasahara, Y. Nakagawa, M. Onga, M. Tokunaga, T. Nojima et al., Nat. Phys. 12, 144 (2015)
- 28. A. Larkin, A. Varlamov, Theory of Fluctuations in Superconductors. (Clarendon Press, 2005)
- 29. R.S. Thompson, Phys. Rev. B 1, 327 (1970)
- 30. B.I. Halperin, D.R. Nelson, J. Low Temp. Phys. **36**(5), 599 (1979)
- 31. K. Epstein, A. Goldman, A. Kadin, Phys. Rev. B 26, 3950 (1982)
- 32. K. Epstein, A. Goldman, A. Kadin, Phys. Rev. Lett. 47, 534 (1981)
- 33. A. Kadin, K. Epstein, A. Goldman, Phys. Rev. B 27, 6691 (1983)
- 34. A. Fiory, A. Hebard, W. Glaberson, Phys. Rev. B 28, 5075 (1983)
- 35. A. Hebard, A. Fiory, Phys. Rev. Lett. **50**, 1603 (1983)
- 36. J. Garland, H.J. Lee, Phys. Rev. B 36, 3638 (1987)
- 37. N. Reyren, S. Thiel, A. Caviglia, L.F. Kourkoutis, G. Hammerl, C. Richter, C. Schneider, T. Kopp, A.S. Rüetschi, D. Jaccard et al., Science 317, 1196 (2007)
- 38. T. Uchihashi, P. Mishra, T. Nakayama, Nanoscale Res. Lett. 8, 1 (2013)
- 39. R. Fazio, G. Schön, Physical Review B 43, 5307 (1991)
- 40. V.F. Gantmakher, V.T. Dolgopolov, Phys. Usp. **53**(1), 1 (2010)
- 41. D. Haviland, Y. Liu, A. Goldman, Phys. Rev. Lett. 62, 2180 (1989)
- 42. A. Yazdani, A. Kapitulnik, Phys. Rev. Lett. **74**, 3037 (1995)
- 43. P. Fulde, R.A. Ferrell, Phys. Rev. **135**, A550 (1964)
- 44. A. Larkin, Y. Ovchinnikov, Z. Eksp, Teor. Fiz 47, 1136 (1964)
- 45. L.P. Gor'kov, E.I. Rashba, Phys. Rev. Lett. **87**, 037004 (2001)
- 46. V. Edel'shtein, Soviet Phys. JETP **68**, 1244 (1989)
- 47. E. Bauer, G. Hilscher, H. Michor, C. Paul, E. Scheidt, A. Gribanov, Y. Seropegin, H. Noël, M. Sigrist, P. Rogl, Phys. Rev. Lett. **92**, 027003 (2004)
- 48. N. Kimura, K. Ito, K. Saitoh, Y. Umeda, H. Aoki, T. Terashima, Phys. Rev. Lett. 95, 247004 (2005)
- K. Togano, P. Badica, Y. Nakamori, S. Orimo, H. Takeya, K. Hirata, Phys. Rev. Lett. 93, 247004 (2004)
- 50. N. Kimura, K. Ito, H. Aoki, S. Uji, T. Terashima, Phys. Rev. Lett. 98, 197001 (2007)
- Y. Okuda, Y. Miyauchi, Y. Ida, Y. Takeda, C. Tonohiro, Y. Oduchi, T. Yamada, N. Duc Dung, T.D. Matsuda, Y. Haga et al., J. Phys. Soc. Jpn. 76, 044708 (2007)
- 52. S. Fujimoto, J. Phys. Soc. Jpn. 76, 051008 (2007)
- 53. O.V. Dimitrova, M.V. Feigel'man, J. Experimental Theoretical Phys. Lett. 78(10), 637 (2003)
- 54. O. Dimitrova, M.V. Feigel'man, Phys. Rev. B **76**, 014522 (2007)

Chapter 3 Experimental Methods

Abstract The experimetal works in this thesis owing to an ultrahigh vacuum system, in which surface conductivity is measured in situ by four-point-probe method down to 0.8 K, combined with surface preparation/analysis capability by reflection-high-energy-electron-diffraction. This chapter begins with the principle of electron diffraction and four-point-probing, including dual configuration method for the reduction of data scattering, and followed by actual setup, including the cooling procedure of the cryostat.

Keywords Electron diffraction · Electrical transport · Four-terminal measurement · Ultrahigh vacuum · Low-temperature

3.1 Electron Diffraction

In this study, the reflection high-energy electron diffraction (RHEED) is employed to characterize the crystalline structures. The RHEED is a kind of electron diffraction techniques, where electron beam strikes the sample at a very small angle relative to its surface. It makes the RHEED a highly surface sensitive tool and suitable to in situ observation during sample growth by the molecular beam epitaxy. Figure 3.1a shows a schematic illustration of a typical RHEED system; It requires an electron gun, photoluminescent detector screen to be projected diffraction patterns and a sample with a clean surface, which is used as a substrate for epitaxial growth by metal deposition.

A de Broglie wavelength λ_d of an electron accelerated by voltage V [volt] is given by

$$\lambda_d = \frac{h}{p} = \frac{h}{\sqrt{2meV}} = \sqrt{\frac{150.412}{V}} [\text{Å}] \text{ (non-relativistic)}. \tag{3.1}$$

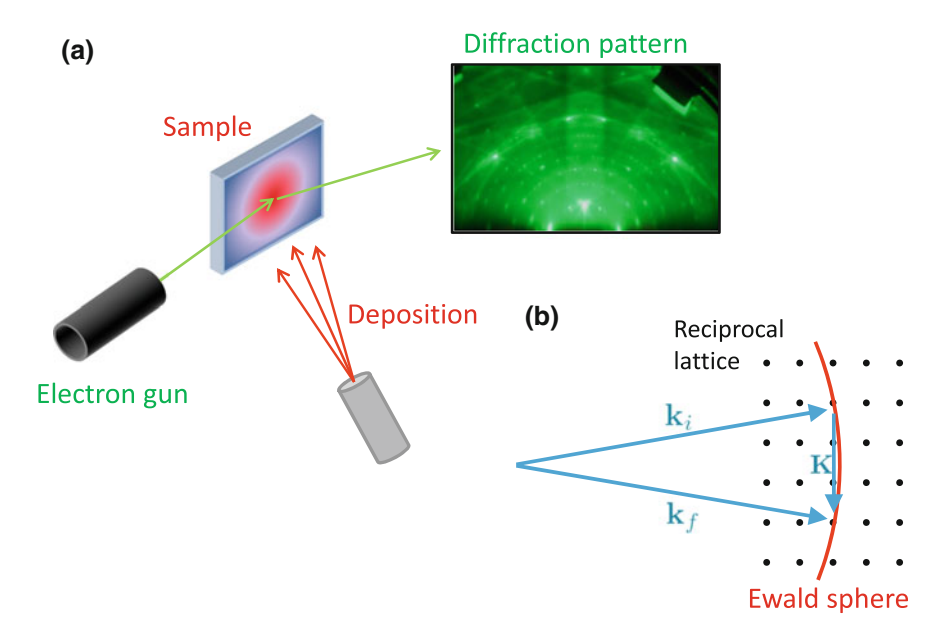


Fig. 3.1 a Conceptual diagram of molecular beam epitaxy in UHV, where vapor depositionis performed with monitoring the surface structure by RHEED in situ. **b** Schematic of Ewald construction. The reflected diffraction wave is excited in the direction in which the surface of the Ewald sphere, having a radius equal to the incident wave number, overlaps the reciprocal lattice point of the crystal

The electron with energy of 15 keV corresponds to $\lambda_d \sim 0.1$ Å. Since this is comparable to the interatomic distance, incident electrons diffract from atoms at the surface of the sample and a part of the diffracted electrons interfere at specific angles, resulting in regular diffraction patterns. Let us define the wavenumber vectors of incident and diffracted electron as \mathbf{k}_i and \mathbf{k}_f . The total amplitude of diffracted wave $A(\mathbf{K} = \mathbf{k}_f - \mathbf{k}_i)(\mathbf{K}$ is scattering vector) is superposition of the localy scattered waves from surface atoms. The scattering amplitude of a spherical wave by an isolated atom is called atomic scattering factor $f(\mathbf{K})$. The diffraction pattern is determined by unit cell of surface structure; its geometry and intensity are given by Laue function $L(\mathbf{K})$ and structure factor $F(\mathbf{K})$.

$$A(\mathbf{K}) = \sum_{j \text{(all atoms)}} f_j \exp(-i\mathbf{K} \cdot \mathbf{r}_j)$$

$$= \left[\sum_{n \text{(all unit cell)}} \exp(-i\mathbf{K} \cdot \mathbf{R}_n) \right] \times \left[\sum_{u \text{(in unit cell)}} f_u \exp(-i\mathbf{K} \cdot \mathbf{r}_u) \right]. \quad (3.2)$$

3.1 Electron Diffraction 55

The Laue function $L(\mathbf{K})$ reaches the primary maxima when scattering vector \mathbf{K} satisfies the Laue condition:

$$\mathbf{K} \cdot \mathbf{a} = h, \quad \mathbf{K} \cdot \mathbf{b} = k, \quad \mathbf{K} \cdot \mathbf{c} = l,$$
 (3.3)

where \mathbf{a} , \mathbf{b} , \mathbf{c} are primitive vectors for a direct lattice and h, k, l is integer. Primitive vectors for a reciprocal lattice are denoted as

$$\mathbf{a}^* = \frac{\mathbf{b} \times \mathbf{c}}{\mathbf{a} \cdot (\mathbf{b} \times \mathbf{c})}, \quad \mathbf{b}^* = \frac{\mathbf{c} \times \mathbf{a}}{\mathbf{a} \cdot (\mathbf{b} \times \mathbf{c})}, \quad \mathbf{c}^* = \frac{\mathbf{a} \times \mathbf{b}}{\mathbf{a} \cdot (\mathbf{b} \times \mathbf{c})}.$$
 (3.4)

If we use these vectors instead of those for direct lattice, the Laue condition is rewritten as

$$\mathbf{K} = h\mathbf{a}^* + k\mathbf{b}^* + l\mathbf{c}^*. \tag{3.5}$$

Namely, arbitrary reciprocal vector satisfies the Laue condition.

In order to connect the real crystallographic properties of the sample surface and observed diffraction patterns, Ewald's spheres are used, which show the allowed diffraction conditions for kinematically scattered electrons in a given setup. The Ewald's sphere is put to be centered on the sample surface with a radius equal to the length of the wavenumber of the incident electrons, A scattering vector satisfying the Laue condition can be found when some reciprocal lattice points lie on the surface of the Ewald's sphere, starting from one to another (see Fig. 3.1b). The procedure of Ewald's sphere analysis is almost same as for bulk crystals, however the reciprocal lattice for the 2D case differs from that for a 3D one. The reciprocal lattices of bulk crystals is 3D because it is converted from 3D direct lattices. In 2D crystal, however, there are no diffraction conditions in the dimension perpendicular to the 2D system. Due to the lack of a third diffracting condition, the reciprocal lattice of a 2D crystal is a series of infinite rods extending perpendicular to the 2D space. Diffraction conditions are satisfied where the rods of reciprocal lattice intersect the Ewald's sphere as shown in Fig. 3.2a. Since the rods stand regularly and perpendicularly on the 2D reciprocal lattice, they slice the Ewald's sphere, producing sets of diffraction spots along concentric arcs $(L_0, L_1, L_2, ...)$ as seen in Fig. 3.2b. These spots are projected on the detector screen. The distance between neighboring spots corresponds to reciprocal of direct lattice constant. In actual experiment, spots have finite size because it depends on the size of crystal i.e. domain size. Observation of sharp spots indicates large domain size and successful growth of epitaxial materials.

In this study, irradiated area by electron beam is $100 \,\mu\text{m}$ while the substrates have area of $2 \times 5 \,\text{mm}^2$.

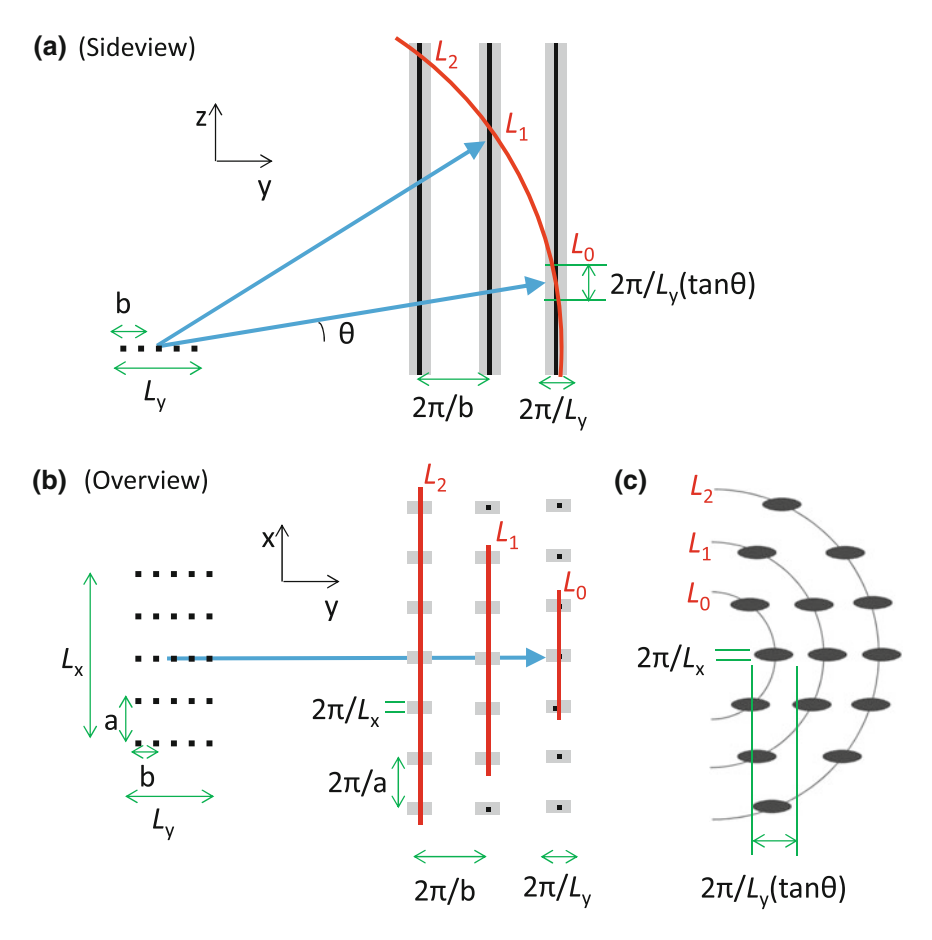


Fig. 3.2 Schematic explanation of RHEED pattern formation from a two-dimensional crystal with lattice constant (a, b) and size (L_x, L_y) . a Sideview and b topview of reciprocal rods. c Expected diffraction pattern

3.2 Electrical Transport Measurement

Four-point-probe method

The four terminal method is known as an electrical resistance measuring technique that uses separate pairs of current-carrying and voltage-sensing electrodes to eliminates inaccuracy attributable to lead resistance. If it is possible to process the sample in experimental rooms, we can prepare ohmic contacts at the edge of sample by various conventional methods. When we have to treat samples in vacuum chambers, only mechanical ways are available to get electrical contacts to 2DES in samples. Multi-point-probe devices provide the simplest solution; the tips land on the surface driven by piezo actuators and work as electrodes.

In this study, we focus on electrical conductivity of metal-adsorbed surfaces or atomic sheet materials put on surfaces of semiconductor substrates. In order to realize surface sensitive conductivity measurement, we have to suppress the other electrical pathways including bulk and space charge layer of substrate. One possible ways is to reduce the probe spacing down to ca. 10 μ m by using micro-four-point-probe [1] or multi-probe STM [2]. When a surface (or a 2D system put on surface) has metallic property, its conductivity increases at low temperature while that of substrate decreases to ignorable order [3–5]. In this study, doped semiconductors (n-type, 1.5–5 Ω cm) are used as substrates. Since resistances of these substrates exceed G Ω , only the surface contributes to 2D conductivity less than 50 K, although a macroscopic four-point-probe with spacing of 200 μ m is used.

A conductivity measurement is performed using the four tips as electrodes in contact with a conducting surface. A current I is driven through the sample between two current injection electrodes at \mathbf{r}_+ and \mathbf{r}_- and the potential difference V is then measured between two remaining electrodes at \mathbf{r}_1 and \mathbf{r}_2 . When the tips are aligned linearly, a relationship between experimentally obtained resistance $R_{\rm exp}$ and true sheet resistivity $R_{\rm sheet}$ is given by following equation [6].

$$R_{\text{exp}} = \frac{V}{I} = \frac{R_{\text{sheet}}}{2\pi} \ln \frac{|\mathbf{r}_1 - \mathbf{r}_-||\mathbf{r}_2 - \mathbf{r}_+|}{|\mathbf{r}_1 - \mathbf{r}_+||\mathbf{r}_2 - \mathbf{r}_-|}.$$
 (3.6)

For an equidistant collinear four-point probe with electrode pitch s, R_{sheet} can be calculated by usual four-terminal configuration; outer two are used for current injection while voltage is detected by inner two as

$$R_{\text{exp}} = \frac{V}{I} = \frac{R_{\text{sheet}}}{2\pi} \ln \frac{2s \cdot 2s}{s \cdot s} = \frac{\ln 2}{\pi} R_{\text{sheet}}.$$
 (3.7)

However, this equation does not work if the four electrodes are collinear but not equidistant. Then the exact sheet resistance R_{sheet} may be extracted numerically with the dual configuration method based on conformal mapping.

Let us redefine the four contact points as A(a, 0), B(b, 0), C(c, 0), D(d, 0) (a < b < c < d), same as shown in Fig. 3.3a. Here we have possible nontrivial electrode combinations of current and potential electrodes, excluding polarity changes which only result in sign change of the measured potential as we can see in Eq. (3.6). Then, following three "resistivities" are independent each other.

- 1. $R_A = (\text{current from } D \text{ to } A)/(\text{voltage between } C \text{ and } B)$
- 2. $R_B = (\text{current from } B \text{ to } A)/(\text{voltage between } C \text{ and } D)$
- 3. $R_C = (\text{current from } C \text{ to } A)/(\text{voltage between } D \text{ and } B)$

Figure 3.3b shows the configuration of R_A and R_B . According to Eq. (3.6),

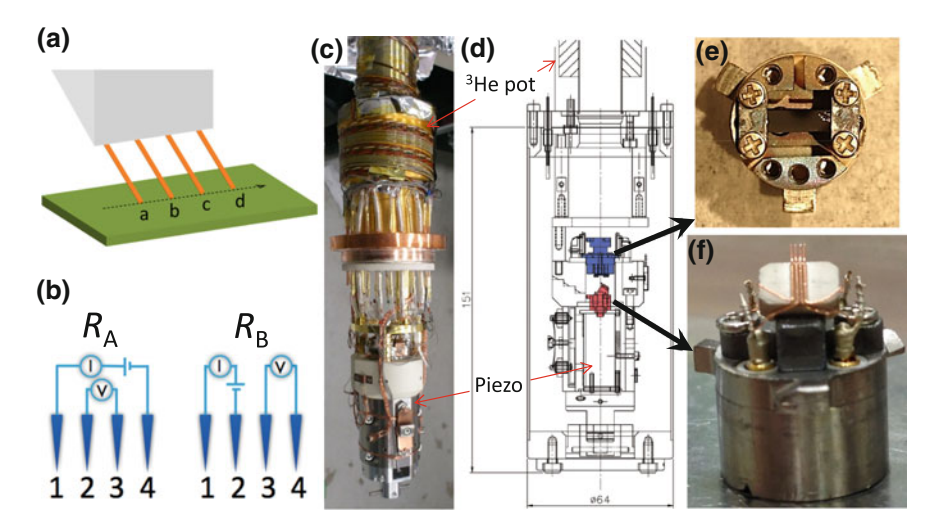


Fig. 3.3 a Schematically drawn four-point-probe. **b** Two configurations to measure R_A and R_B used in the "dual configuration" calculation. **c** Photograph and **d** drawing of STM head. Positions of the ³He pot and piezo driver are indicated by arrows. **e** Photograph of a sample holder. Active region between electrical terminals has area of ca. $2 \times 5 \text{ mm}^2$. **f** Photograph of the four point probe, consisting of four copper wires with ϕ 100 μ m diameter and 200 μ m spacing

$$R_A = \frac{R_{\text{sheet}}}{2\pi} \ln \frac{(c-a)(d-b)}{(d-c)(b-a)},$$
(3.8)

$$R_B = \frac{R_{\text{sheet}}}{2\pi} \ln \frac{(c-a)(d-b)}{(c-b)(d-a)},$$
 (3.9)

$$R_C = \frac{R_{\text{sheet}}}{2\pi} \ln \frac{(d-a)(c-b)}{(d-c)(b-a)},$$
(3.10)

resulting in $R_C = R_A - R_B$. Therefore, there remain only two independent resistances. True sheet resistivity of sample R_{sheet} is calculated from measured R_A and R_B by an identical equation regardless of in-line position errors relative to the electrode pitch:

$$\exp\left(-\frac{2\pi R_A}{R_{\text{sheet}}}\right) + \exp\left(-\frac{2\pi R_B}{R_{\text{sheet}}}\right) = \frac{(d-c)(b-a)}{(c-a)(d-b)} + \frac{(c-b)(d-a)}{(c-a)(d-b)} = 1$$
(3.11)

This method is called dual configuration technique, which is used throughout this thesis [7–10].

When external magnetic field is applied along surface normal,

$$R_{\text{exp}} = \frac{V}{I} = \frac{R_{\text{sheet}}}{2\pi} \left(1 + \frac{R_H^2}{R_{\text{sheet}}^2} \right) \ln \frac{|\mathbf{r}_1 - \mathbf{r}_-||\mathbf{r}_2 - \mathbf{r}_+|}{|\mathbf{r}_1 - \mathbf{r}_+||\mathbf{r}_2 - \mathbf{r}_-|}, \tag{3.12}$$

where R_H is Hall resistance [11]. Hence, output value from the dual configuration measurement is corrected as $R_{\rm sheet}(1+R_H^2/R_{\rm sheet}^2)$, where the second term corresponds to Hall effect. In this study, however, this classical effect is negligible because we focus on the magnetic response with respect to low field where superconducting transition and quantum interference are much more dominant than the classical Hall effect.

3.3 Experimental Apparatus

In 2003, a newly developed UHV system for the monolithic micro-four-point probes combined with a cryostat is constructed by Tanikawa et al. [12]. This system has contributed to investigation of conductive properties of various surface systems from room temperature to 10 K. Though this is enough for observing carrier scattering mechanism at the surface layers of crystals but not for quantum transport phenomena such as superconductivity and weak localization. Actually, an observation of superconductivity on Si(111)- $\sqrt{7} \times \sqrt{3}$ -In surface superstructure was reported with the critical temperature below 2K in an UHV-conductivity measurement system with He-flow type cryostat [13]. In order to investigate more detailed properties of the superconductivity, we need a measurement with stable temperature controlling around 1 K and also high magnetic field. An UHV equipment combined with such extreme conditions had already been commercialized for the STM by Unisoku Co. (model USM1300 [14]). In this study, the four-point-probe is integrated in this system instead of the single STM tip. Figure 3.4a, c is the design drawings and photo of whole the UHV system. The system is composed of three chambers, a load-lock chamber, a preparation chamber, and a main chamber, separated from each other by gate valves. The load-lock chamber is pumped by a turbo-molecular pump, while the preparation chamber and main chamber are pumped together by an ion pump to reach 10^{-9} Pa vacuum. The sample is introduced from the load-lock chamber and transferred into the preparation chamber by using a transfer rod. Thus it is possible to exchange the sample without breaking vacuum of the preparation and main chambers. The preparation chamber contains Jule heating, RHEED system and five evaporators. The sample can be prepared by MBE technique with in situ RHEED observation. The main chamber contains a long UHV pipe with a STM head at the bottom and inserted in a liq. ⁴He tank. A superconducting magnet is set at the bottom of the tank, which can apply the magnetic field up to 7 T in the direction perpendicular to the sample surface. Figure 3.4d is a schematic illustration of the cooling system. Liq. ⁴He is introduced from the tank into a 1 K Pot pumped by an oil-free pump to reach around 2 K (yellow part in Fig. 3.4d). ³He gas is confined in the green part in Fig. 3.4d. The 1 K Pot cools down this part and ³He is liquefied in a ³He Pot. In the green part, there is a sorption pump for decompressing the ³He Pot. The sorption pump is cooled by ⁴He vapor from the 1 K Pot, so that charcoal in the sorption pump adsorbs ³He vapor in the ³He Pot to make the pressure in the green part down to about 1 Pa. By this decompression, the ³He Pot, together with the measuring head which is

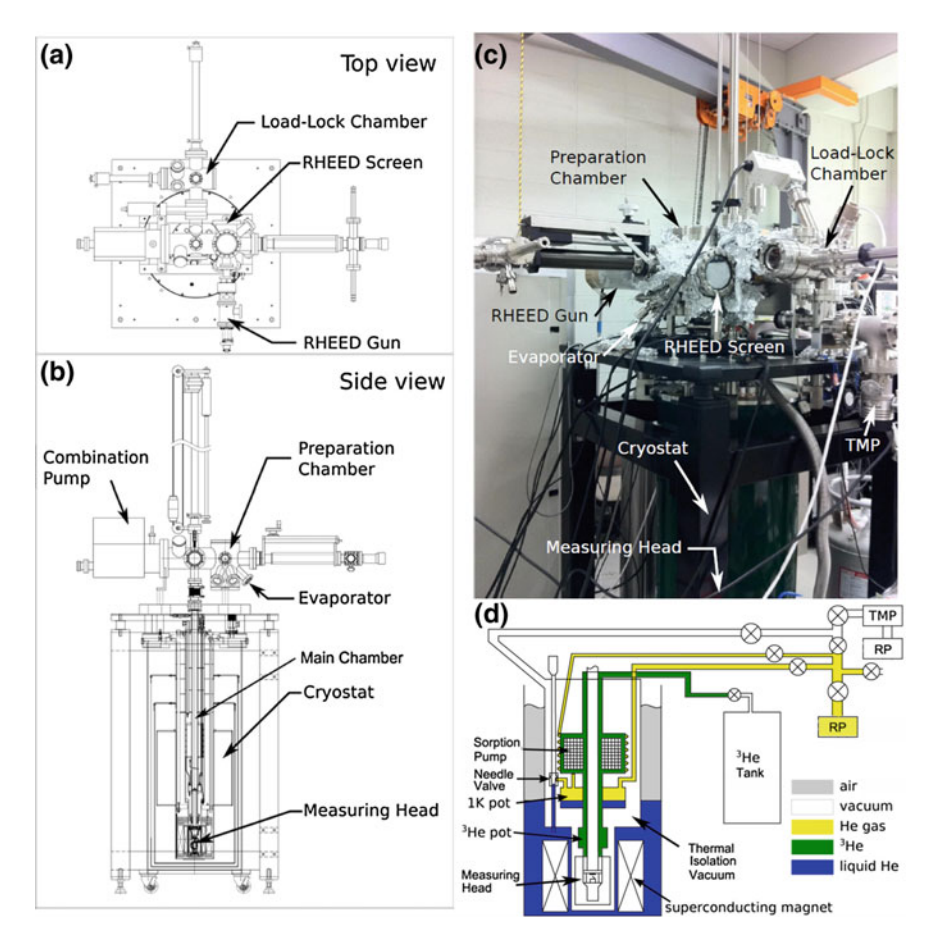


Fig. 3.4 Whole design drawings of the experimental apparatus [15] from **a** topview and **b** sideview. **c** Photograph of the apparatus. **d** Schematic diagram of cooling system. Reprinted with permission from Ref. [15]

thermally anchored to the ³He Pot, are cooled down to the lowest temperature. Actual using of ³He gas gives the best lowest temperature of 0.3 K for several days. Stable condition in long-term is required for STM/S measurements, such as differencial conductance mapping to obtain Fourier transformed patterns of electronical standing wave. In conductance measurement, however, such serious stability is not important because all we do is just repeating the cycle of sweeping temperature and magnetic field and each running is finished within an hour. Therefore confining ⁴He instead of ³He gas in the green part of Fig. 3.4d is enough, even if ⁴He realizes only 0.8 K for several hours due to its higher boiling point and unintentional thermal contact by its superfluidity.

The four-point-probe is made by copper wires with diameter of ϕ 100 μ m, which is mounted on the STM head. The resistivities $R_{A,B,C}$ are obtained from linear fitting of DC current-voltage characteristic with least square method by the home-made measurement circuit and software. The voltage differences between any pair of probes of the four are always measured while current injection probes are switched automatically for dual configuration measurement. For zero-bias resistivity measurement, 5000-10000~(I,V) points are acquired and stored in PC during one sweeping of the current by 10 kHz for one configuration. Then the scanning range of the current is limited within \pm 10 μ A to avoid Jule heating and non-linear effect. The obtained $R_{A,B,C}$ are immediately converted into $R_{\rm sheet}$ calculated by the software using dual configuration method. To see the non-linear I-V characteristic, one can expand the current range to \pm 250 μ A. In particular, for the measurement of critical current of superconductivity, Jule heating effect should be suppressed. So one-shot current sweeping by R_A configuration is performed instead of continuous scanning of current and other probe configurations.

The four-point-probe is approached to/retracted from a sample surface by piezo actuator, which is applied pulse voltage from a controller. During the probe approach, the pulse voltage is applied consecutively (auto-mode) as a bias voltage is applied and flowing current is monitored between tips and a sample. Once the current is detected by one of the four probes, the probe motion is stopped and switched from auto-mode to manual mode to make soft direct contact for all probes.

The application of magnetic field is operated by usual commercialized controller supplied by Cryogenic. For the temperature, current is applied to a hand-made heater put on the STM head from a temperature controller of Lakeshore (model 340). This one can stabilize the temperature at any setpoint value with high accuracy, This is sufficient for STM measurement, where scanning is performed for a long time at fixed temperature. In order to observe critical temperature of phase transitions by resistivity measurement, temperature must be swept continuously and gently to keep thermal equilibrium condition. Hence I prepared a home-made softwares to monitor the resistivities continuously and to increase the temperature-setpoint by enough small steps (6 mK per minute, at the smallest).

References

- S. Yamazaki, Y. Hosomura, I. Matsuda, R. Hobara, T. Eguchi, Y. Hasegawa, S. Hasegawa, Phys. Rev. Lett. 106, 116802 (2011)
- S. Yoshimoto, Y. Murata, K. Kubo, K. Tomita, K. Motoyoshi, T. Kimura, H. Okino, R. Hobara, I. Matsuda, S.I. Honda, et al. Nano Lett. 7, 956 (2007)
- 3. R.A. Smith, Semiconductors (Cambridge Univ, Press, 1978)
- 4. S.M. Sze, K.K. Ng, Physics of Semiconductor Devices (Wiley, New York, 2006)
- 5. S. Hatta, T. Noma, H. Okuyama, T. Aruga, Phys. Rev. B 90, 245407 (2014)
- 6. F. Smits, Bell Syst. Tech. J. 37, 711 (1958)
- L. Van der Pauw, Philip. Tech. Rev. 20, 220 (1958)
- 8. R. Rymaszewski, J. Phys. E Sci. Instrum. 2, 170 (1969)

- D.H. Petersen, R. Lin, T.M. Hansen, E. Rosseel, W. Vandervorst, C. Markvardsen, D. Kjær, P.F. Nielsen, J. Vac. Sci. Technol. B 26, 362 (2008)
- D.H. Petersen, O. Hansen, T.M. Hansen, P. Bøggild, R. Lin, D. Kjær, P.F. Nielsen, T. Clarysse, W. Vandervorst, E. Rosseel, et al., J. Vac. Sci. Technol. B Nanotechnol. Microelectron. Mater. Process. Meas. Phenom. 28(1), C1C27 (2010)
- 11. D.H. Petersen, O. Hansen, R. Lin, P.F. Nielsen, J. Appl. Phys. **104**, 013710 (2008)
- 12. T. Tanikawa, I. Matsuda, R. Hobara, S. Hasegawa, E-J. Surf. Sci. Nanotechnol. 1, 50 (2003)
- 13. T. Uchihashi, P. Mishra, M. Aono, T. Nakayama, Phys. Rev. Lett. 107, 207001 (2011)
- 14. M. Ono, T. Nishio, T. Eguchi, Y. Hasegawa, E-J. Surf. Sci. Nanotechnol. 2, 165 (2004)
- M. Yamada, T. Hirahara, R. Hobara, S. Hasegawa, H. Mizuno, Y. Miyatake, T. Nagamura, E-J. Surf. Sci. Nanotechnol. 10, 400 (2012)

Chapter 4 Thallium Biatomic Layer

Abstract Thallium, the heaviest element among Group III metals, composes one of the essential parts of cuprate high- $T_{\rm c}$ superconductors. Surprisingly, however, there is few reports of superconductivity in pure Tl. Due to instability of the element, it is difficult to grow large single crystal and superconductivity is reported on only disordered thin films. In this chapter, the first observation of superconductivity in a double atomic layer of Tl epitaxially grown on Si(111) substrate using in situ electrical resistivity measurements in ultrahigh vacuum. Macroscopic superconducting transition was found at 0.96 K, accompanied by thermal and quantum fluctuations of order parameter. The system also demonstrates a perpendicular-magnetic-field-induced superconductor-insulator transition, together with an intermediate metallic state. The magnetic field dependence of the intermediate state is consistent with the Bose metal picture, which is a consequence of strong quantum fluctuations.

Keywords Thallium · Silicon · Surface · Superconductivity · Fluctuation

4.1 Background

This the heaviest element among Group III metals. Thinduced surface reconstructions of Si(111) have already been found to exhibit a set of interesting phenomena. Since Thas a variable valency of one or three, It induces the both $\sqrt{3} \times \sqrt{3}$ periodicity [1, 2] like other Group III metals and the 3×1 periodicity [1, 3] that is typical for alkali metals. One monolayer of Thorms a specific 1×1 reconstruction [1, 4, 5] having a structure of a pseudomorphic layer where Thatoms occupy every T_4 sites atop a bulk-cleaved Si(111) surface as shown in Fig. 4.1a [6–8]. The 1×1 -Threconstruction has recently attracted a great attention due to a large spin-splitting and valley-degree of freedom of its surface bands [9–15]. However, as shown in Fig. 4.1b, 1×1 -Threconstruction the spin spin splitting and valley-degree of freedom of its surface bands [9–15]. However, as shown in Fig. 4.1b, 1×1 -Threconstruction the spin spin splitting is associated with extra Thatoms on the 1×1 -Threconstruction filling is associated with extra Thatoms on the 1×1 -Threconstruction for specific surface defects [5]. Figure 4.1c

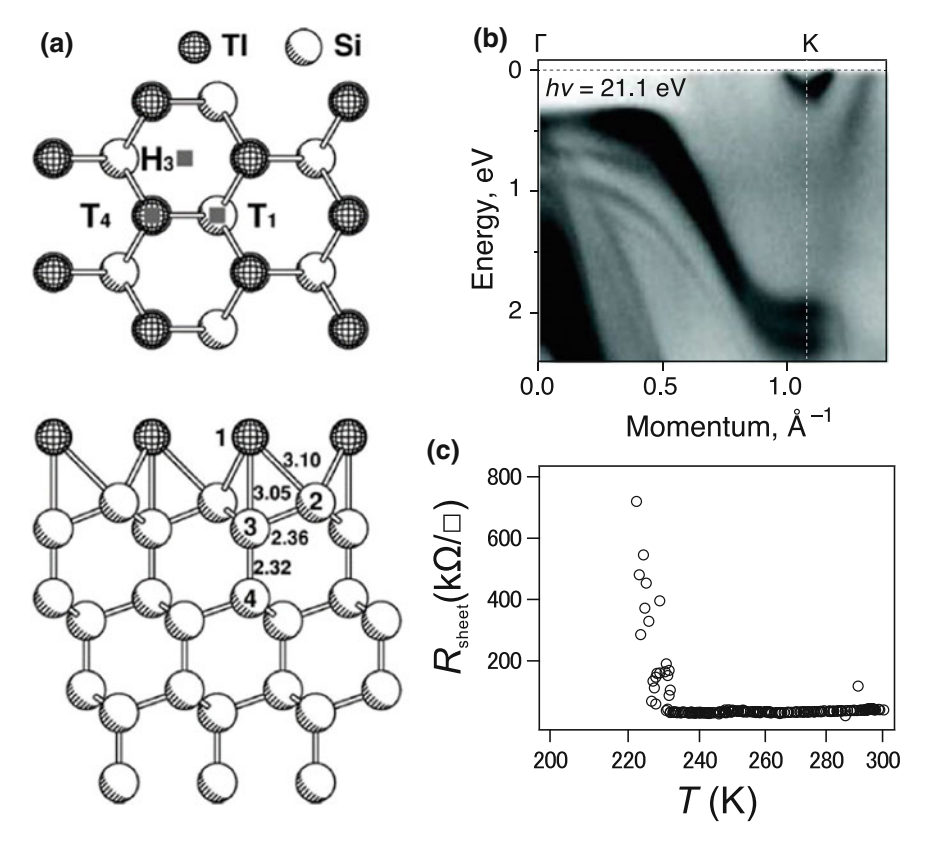


Fig. 4.1 Properties of 1×1 -Tl surface. a Schematic crystal structure [45]. b Band dispersion obtained by the ARPES measurement [25]. c Sheet resistivities as a function of temperature, showing abrupt uprise at 230 K [25]. Reprinted with permission from Refs. [25, 45]

show temperature dependent sheet resistivities $R_{\text{sheet}}(T)$ of the 1 × 1-Tl. The 1 × 1-Tl becomes insulating immediately after cooling from room temperature. This is in consistent with the previous reports by ARPES, suggesting its insulating nature [9, 11, 12].

4.2 Structural Properties of Si(111)-6 \times 6-Tl

4.2.1 Atomic Arrangement

When further Tl is deposited onto the Si(111)-1 × 1-Tl surface, formation of the double-layer Tl phase takes place. In large-scale scanning tunnel microscope (STM) images it appears as bright regions (Fig. 4.2a). The apparent height of the double-

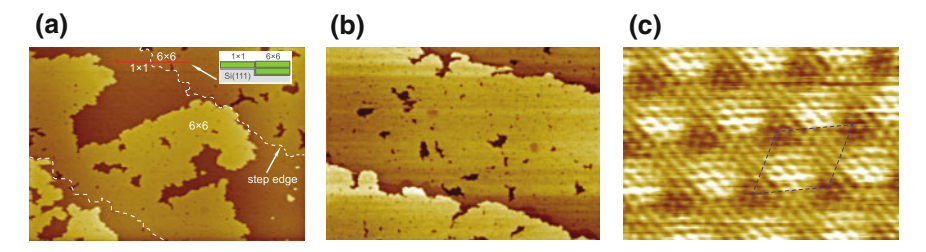


Fig. 4.2 Large-scale $(800 \times 600 \, \text{nm}^2)$ STM images at **a** intermediate and **b** final stages of the formation of the 6×6 -Tl phase upon deposition of Tl onto Si(111)-1 \times 1-Tl surface held at 200 °C [25]. Inset in **a**, shows a schematic picture of the Tl atomic layers on Si(111) along the red line in STM image which crosses an atomic step (indicated by dashed white line). **c** High-resolution $(10 \times 7.5 \, \text{nm}^2)$ STM image exhibiting moiré structure of the bilayer Tl [25]. The 6×6 unit cell is outlined by a blue dashed line. Reprinted with permission from Ref. [25]

layer phase almost coincides with that of the 1×1 -Tl phase on the upper terrace of bare Si(111) surface as illustrated in the inset in Fig. 4.2a. Figure 4.2c displays a high-resolution STM image, where the double-layer Tl phase demonstrates a 6×6 periodicity. It is revealed that the periodic structure is associated with developing of the moiré pattern within the array which preserves basic 1×1 periodicity. The double-layer 6 × 6-Tl phase is completed when somewhat more than 1 ML Tl is added on the 1×1 -Tl surface (Fig. 4.2b). Any overdosing of Tl (deposition of additional Tl onto the completed 6×6 -Tl phase) destabilizes the Tl biatomic layer, which collapses into 3D islands restoring the 1-ML 1×1 -Tl structure on the baring surface. Vitali et al. [4, 16] studied the Tl double-layer phase on Si(111) by STM/S and considered such kind of instability as a sign of its structural "softness". They carefully examined the moiré pattern which reveals that the distribution of maxima is not oriented along a unique direction. In other words, the two layers have rotational angle, indicating the quite weak interlayer coupling of them. Indeed, the lattice constant is different depending on number of layers; it is ca. 3.3 Å on toplayer of 6×6 -Tl while 3.84 Å on 1×1 -Tl. The bilayer one is rather close to the value of bulk Tl (3.46 Å). From the experimental results above, it is concluded that the biatomic layer of thallium is at a metastable condition, where wettability competes with condensation energy to 3D structure.

4.2.2 Electronic Structure

Electronic structure of the double-layer 6×6 -Tl phase were examined by the ARPES. The results are presented in the form of the spectra along the $\overline{\Gamma}$ - \overline{K} direction and Fermi surface maps as shown in Figs. 4.3a and b.

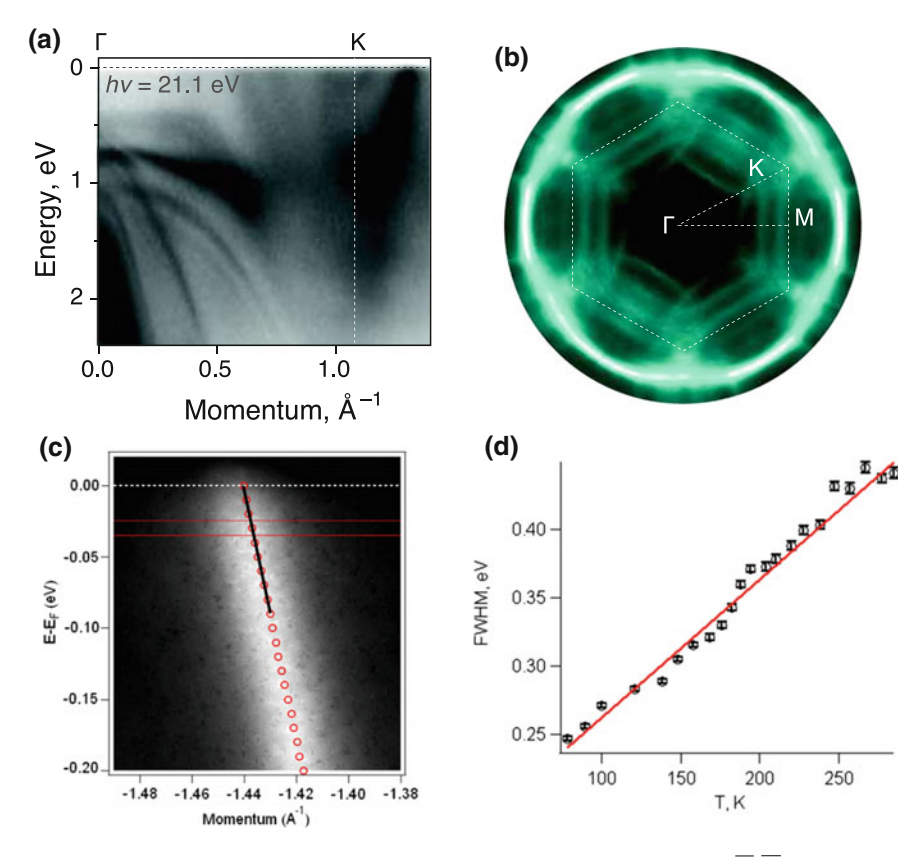


Fig. 4.3 Spectoscopic studies of 6×6 -T1. **a** Electrical band dispersion along $\overline{\Gamma}$ - \overline{K} direction and **b** Fermi surface [25]. **c** Close-up band dispersion at the vicinity of Fermi energy. The red circle represents the peak positions in the MDC spectrum and the black line represents the slope of the dispersion. The distance between the red lines indicates the spectrum width in the energy direction [17]. **d** Temperature dependence of the spectrum width. The results of linear fitting is shown by the red line [17]. Reprinted with permission from Ref. [25]

As mentioned earlier, the initial 1×1 -Tl surface has basically semiconducting structure. With formation of the 6×6 Tl double layer, a distinct metallic surface-state band develops. The Fermi surface map Fig. 4.3b shows up that the inner contour has a shape of a concave hexagon. This is apparently a folded Fermi contour from the large, bright, and almost circular one located in the second 1×1 surface Brillouin zones (SBZs) into the first SBZ. The other less distinct contours are also believed to be replica contours. Namely, they are not related to the real electron band structure of the Tl double layer, but just results from interference of the ejected photoelectrons with the periodic potential of the moiré structure at the surface. Evidently, the replica bands have almost the same velocity when crossing the Fermi level and no minigaps at the crossing points. Therefore, the Fermi wavenumber of true band can be estimated as $k_F \sim 1.4 \text{ Å}^{-1}$. The Fermi velocity, the gradient of dispersion near Fermi level is

 $v_F = 1.3 \times 10^8$ cm/s and effective mass $m^* = 1.2 m_e$. Career density is estimated as $n = 3.1 \times 10^{15}$ cm⁻² by applying free electronic approximation: regarding the Fermi surface as circular one.

As mentioned in Sect. 2.4.1, strength of electron-phonon coupling (EPC) is associated with emergence of superconductivity and the EPC constant λ can be extracted from the slope of the temperature T dependence of the spectral energy width of a surface state band ΔE according to the relation $\lambda = (d\Delta E/dT)/(2\pi k_B)$, where k_B is the Boltzmann constant [17]. The ΔE value was obtained as the product of Δk , which is defined as the width of the Lorentzian function fit to the momentum distribution curves (MDC) [18], with the gradient of the dispersion dE/dk near the Fermi level (see Fig. 4.3c). Finally, EPC constant λ was determined from a linear fit to the ΔE -T plots. Temperature range chosen was beyond 80 K in order to exceed the Debye temperature θ_D which is known to amount 79 K for bulk Tl [19]. Figure 4.3d shows typical $\Delta E - T$ plots with the results of EPC constant λ evaluation for a particular experimental run. A set of experiments performed to yield $\lambda = 1.86 \pm 0.02$. For comparison, the known superconducting In and Pb monolayers on Si(111) demonstrate lower values of λ , 0.8–1.0 for In [20] and 0.6–0.9 for Pb [21]. Therefore, enhanced EPC in Tl bilayer provides a promise for observing strong coupled superconductivity in this system.

According to McMillan's equation (2.130)

$$T_{c} = \frac{\hbar\omega_{D}}{1.45k_{B}} \exp\left(-\frac{1.04(1+\lambda)}{\lambda - \mu^{*}(1+0.62\lambda)}\right),\tag{4.1}$$

the superconducting transition temperature is estimated as $T_c = 7.9-8.9 \,\mathrm{K}$, if the surface has $\theta_D = 79 \,\mathrm{K}$, same as the bulk Tl.

4.3 Purpose of This Study

Although the STM and ARPES studies on 6×6 -Tl revealed its metallic nature, its ground state has not been explored. It is demonstrated that the system has the strong electron-phonon coupling by temperature–dependent ARPES, promising for the emergence of superconductivity. According to the structural studies, Tl biatomic layer is a metastable state. It is destabilized by slight amount of excess/deficiency of Tl and collapses into more stable 1×1 -Tl or 3D clusters. This is different from the previous examples of superconducting surface reconstructions on silicon such as In/Si(111) [22–24] and Pb/Si(111) [22, 24]. They are stable wetting layer of silicon surface and can coexist with In or Pb 3D islands. In order to clarify its low-temperature state and the effect of the instability, the in situ electrical transport tests was conducted at low temperature.

The following results and discussions are based on the content of a published article [25]: "Superconductivity in thallium double atomic layer and transition into an insulating phase intermediated by a quantum metal state" S. Ichinokura, L. Bondarenko, A. Tupchaya, D. Gruznev, A. Zotov, A. Saranin, and S. Hasegawa: 2D Materials **4**, 025020 (2017).

4.4 Electrical Transport Studies on Si(111)-6 \times 6-Tl

4.4.1 Sample Preparation

The in-situ electronic resistivity measurements were performed with the UHV-4PP system, equipped with RHEED for sample characterization with deposition [26].

Atomically-clean Si substrates were prepared in situ by dc heating treatment of wafers with $1-10\,\Omega$ cm n-type doping. The cleaning procedure of the sample includes preheating (700 °C, 30 s), flashing (1250 °C, 5 s), post annealing (850 °C, 30 s) and monotonic cooling to room temperature taking 30 s. It was repeated till getting clear Si(111)-7 × 7 RHEED pattern with high quality as displayed in Fig. 4.4a. Tl/Si(111) reconstructions were prepared by depositing Tl from an alumina effusion cell with tungsten filament for dc current heating onto Si(111)-7 × 7 surface. Since oxidation progresses in the atmosphere, Tl is immersed in oil at the time of preservation, taken out just before use, washed with isopropyl alcohol and then introduced into the vacuum chamber. Because Tl does not sublime, it can be degassed by keeping it at the melting point for a long time in the vacuum chamber.

The 1×1 -Tl reconstruction was prepared by depositing 1 ML Tl onto clean Si surface held at $\sim 300 \,^{\circ}$ C [1 ML (monolayer) = $7.8 \times 10^{14} \,^{\circ}$ cm⁻²]. One can see the characteristic Kikuchi line extends from the (00) spot as in Fig. 4.4b. To obtain 6×6 -Tl with good reproducibility, Tl is additionally vapor-deposited on Si(111)-1 \times 1-Tl after it is cooled to 200 °C or lower. Then, 1 ML of Tl changes the diffraction pattern into Fig. 4.4c. Intensity of 1×1 , especially (10), (01) spot intensities are weakened, and weak diffraction spots appeared near the (00) spot (pointed by arrows in Fig. 4.4c). The decrease in the intensity of 1×1 means that the surface was covered by the slightly misoriented double layer. Weak diffraction spots near the (00) spot can be interpreted as deriving from the 6×6 period of the moiré pattern. If the additional dosing of Tl is carried out for 1 ML or more, the RHEED pattern rapidly changes from Fig. 4.4c, d, in which the 6×6 spots disappear and conversely the (10), (01) spot intensity recovers. This change corresponds to agglomeration and destruction of the double layer structure and exposure of the first wetting layer. The spots pointed by the arrows in Fig. 4.4d indicate the existence of a crystal having a lattice constant smaller than 1×1 , which is thought to originate from the Tl islands. These observation is agree with the STM studies in Sect. 4.2. Therefore, repeating RHEED observation with deposition of Tl at a constant rate makes it possible to

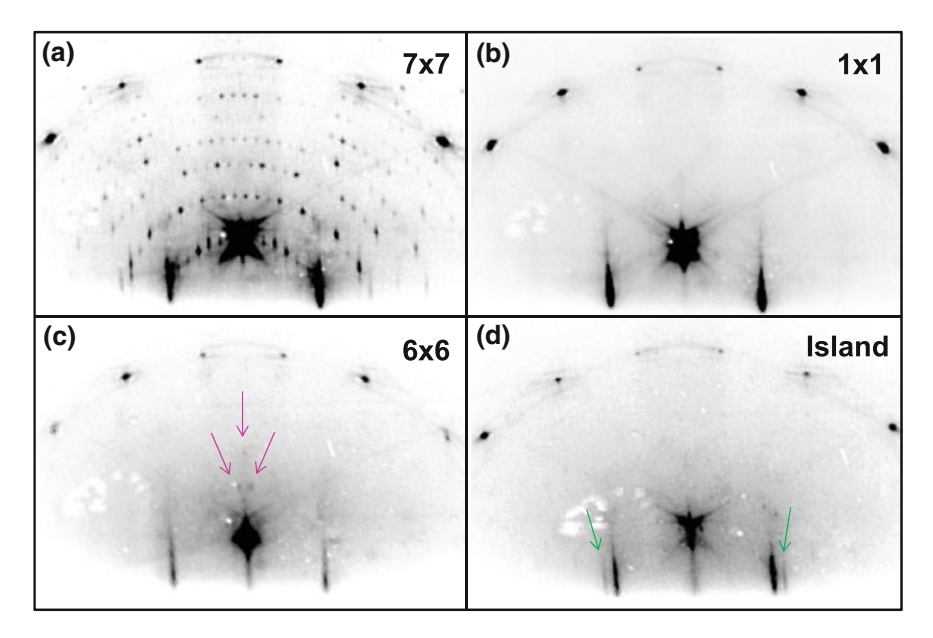


Fig. 4.4 Evolution of RHEED patterns during Tl adsortion on a Si (111) surface. **a** Si(111)-7 \times 7. **b** 1 \times 1-Tl. **c** 6 \times 6-Tl. Pink arrows indicates the 1/6 order reflections. **d** Tl-overdosed surface (> 2ML), where 1 \times 1-Tl and 3D islands coexist. The spots pointed by green arrows are derived from the islands

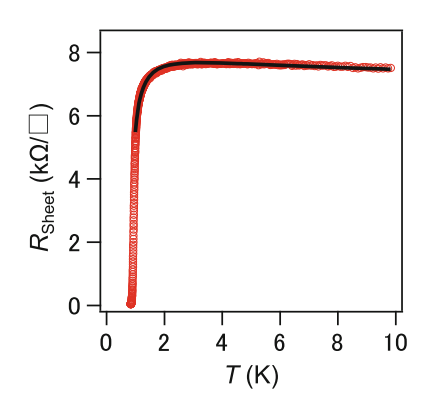
calibrate the deposition amount by considering 1 ML for the time when 1×1 is formed and 2 ML for the time when the island is formed.

4.4.2 Results

Figure 4.5 shows the temperature dependent sheet resistivities $R_{\rm sheet}(T)$ of the 6 × 6-Tl. on the surface with the 6 × 6-Tl, $R_{\rm sheet}$ kept ca. 7.6 k Ω , well below the quantized resistance for electrons, $h/e^2=25.8$ k Ω . This indicates the metallic nature of the Tl double layer. One can see the most significant feature of this system, a superconducting transition below 1 K. The midpoint of resistance drop gives $T_{\rm c}\sim0.96$ K. According to BCS theory, we can convert $T_{\rm c}\sim0.96$ K to superconducting gap $\Delta(0)$ and Pippard's coherence length ξ_0 via Eq. (2.132) $\Delta(0)=ak_BT_{\rm c}(a=1.76-2.2)$ and $\xi_0=\frac{\hbar v_{\rm F}}{\pi\Delta(0)}$. Using $v_{\rm F}$ (Fermi velocity) taken from ARPES measurements in Sect. 4.2, $\Delta(0)$ and ξ_0 can be estimated as 0.15–0.19 meV and 1500–1900 nm, respectively. Also, using the R_n and k_F , the mean free path is estimated by Eq. (2.13)

$$l = \frac{1}{k_F} \cdot \frac{h/e^2}{R_n}. (4.2)$$

Fig. 4.5 Sheet resistivity of double-layer 6×6 -Tl surface as a function of temperature [25]. The resisitivity starts to decrease at around 4 K, and reaches zero around 1 K. The black solid line shows a result of the least-squares fit to conductivity including Aslamazov-Larkin term and $\ln T$ components



The result is l=2.4 Å, which is about the same as the Fermi wave number. It is close to the limit at which Bloch picture can be applied. At the same time, this is much shorter than $\xi_0=1500-1900$ nm, meaning that the present system can be regarded as a dirty superconductor. Effective coherence length ξ in a dirty limit superconductor is estimated as $\xi=0.85\sqrt{\xi_0 l}=16$ (nm).

Although the resistivity slightly uprises towards low temperature higher than 4 K, it decrease gradually below 4 K, which can be interpreted as an effect of amplitude fluctuations of the superconducting order parameter, and suggests strong two-dimensional nature of the present superconducting system. In Sect. 2.4.2, it is described that the amplitude fluctuation effect is explained by Eq. (2.139). Since this case is a dirty superconductor, the MT term does not work. The following equations well reproduce this behavior as proved by the coincidence of the experimental data with the numerical fitting curve shown by the black solid line in Fig. 4.5b.

$$R = \frac{1}{\sigma_0 + \sigma_{AL} + \sigma'},\tag{4.3}$$

$$\sigma_{\rm AL} = \frac{e^2}{16\hbar} \cdot \frac{T_c}{T - T_c},\tag{4.4}$$

$$\sigma' = \alpha \frac{e^2}{h} \ln T. \tag{4.5}$$

The last term σ' includes all possible components giving $\ln T$ behavior: weak (anti) localization and electron-electron interaction in the diffusion channel. From the fitting, $T_{\rm c}=0.804\pm0.001~{\rm K}$ and $\alpha=0.170\pm0.003$ are obtained, which roughly agree with the $T_{\rm c}\sim0.96~{\rm K}$ defined by the midpoint.

Magnetic-field-induced superconductor-insulator transition

Figures 4.6a and b show the sheet resistivities of 6×6 -Tl as a function of temperature measured at different values of perpendicular magnetic field. Figure 4.6a presents the high-resistance region of 7.0–8.8 k Ω . Except for 1.00 T, each curve has onset of superconductivity where the sign of dR/dT changes from negative to positive

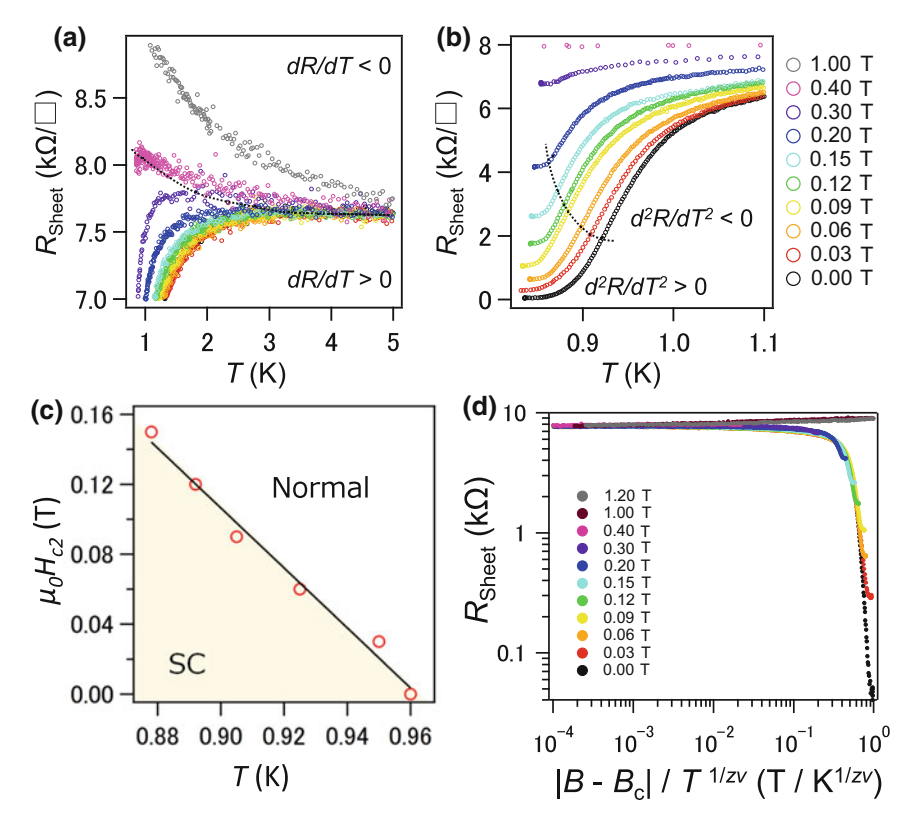


Fig. 4.6 a, **b** Sheet resistivities under different magnetic fields applied perpendicular to the surface [25]. **a** Temperature dependencies in the high-resistance region $(7.0-8.8 \text{ k}\Omega)$. A black dotted line indicates the boundary where the sign of dR/dT changes, namely, superconductor-insulator transition occurs. **b** Same in the low-resistance region $(0-8 \text{ k}\Omega)$. Black dotted line indicates the boundary where the sign of d^2R/dT^2 changes. **c** Estimation of the upper critical field based on the GL picture. The red circles indicate the critical points $(T, \mu_0 H_{c2})$ where the sheet resistivities cross the midpoint value. The black solid line is given by the numerical fitting using GL theory Eq. [(2.121)]. **d** Result of usual scaling analysis of SIT: All data of the sheet resistance shown in a, b are summarized as a function of the scaling variable $|B - B_c|/T^{1/zv}$

(denoted by the black dotted line in Fig. 4.6a). The relation between the magnetic field and the temperature at the critical points $[B_{c2} = \mu_0 H_{c2}(T)]$, where the resistances become half of those in normal state (= 3.8 k Ω), is plotted linearly as shown in Fig. 4.6. By applying the equation of the GL theory (2.121)

$$\mu_0 H_{c2}(T) = \frac{\phi_0}{2\pi \xi_{GL}(0)^2} \left(1 - \frac{T}{T_c} \right),\tag{4.6}$$

 $T_{\rm c}=0.962\pm0.003$ K, and $\xi_{\rm GL}(0)=14.1\pm0.4$ nm are obtained. This is consistent to the effective coherence rength $\xi=16\,\mathrm{nm}$. The upper critical magnetic field at

absolute zero degree is obtained by extrapolation as $\mu_0 H_{c2}(0) = 1.65 \pm 0.09$ T. Raising of the magnetic field decreases the onsets and eventually, at the fields larger than 0.4 T, resistivity rises monotonically with cooling. In other words, it shows insulating behavior down to the lowest temperature. This suggests the occurrence of magnetic-field-induced superconductor-insulator transition (B-SIT). These data enable a scaling analysis in terms of the quantum phase transition and the quantum critical behaviour, as mentioned in Sect. 2.4.2. In the B-SIT, magnetic field B is used as control parameter. Then $R_{\rm sheet}(B,T)$ is plotted with respect to the scaling variable $|B-B_c|/T^{z\nu}$, and adjust the power $z\nu$ to obtain the best visual coincidence of the data [27]. Figure 4.6d shows the splitting of $R_{\rm sheet}(B,T)$ into two branches. This successful scaling is obtained assuming $z\nu=0.2$. The value $z\nu=0.2$ deviates from typical examples: $z\nu=4/3$ (classical percolation model) or 2/3 (3D XY model). This point will be discussed later.

BKT transition

According to the BKT theory, the two-dimensional superconductor is exposed to the incessant creation/annihilation of vortex-antivortex pairs due to the phase fluctuation effect. Above the BKT transition temperature $T_{\rm BKT}$, the pairs are unbound and cause the resistivity. The zero resistance state is realized by the binding of vortex-antivortex pairs. This results in the "tailed" resistance curve slightly below the $T_{\rm c}$. To determine the BKT transition temperature, we used the Halperin-Nelson equation (2.141) [28],

$$R \propto \exp\left[-2b\left(\frac{T_c - T_{\text{BKT}}}{T - T_{\text{BKT}}}\right)^{1/2}\right],$$
 (4.7)

where b is material dependent parameter. The successful least-square fitting shown by the black dashed line in Fig. 4.7a suggests strong two-dimensionality of the present system and gives a superconducting and BKT transition temperatures $T_c = 1.0 \pm 0.3$ K and $T_{\rm BKT} = 0.8 \pm 0.4$ K, respectively. The critical temperatures obtained from the fitting to Eqs. (4.3) and (2.141) are consistent with the T_c of 0.96 K, estimated from the midpoint of resistance curve. At dirty limit, BKT transition temperature can also be estimated by Eq. (2.141) [29]

$$\frac{T_{\rm BKT}}{T_{\rm c}} \sim \frac{1}{1 + 0.17 \frac{R_n}{R}}.$$
 (4.8)

 $T_{\rm BKT} = 0.73$ K obtained from this equation is in a good agreement with $T_{\rm BKT} = 0.8 \pm 0.4$ K estimated from the Halperin-Nelson fitting above. This confirms that the present system shows the BKT transition as a dirty-limit superconductor.

Intermediate metallic state

Furthermore, another phase transition is found under finite magnetic field. As one can see in Fig. 4.6b, which focuses on the region below 8 k Ω , resistances drop gradually with cooling. This can be interpreted as the amplitude fluctuation, which

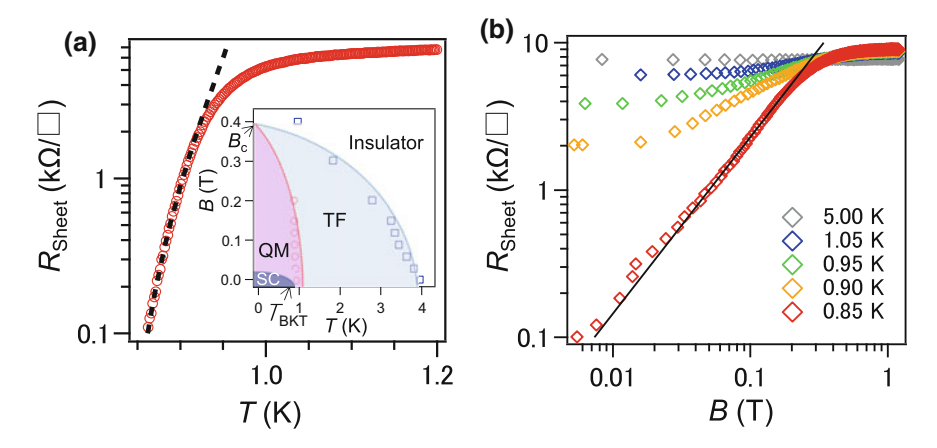


Fig. 4.7 a Resistive transition plotted in a semilogarithmic scale [25]. The black dashed line represents the Berezinskii-Kosterlitz-Thouless transition using the Halperin-Nelson equation Eq. (2.141). b Magnetoresistance for different temperatures [25]. The curve obtained at 0.85 K is empirically fitted by the scaling function of superconductor-Bose metal transition (black solid line). Inset in a shows full B-T phase diagram of the Tl double layer. The blue squares denotes the phase boundary of superconductor-insulator transition, where the sign of dR/dT changes (the black dotted line in Fig. 4.6a). The red circles, dividing the quantum metal (QM) state from a state dominated by strong thermal fluctuation (TF) of order parameter, mark the transition where d^2R/dT^2 changes their sign (the black dotted line in Fig. 4.6b)

affects superconducting properties even in the magnetic field [27]. In this region, $d^2R/dT^2 < 0$, that is, the resistance drop is accelerated as lowering the temperature. Once across the boundary denoted by the black dotted line in Fig. 4.6b, however, d^2R/dT^2 becomes positive, i.e., R-T curves are leveled toward the lowest temperature with finite residual resistivities. These plateau suggest a kind of an intermediate "metallic state", which is not insulating but has finite resistivity. For understanding this non-trivial temperature dependence under finite magnetic field, we performed numerical fittings with theoretical models describing dissipative vortices motion in the R(T, B) behaviors. In usual cases of broaden superconducting transitions due to magnetic field, vortices should be driven by thermal activation (thermally activated flux flow, TAFF), causing the dissipation written as $R \propto \exp\left(\frac{-U(B)}{k_BT}\right)$, where U(B)is the activation energy. Even though TAFF is widely observed in 2DSC, in 6×6 -T1, however, broadening of transition due to magnetic field is not significant. Also, it does not explain the leveling of resistance. A possible picture of the intermediate metallic state between the SIT is the Bose metal (BM) [30–35]. In the model, a 2D system of interacting bosons may form a gapless, nonsuperfluid state in the limit of zero temperature. It is argued that the uncondensed Cooper pairs and vortices cause the small resistance even under small finite field. A magnetic field is responsible for gauge fluctuations, which disrupt phase coherence and cause dissipation.

The induced resistance which is proportional to the free (anti) vortices density n_v as $R \propto R_Q n_v \mu_v$. Here, μ_v is vortex mobility. n_v scales as $n_v \sim 1/\xi_+^2$. ξ_+ is superfluidicity correlation length which diverges across the boundary of superconductor-BM transition with an exponent ν_0 , i.e. $\xi_+ \sim (B-B_{\rm c0})^{-\nu_0}$ where $B_{\rm c0}$ is the critical field of the superconductor to BM state. As a result, resistivity across the field-tuned transition from superconductor to metallic state is described by [31]

$$R \propto (B - B_{c0})^{2\nu_0}$$
. (4.9)

Fig. 4.7c shows a log-log plot of sheet resistivities versus magnetic field taken at several different temperatures. The curve at 0.85 K obeys a power-law dependence on the magnetic field. We have fitted the data to Eq. (4.9). In Fig. 4.5c, solid black line represents the fitting result, which shows good agreement with the data at T=0.85 K. This yields the critical exponent of $\nu_0=0.60$. In other experimental examples employing this analysis, $\nu_0\sim0.5$ [34] and $\nu_0=1.61$ [35] were reported in the MoGe thin film and exfoliated NbSe₂ thin flake, respectively. The numerical fitting also gives us the critical field of $B_{c0}\sim0$ T, indicating that the system is in the metallic phase at 0.85 K even without magnetic field. This is reasonable since, under zero magnetic field, a zero-resistivity state survives only below 0.8 K due to vortex-antivortex generation as discussed above.

4.4.3 Discussion

 $T_{\rm c} = 0.96$ K is lower than the predicted critical temperature $T_{\rm c} = 7.9-8.9$ K by the electron-phonon interaction constant λ estimated from ARPES and the Debye temperature of bulk Tl. There are two possible reasons for this. First, the Debye temperature of 6×6 -Tl surface may be lower than that of bulk Tl. It is known that the Debye temperature of the metal surface decreases by about 0.75 times compared with the Debye temperature in the bulk [36, 37]. There are a few studies on the metal adsorbed semiconductor surface [38, 39], $\Theta_D = 90$ K is reported in the Ge (111) $\sqrt{3} \times \sqrt{3}$ -Ag structure, which is much lower than 225 K in the bulk Ag [40]. Qualitatively, the Debye temperature is as low as the atoms constituting the crystal are heavy or bonding between the atoms is weak. Actually Tl is a heavy atom, and the interlayer coupling in the Tl bilayer system is weak. These material properties may suppress the Debye temperature. The other reason is derived from the morphology of the system. As seen in Fig. 4.2b, the superconducting double layer of Tl has not only atomic defects or steps, but also spatial fluctuations of coverage. The bare 1×1 single Tl layer area is an insulator that should act as the Josephson junction between areas of the superconducting 6×6 -Tl double layer. Such disorders are called "quenched disorder". Although the quenched disorder can suppress the T_c immediately, it is recently pointed to cause the "quantum Griffiths singularity". In some of the epitaxial two-dimensional systems accompanying with superconductor-insulator (or -metal)

transition, temperature-dependent zv have been reported [41, 42]. In these studies, zv grows rapidly with decreasing temperature and tends to diverge with the field approaching a critical value. This divergence is regarded as a sign of the quantum Griffiths singularity, in which the dynamical exponent z obeys activated scaling behavior. Then the system is under the domination of the quenched disorder, namely, time-independent random potentials such as vacancies, defects and impurity atoms. The temperature dependence originates from the interplay of the quenched disorder and the thermal/quantum fluctuations. The present superconducting double layer of Tl satisfies the condition where the quantum Griffiths singularity occurs. However, it is hidden by strong thermal fluctuations because at the temperature range where the scaling equation (2.145) is applied, thermal fluctuations are dominant as seen in Fig. 4.6b. Thus, this region possibly corresponds to the high-temperature phase of quench-disordered system. Despite the presence of disorder, the high-temperature phase should be regarded as a clean system, in which ν is determined by the Harris criterion. The Harris criterion suppresses ν as $d\nu < 2$, where d is dimension, leading to small value of $z\nu$, for example, 0.32 in Ref. [41]. For the lower temperatures, vortex glass state is expected to be induced by magnetic field due to a quenched disorder. In the vortex glass phase, variable range of hopping (VRH) of vortices generates finite resistance: $R \propto \exp[-(T_0/T)^{1/3}]$ [43, 44]. R-T curves of the 6 × 6-Tl under magnetic field are not agree with this relation due to saturation of resistance at very low temperatures. Hence, as described above, Bose metal is the most plausible picture to create an intermediate metallic state in the 6×6 -Tl double layer.

A phase diagram of the 6×6 -Tl is presented in the inset of Fig. 4.7a. The phase transition at high temperature and field is described by usual scaling analysis of SIT. Its boundary is determined by the black dotted line in Fig. 4.6a and shown as squares with guideline in the diagram. However, the present system does not have direct transition into the pure superconducting state. First, Cooper pair formation is governed by the thermal fluctuation (TM), which drives the gradual decreasing of resistivity. The resistivity is dragged into mean-field superconductivity state but global phase coherence is suppressed by gauge fluctuations. The state in which bosonic Cooper pairs are spatially confined by the localization length of randomly induced strong phase fluctuations is regarded as quantum metallic state (QM). The boundary shown as circles with guideline in the diagram corresponds to the black dotted line in Fig. 4.6b. In the QM phase, dissipation of unbinded vortex-antivortex pairs causes finite resistivity that survives even at zero-magnetic field. True superconductivity, i.e. zero resistance state is achieved by binding of the vortex-antivortex pairs at $T_{\rm BKT}$ in accordance with the BKT physics. It should be noted that Dalidovich and Phillips pointed out that Bose metal state is a "phase glass" where superconductor loses global phase coherence [32, 33]. Though vortex and phase glasses are not identical, there remains room for discussion about correlation of these two states.

4.5 Summary

Thallium deposition on the Si(111)-1 × 1-Tl surface at ambient temperature results in the formation of 6×6 -Tl double-layer film which has a metallic character in contrast to the single-layer 1×1 -Tl insulating surface. The 6×6 -Tl double layer exhibits superconducting transition at 0.96 K. The transition is broaden by amplitude and phase fluctuations of order parameter, which are described by Aslamazov-Larkin and Halperin-Nelson formulas, respectively. Applying perpendicular magnetic field induced superconductor-insulator transition. In the high-temperature regime, the data agree with the usual scaling law of SIT, but obtained small value of $z\nu = 0.2$ implies that the present system is in the high-temperature phase of quench-disordered 2DSC. At the lower-temperature regime, on the other hand, an intermediate metallic state is observed. Magnetoresistance measurements close to the lowest temperature suggests that the intervening state is the Bose metal, induced by gauge fluctuations by magnetic field. This is an extension of phase fluctuation effect without magnetic field, in other words, the BKT physics.

References

- 1. V.G. Kotlyar, A.A. Saranin, A.V. Zotov, T.V. Kasyanova, Surf. Sci. 543, L663 (2003)
- 2. S. Özkaya, M. Çakmak, B. Alkan, Surf. Sci. 602(7), 1376 (2008)
- 3. S. Özkaya, M. Cakmak, B. Alkan, Phys. Stat. Sol. B 251(8), 1570 (2014)
- L. Vitali, F.P. Leisenberger, M.G. Ramsey, F.P. Netzer, J. Vac. Sci. Technol. A 17(4), 1676 (1999)
- 5. P. Kocán, P. Sobotík, I. Ošť ádal, Phys. Rev. B 84(23), 233304 (2011)
- S.S. Lee, H.J. Song, N.D. Kim, J.W. Chung, K. Kong, D. Ahn, H. Yi, B.D. Yu, H. Tochihara, Phys. Rev. B 66(23), 233312 (2002)
- 7. T. Noda, S. Mizuno, J. Chung, H. Tochihara, Jpn. J. Appl. Phys. 42(3B), L319 (2003)
- N.D. Kim, C.G. Hwang, J.W. Chung, T.C. Kim, H.J. Kim, D.Y. Noh, Phys. Rev. B 69(19), 195311 (2004)
- 9. K. Sakamoto, T. Oda, A. Kimura, K. Miyamoto, M. Tsujikawa, A. Imai, N. Ueno, H. Namatame, M. Taniguchi, P.E.J. Eriksson, R.I.G. Uhrberg, Phys. Rev. Lett. **102**(9), 096805 (2009)
- 10. J. Ibañez-Azpiroz, A. Eiguren, A. Bergara, Phys. Rev. B 84(12), 125435 (2011)
- 11. K. Sakamoto, T.H. Kim, T. Kuzumaki, B. Müller, Y. Yamamoto, M. Ohtaka, J.R. Osiecki, K. Miyamoto, Y. Takeici, A. Harasawa, S.D. Stolwijk et al., Nat. Commun. 4, 2073 (2013)
- S.D. Stolwijk, A.B. Schmidt, M. Donath, K. Sakamoto, P. Krüger, Phys. Rev. Lett. 111(17), 176402 (2013)
- S.D. Stolwijk, K. Sakamoto, A.B. Schmidt, P. Krüger, M. Donath, Phys. Rev. B 90(16), 161109 (2014)
- 14. K. Nakajin, S. Murakami, Phys. Rev. B **91**(24), 245428 (2015)
- S.D. Stolwijk, K. Sakamoto, A.B. Schmidt, P. Krüger, M. Donath, Phys. Rev. B 91(24), 245420 (2015)
- 16. L. Vitali, M.G. Ramsey, F.P. Netzer, Surf. Sci. 452(1/3), L281 (2000)
- 17. A.A. Saranin, Priv. Commun.
- 18. S. Hatta, T. Noma, H. Okuyama, T. Aruga, Phys. Rev. B 90, 245407 (2014)
- 19. C. Kittel, Introduction to Solid State Physics (Wiley, Hoboken, 2005)
- 20. S.H. Uhm, H.W. Yeom, Phys. Rev. B 86, 245408 (2012)

References 77

 M. Ligges, M. Sandhofer, I. Sklyadneva, R. Heid, K.P. Bohnen, S. Freutel, L. Rettig, P. Zhou, P.M. Echenique, E.V. Chulkov, U. Bovensiepen, J. Phys. Condens. Matter 26(35), 352001 (2014)

- T. Zhang, P. Cheng, W.J. Li, Y.J. Sun, G. Wang, X.G. Zhu, K. He, L. Wang, X. Ma, X. Chen et al., Nat. Phys. 6, 104 (2010)
- 23. T. Uchihashi, P. Mishra, M. Aono, T. Nakayama, Phys. Rev. Lett. 107, 207001 (2011)
- 24. M. Yamada, T. Hirahara, S. Hasegawa, Phys. Rev. Lett. 110, 237001 (2013)
- S. Ichinokura, L. Bondarenko, A. Tupchaya, D. Gruznev, A. Zotov, A. Saranin, S. Hasegawa, 2D Mater. 4(2), 025020 (2017)
- M. Yamada, T. Hirahara, R. Hobara, S. Hasegawa, H. Mizuno, Y. Miyatake, T. Nagamura, e-J. Surf. Sci. Nanotechnol. 10, 400 (2012)
- 27. V.F. Gantmakher, V.T. Dolgopolov, Phys. Uspekhi 53(1), 1 (2010)
- 28. B. Halperin, D.R. Nelson, J. Low Temp. Phys. **36**(5–6), 599 (1979)
- 29. K. Epstein, A. Goldman, A. Kadin, Phys. Rev. B 26, 3950 (1982)
- 30. D. Das, S. Doniach, Phys. Rev. B 60(2), 1261 (1999)
- 31. D. Das, S. Doniach, Phys. Rev. B **64**(13), 134511 (2001)
- 32. D. Dalidovich, P. Phillips, Phys. Rev. Lett. 89(2), 027001 (2002)
- 33. P. Phillips, D. Dalidovich, Science **302**(5643), 243 (2003)
- 34. N. Mason, A. Kapitulnik, Phys. Rev. B **64**(6), 060504 (2001)
- 35. A. Tsen, B. Hunt, Y. Kim, Z. Yuan, S. Jia, R. Cava, J. Hone, P. Kim, C. Dean, A. Pasupathy, Nat. Phys. (2015)
- 36. J. Demuth, P. Marcus, D. Jepsen, Phys. Rev. B 11, 1460 (1975)
- 37. B. Clark, R. Herman, R. Wallis, Phys. Rev. 139, A860 (1965)
- 38. Y. Fukaya, A. Kawasuso, K. Hayashi, A. Ichimiya, Appl. Surf. Sci. 237, 29 (2004)
- 39. Y. Fukaya, A. Kawasuso, K. Hayashi, A. Ichimiya, Phys. Rev. B **70**, 245422 (2004)
- 40. Y. Fukaya, A. Kawasuso, A. Ichimiya, e-J. Surf. Sci. Nanotechnol. 3, 228 (2005)
- 41. Y. Xing, H.M. Zhang, H.L. Fu, H. Liu, Y. Sun, J.P. Peng, F. Wang, X. Lin, X.C. Ma, Q.K. Xue et al., Science **350**, 542 (2015)
- S. Shen, Y. Xing, P. Wang, H. Liu, H. Fu, Y. Zhang, L. He, X.C. Xie, X. Lin, J. Nie, J. Wang, Phys. Rev. B 94, 144517 (2016)
- 43. A. Auerbach, D.P. Arovas, S. Ghosh, Phys. Rev. B **74**(6), 064511 (2006)
- 44. G. Koren, Y. Mor, A. Auerbach, E. Polturak, Phys. Rev. B 76(13), 134516 (2007)
- 45. S. Lee, H. Song, N. Kim, J. Chung, K. Kong, D. Ahn, H. Yi, B. Yu, H. Tochihara, Phys. Rev. B 66, 233312 (2002)

Chapter 5 Thallium-Lead Monatomic-layer Compound

Abstract The Rashba effect, a momentum-dependent spin splitting of electrical bands is a dramatic phenomena originated from lack of the space inversion symmetry. When the Rashba effect meets superconductivity, novel superconducting phenomena is predicted to realize: mixing of singlet-triplet component, spatial modulation of order parameter by Fulde-Ferrell-Larkin-Ovchinnikov mechanism, transition to topological superconductivity etc. Although the surface two-dimensional electron system has been expected to combine these independent frameworks, there has been no report on coexistence of them so far. Here, a one-atom-layer compound made of one monolayer of Tl and one-third monolayer of Pb on a Si (111) surface, known as Rashba-metallic surface system is presented to exhibit two-dimensional superconducting transport properties. The observed transition temperature of 2.26 K is sizable, while the energy of Rashba spin splitting is still larger upto 250 meV, promising for the emergence of the exotic superconductivity.

Keywords Thallium · Lead · Silicon · Surface · Superconductivity · Rashba effect

5.1 Background

As mentioned in Sect. 2.4.4, in the supercondcutor without space inversion symmetry, emergence of abundant novel superconducting phenomena are predicted: a mixing of singlet-triplet components [1, 2], a spatial modulation of the order parameter by the Flude-Ferrell-Larkin-Ovchinnikov-like mechanism [3, 4], and enhancement of in-plane critical magnetic field [3–5]etc. These phenomena are driven by *the Rashba effect*, a spin splitting of band dispersion due to spin-orbit coupling. Many of semiconductor surface with adsorption of heavy elements such as Bi and Tl have been reported to have Rashba effect [6–10]. For applications to spintoronics, one needs metallic spin-split bands to ensure considerable spin transport whereas no metallic Rashba bands are found in surface systems above. As an exception, Yaji et al. reported that the Ge (111) - $\sqrt{3} \times \sqrt{3}$ -Pb structure has a metallic surface state with a relatively large Rashba split of 200 meV [11]. Hatta et al. confirmed that this one maintains metallic conduction down to 9 K by electrical conduction measurements

[12]. Although such heavy-metal-induced metallic surface states are expected to combine the Rashba effect and superconductivity, there has been no report on the coexistence of them so far. Gruznev and colleagues reported that metallic Rashba surfaces can be easily produced by adsorbing two metal species including heavy elements. On the surface of Si (111), $\sqrt{3} \times \sqrt{3}$ - (Bi, Na) [13], $\sqrt{3} \times \sqrt{3}$ - (Tl, Pb) [13], $\sqrt{3} \times \sqrt{3}$ - (Tl, Sn) [14] have been found as such examples. They can be regarded as "Monatomic-layer alloys", which have been unexplored in surface science compare to single-specie-adsorbed semiconductor surfaces. In particular, $\sqrt{3} \times \sqrt{3}$ - (Tl, Pb), in other words, *monolayer Tl-Pb alloy* has so large Fermi surface centered on Γ point and Rashba splitting of 250 meV at the maximum that is expected to have superconductivity related to the Rashba effect.

5.2 Structural Properties of Si(111) - $\sqrt{3}$ x $\sqrt{3}$ -(Tl, Pb)

5.2.1 Atomic Arrangement

The monolayer Tl-Pb compound is formed starting from Si (111) - 1 \times 1-Tl reconstruction. When lead is deposited onto the 1 \times 1-Tlsurface held at room temperature, the patches of the compound region are created and grow in size with Pb dosing til covering the entire surface at 1/3 ML Pb coverage (Fig. 5.1a and b) [15]. Here, 1 ML (monolayer) = 7.8×10^{14} cm⁻². In the large area STM images, the Tl-Pb compound is distinguished from the parent Tl monolayer by brighter contrast. The atomic arrangement appears in high-resolution image, which is kagome-like lattice with $\sqrt{3} \times \sqrt{3}$ periodicity (Fig. 5.1c). As confirmed by the DFT calculation in Ref. [13], the Tl-Pb alloy is composed of honeycomb-chained trimers of Tl atoms with Pb atoms occupying the T₄ sites in the center of each honeycomb unit (Fig. 5.1d). As shown in the cross section (Fig. 5.1d), Tl and Pb form a single atomic layer on Si (111), and the metal atoms are densely formed on the Si surface, so that the wave functions of each atom easily overlap each other, leading to a two-dimensional metallic state [13].

5.2.2 Electronic Structure

The band dispersion of the Tl-Pb alloy obtained by ARPES measurement by Gruznev et al. is shown in Fig. 5.2a. Four metallic band dispersions (Σ_1 , Σ_1' , Σ_2 , Σ_2') are observed. The DFT calculation incorporating spin-orbit interactions (Fig. 5.2b) revealed that these four bands are two pairs of spin-split bands by the Rashba effect. Consequently, its Fermi surface has a complicated spin texture as shown in Fig. 5.2c, where results of the DFT calculation (upper half) and ARPES measurement (lower half) are plotted together. In the Fermi-surface map, they appear as two split contours.

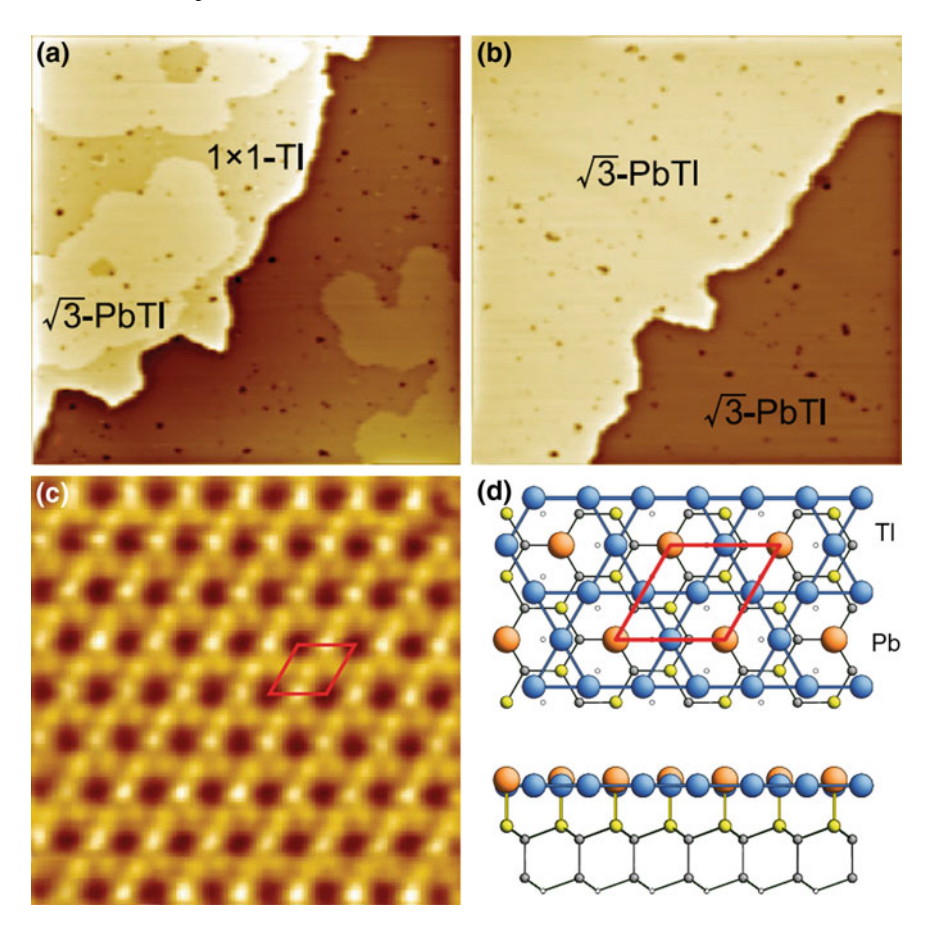


Fig. 5.1 Morphogical study of $\sqrt{3} \times \sqrt{3}$ - (Tl, Pb) by STM [15]. **a** Evolution of STM images in large-scale (150 \times 150 nm²), showing growth of the Tl-Pb 2D compound on the Si(111)1×1-Tl surface for RT deposition of **a** 0.18 ML Pb (intermediate stage) and **b** 0.33 ML Pb (final stage). Two atomic terraces are seen in each image. **c** High-resolution (5 \times 5 nm²) STM image of the (Tl, Pb)/Si(111) surface. **d** Atomic structure of the Tl-Pb compound. Tl atoms are shown by blue circles, Pb atoms by orange circles, top Si atoms by yellow circles, deeper Si atoms by light gray circles. The $\sqrt{3} \times \sqrt{3}$ unit cell is outlined by a red frame. Reprinted with permission from Ref. [15]

For the Σ_1 (Σ_1') band, the outer contour has almost round shape, while the inner contour is a hexagon with corners pointing in the $\overline{\Gamma}$ - \overline{K} directions in the $\sqrt{3}\times\sqrt{3}$ surface Brillouin zone (SBZ). The maximal momentum and energy splittings for the Σ_1 (Σ_1') band, $\Delta k_{\parallel}=0.038~\text{Å}^{-1}$ and $\Delta E_{\rm F}=250$ meV, respectively, are along the $\overline{\Gamma}$ - \overline{M} direction. The Σ_2 (Σ_2') bands show up as hexagonal contours with corners along the $\overline{\Gamma}$ - \overline{M} direction. The maximal splittings for the Σ_2 (Σ_2') band, $\Delta k_{\parallel}=0.050~\text{Å}^{-1}$ and $\Delta E_{\rm F}=140$ meV, are along $\overline{\Gamma}$ - \overline{K} direction. The DFT calculations revealed that the planar spin components show in-plane helicity with the spin being fully aligned in-plane and perpendicular to the momentum vector for momentum vectors along

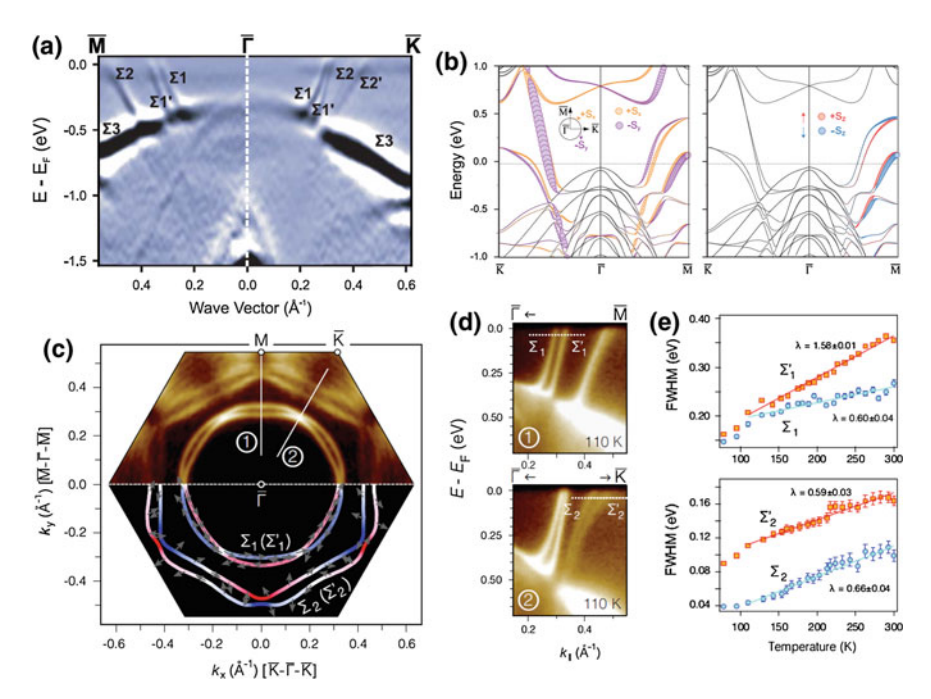


Fig. 5.2 Summary of spectroscopic studies on $\sqrt{3} \times \sqrt{3}$ - (Tl, Pb) [13, 15]. **a** Band dispersion by ARPES measurement [13]. **b** DFT calculation result including spin orbit interaction [13]. Left (right) panel shows in-plane (out-of-plane) spin polarization. The color of the plot corresponds to the component and direction of the spin, and the size represents the magnitude of spin polarization. **c** Fermi surface mapping of $\sqrt{3} \times \sqrt{3}$ - (Tl, Pb)[15] shown in the $\sqrt{3} \times \sqrt{3}$ surface Brillouin zone. The upper half is obtained by an ARPES measurement and the lower one is calculated by the DFT method. The gray arrows indicate the direction of the in-plane spin component, and the color code (from red to blue) represents the out-of-plane spin component. **d** Close-up band dispersions along (upper) $\overline{\Gamma}$ - \overline{M} and (lower) $\overline{\Gamma}$ - \overline{K} direction [shown as solid lines in a] at the vicinity of the Fermi plane [15]. **e** Temperature dependences of the spectral width in the energy direction of the dispersions Σ_1 , Σ_1' , Σ_2 , Σ_2' . The solid lines are linear fittings, which gradients give the electron-phonon interaction constant λ [15]. Reprinted with permission from Refs. [13, 15]

the $\overline{\Gamma}$ - \overline{K} directions. The out-of-plane spin component undulates between positive and negative values along the contours according to the $C_{3\nu}$ symmetry of the surface, as indicated by the color code in Fig. 5.2c.

As theoretically explained in Sect. 2.4.1 and performed in the previous chapter, we can evaluate the electron-phonon coupling constant λ as a benchmark for superconductivity. The λ can be obtained from a set of momentum distribution curves (MDC) in temperature-dependent ARPES measurements. λ was determined from a linear fit to the $\Delta E-T$ plots, where ΔE is the spectral energy width of a surface state band. Temperature range chosen was beyond 110 K in order to exceed the Debye temperature $\theta_{\rm D}$ which is known to amount 79–105 K for bulk Tl and Pb. For each band the measurements were conducted in the directions where spin splitting is maximal (i.e.,

perature of $\sqrt{3} \times \sqrt{3}$ (11,10)							
Dispersion	$k_F (\mathring{A}^{-1})$	λ	$v_F(10^8 \text{ cm/s})$	m^*/m_e	$n(10^{14} \text{ cm}^{-2})$	$T_{c}(\mathbf{K})\Theta_{D}^{\mathrm{Tl}}$	$T_{\rm c}({\rm K})\Theta_D^{\rm Pb}$
Σ_1	0.30	0.60	1.28	0.27	0.7	0.8-1.5	1.1-2.0
Σ_1'	0.33	1.58	1.27	0.30	0.9	6.7–7.8	8.9–10
Σ_2	0.42	0.66	0.27	1.77	1.5	1.2-2.0	1.5-2.6
Σ_2'	0.44	0.59	0.25	2.02	1.7	0.7–1.4	1.0–1.9

Table 5.1 ARPES-obtained electronical properties and expected superconducting transition temperature of $\sqrt{3} \times \sqrt{3}$ - (Tl. Pb)

along the $\overline{\varGamma}$ - \overline{M} direction for \varSigma_1 (\varSigma_1') band and along the $\overline{\varGamma}$ - \overline{K} for \varSigma_2 (\varSigma_2')) to obtain λ for each subband. Figure 5.2e shows ΔE -T plots with the results of EPC constant λ evaluation. This yield the following values of λ : 0.60 ± 0.04 for \varSigma_1 , 1.58 ± 0.01 for \varSigma_1' , 0.66 ± 0.04 for \varSigma_2 and 0.59 ± 0.03 for \varSigma_2' bands. One can see that EPC constant λ varies from one band to another and might be different even for two neighboring subbands having opposite spin orientations. Difference in the EPC of different bands in the same material is a usual phenomenon due to the largely varying electron DOS and phonon spectrum for different momentum values [16]. However, for the \varSigma_1 and \varSigma_1' , there is no big difference in wave numbers since they are pairs that originally spin degenerated. Such difference in λ of two bands split by Rashba effect were also observed in the ARPES measurements in Ge (111) - $\sqrt{3} \times \sqrt{3}$ - Pb [12]. It is explained that this is the final state effect in photoelectron spectroscopy, and it is considered to be the same in $\sqrt{3} \times \sqrt{3}$ - (Tl, Pb).

Fermi wave number k_F , Fermi velocity v_F , effective mass m^* , carrier density n are also estimated from the measurement results of each band dispersion. Furthermore, the superconducting transition temperature was also estimated from McMillan's equation (2.130)

$$T_{c} = \frac{\hbar \omega_{D}}{1.45k_{B}} \exp\left(-\frac{1.04(1+\lambda)}{\lambda - \mu^{*}(1+0.62\lambda)}\right),\tag{5.1}$$

using the measured λ and the literature value of Debye temperature of bulk Tl ($\Theta_D^{\text{Tl}} = 79 \text{ K}$) and Pb ($\Theta_D^{\text{Tl}} = 105 \text{ K}$) [17]. The results are summarized in Table 5.1. There is a significant difference in the expected transition temperature depending on the value of λ .

5.3 Purpose of This Study

As mentioned above, the $\sqrt{3} \times \sqrt{3}$ - (Tl, Pb) structure is a monoatomic layer structure accompanied with metallic Rashba state with enhanced electron-phonon interaction. This is promising for exotic superconductivity due to the lack of space-inversion-symmetry [1–5]. However, it is not trivial that simple pairing occurs on anisotropic

Fermi surface of $\sqrt{3} \times \sqrt{3}$ -(Tl, Pb) in terms of spin and phonon interaction. This study aim to reveal its ground state and nature of many-body effect, especially the effect of strong electron -phonon coupling.

The following results and discussions are based on the content of a published article [15]: "Two-dimensional superconductor with giant Rashba effect: One-atomic-layer Tl-Pb compound on Si(111)" A. V. Matetskiy, S. Ichinokura, L.V. Bondarenko, A.Y. Tupchaya, D.V. Gruznev, A.V. Zotov, A.A. Saranin, R. Hobara, A. Takayama, and S. Hasegawa: Physical Review Letters **115**, 147003 (2015).

5.4 Electrical Transport Studies on Si(111)- $\sqrt{3}$ x $\sqrt{3}$ - (Tl, Pb)

5.4.1 Sample Preparation

Sample preparation is done in the same way as in the previous chapter; MBE growth was done in the preparation chamber which is connected to the UHV-4PP system via a vacuum tunnel [18]. Si wafers (1–10 Ω cm, n-type doping) were used for substrates. They were cleaned by cycles of usual flash annealing procedure in situ by dc Jule heating: (i) preheating (700°C, 30 s), (ii) flashing (1250°C, 5 s), (iii) post annealing (850°C, 30 s) and (iv) monotonic cooling to room temperature taking 30 s. Self assemble of Tl and Pb on the surface is introduced by vaper deposition of the metals from a crucible made of alumina heated by a filament wound around for dc current. Both of the crucibles degassed enough in the vacuum chamber before use. Tl source needs particularly careful treatment to avoid oxidization and dissolution to water before installing to the vacuum chamber. First, Si(111)-1×1-Tl reconstruction was prepared by depositing 1 ML Tl onto Si(111)-7×7 clean surface held at \sim 300°C. Its RHEED pattern is shown in Fig. 5.3a. Subsequently, 1/3 ML of Pb was deposited on 1×1-Tl at room temperature. For the calibration of coverage of Pb, the structural transition from HIC- to SIC-phase of Pb/Si(111) at 4/3 ML [19] is observed prior

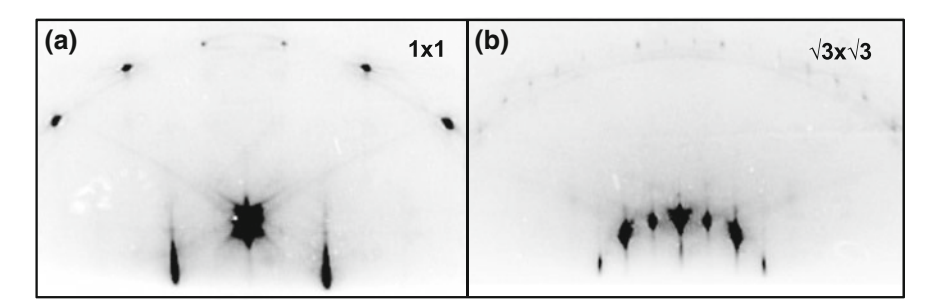


Fig. 5.3 RHEED patterns **a** before and **b** after deposition of 1/3 ML of Pb onto a 1 × 1-Tlsurface. The initial 1×1 - Tl surface is seen in **a**, while the completed $\sqrt{3} \times \sqrt{3}$ - (Tl, Pb) surface is shown in **b**

to the fabrication of $\sqrt{3} \times \sqrt{3}$ - (Tl, Pb). The sample for the electrical conductivity measurement showed a RHEED pattern like the Fig. 5.3b. A somewhat streaky but bright $\sqrt{3} \times \sqrt{3}$ spot was seen, which confirmed the formation of high quality structure throughout the surface.

5.4.2 Results

The $R_{\text{sheet}}(T)$ property on this $\sqrt{3} \times \sqrt{3}$ - (Tl, Pb) system at low temperature is displayed in Fig. 5.4. One can see that it reaches zero resistance state around 2.2 K, an evidence of superconductivity. The resistance starts to decrease from above T_{c} , which is due to the amplitude fluctuation effect [20, 21]. Accurate fitting of the experimental data with the theory Eq. (2.139) [20, 21]

$$\rho = \frac{1}{\sigma_0 + \sigma_{AL} + \sigma_{MT}} \tag{5.2}$$

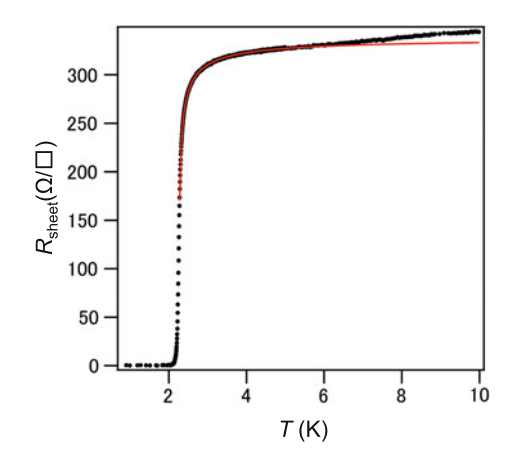
$$\sigma_{\rm AL} = \frac{e^2}{16\hbar} \cdot \frac{T_c}{T - T_c} \tag{5.3}$$

$$\sigma_{\rm MT} = \frac{e^2}{8\hbar} \cdot \frac{T_c}{T - (1+\delta)T_c} \ln \frac{T - T_c}{\delta T_c}$$
(5.4)

yields the $T_c=2.2568\pm0.0002$ K and also the "pair-breaking parameter" $\delta=0.0409\pm0.0002$.

By estimating the size of the superconducting gap from the observed T_c by Eq. (2.132) $\Delta(0) = ak_BT_c(a = 1.76-2.2)$, we obtain $\Delta(0) = 0.34-0.42$ meV, so that $\Delta E_R \gg \Delta(0)$. Namely, the energy of the spin splitting due to the spin orbit interaction is sufficiently larger than the superconducting gap, even though the gap

Fig. 5.4 Temperature dependence of the sheet resistance $R_{\text{sheet}}(T)$, exhibiting the superconducting transition at around 2.2 K. The red line is a result of the least-squares fit consisting the Aslamazov-Larkin-Maki-Thompson correction (Eq. 2.139)



itself is sizable value. This combination provides an opportunity to observe a number of fascination phenomena arising from lack of space inversion symmetry.

The Pippard's coherence length is estimated as $\xi_0 = 620$ –780 nm by the Eq. (2.122) $\xi_0 = \frac{\hbar v_F}{\pi \Delta(0)}$ using the superconducting gap and the inclination of the band dispersions in ARPES. In order to obtain the mean free path l precisely, it is necessary to numerically calculate it from the Eq. (2.8) in consideration of the wave number dependence. Here, let us approximate two sets of spin split bands into two sets of spin degenerate free electron bands with Fermi wave numbers of k_{F1} , $k_{F2} = 0.32$, 0.43Å^{-1} for rough estimation of l. Then, Eq. (2.13) is rewritten as

$$l = \frac{1}{k_{F1} + k_{F2}} \cdot \frac{h/e^2}{R_s},\tag{5.5}$$

resulting in l=10 nm, which is much smaller than Pippard's coherence length $(\xi_0 \gg l)$. Assuming a dirty limit expression Eq. (2.124), the effective coherence length is calculated as $\xi=67-75$ nm.

Upper critical field

Figure 5.5a shows the sheet resistance as a function of temperature under different magnetic field B applied perpendicular to the surface. The superconductivity transition becomes broader and shifts to lower temperature as the B increases. The results of the magnetoresistance measurements at different temperatures are summarized in Fig. 5.5b. The temperature–dependent upper critical field is extracted from these data by defining the upper critical field ($H_{c2} = B_{c2}/\mu_0$) at which the sheet resistance is a half of the normal-state-resistance. In Fig. 5.6, the points $\mu_0 H_{c2}(T)$ obtained from Fig. 5.5a/b are plotted as red circles/blue square, respectively. It can be seen that the

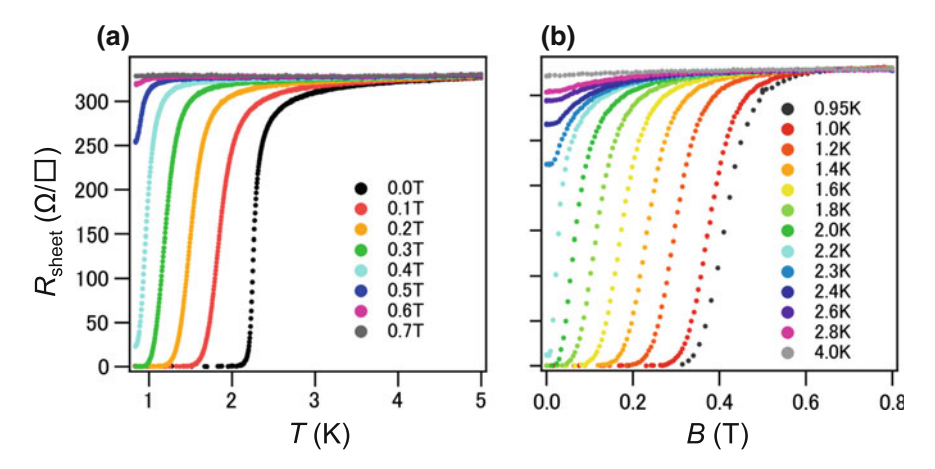
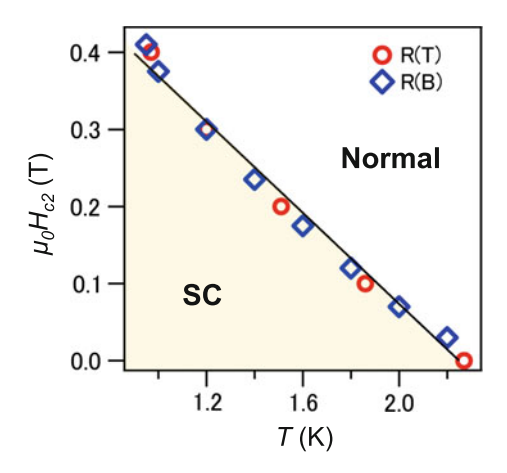


Fig. 5.5 Sheet resistivity as a function of temperature and out-of-plane magnetic field $R_{\rm sheet}(T,B)$. a Temperature dependence in steps of constant magnetic field and **b** magnetic field dependence at the temperature fixed at several values

Fig. 5.6 Temperature dependence of upper critical field of $\sqrt{3} \times \sqrt{3}$ - (Tl, Pb) obtained from Fig. 5.5. The points obtained from Fig. 5.5a **b** are plotted as red circles (blue squares). Solid line is fitting by GL theory (Eq. 2.121)



measurements were performed with high accuracy since both plots were on the same straight line. This linear relation can be evaluated in the framework of the GL theory. Numerical fitting to Eq. (2.121)

$$\mu_0 H_{c2}(T) = \frac{\phi_0}{2\pi \xi_{GL}(0)^2} \left(1 - \frac{T}{T_c} \right),\tag{5.6}$$

yields the coherence length as $\xi_{\rm GL}(0)=22.3\pm0.2$ nm, about twice the mean free path. Here $T_{\rm c}$ is fixed at 2.26 K. The $\xi_{\rm GL}(0)$ does not coincide with the effective coherence length ($\xi=67\text{--}75\,\mathrm{nm}$) obtained by assuming dirty limit equation Eq. (2.124), indicating that the present system is not at the dirty limit. The upper critical field at zero Kelvin is obtained by extrapolation as $\mu_0 H_{\rm c2}(0)=0.67\pm0.02\,\mathrm{T}$. These are on the same order as in the cases of mono/bilayer superconductors In and Pb on Si(111) [22].

BKT transition

Same as the 6 × 6-Tl, the $\sqrt{3}$ × $\sqrt{3}$ - (Tl, Pb) structure can be a test stage for BKT physics. Here, another sample were prepared for transport measurements. The temperature dependence of the sheet resistance is shown in Fig. 5.7a. The fitting result by the Eq. (2.139) is indicated by a red solid line in Fig. 5.7a, which reproduced a gradual decrease in resistance curve well. The transition temperature, which was used as a fitting parameter, was $T_c = 1.7919 \pm 0.0003$ K, and the pair-breaking parameter was $\delta = 0.122 \pm 0.001$. The sheet resistivity approaches zero with a "tail", caused by the motion of vortex-antivortex pairs, generated by phase fluctuations of the order parameter. The tail in the resistance drop can be explained by Halperin-Nelson equation Eq. (2.141) [23].

$$R \propto \exp\left[-2b\left(\frac{T_c - T_{\text{BKT}}}{T - T_{\text{BKT}}}\right)^{1/2}\right],\tag{5.7}$$

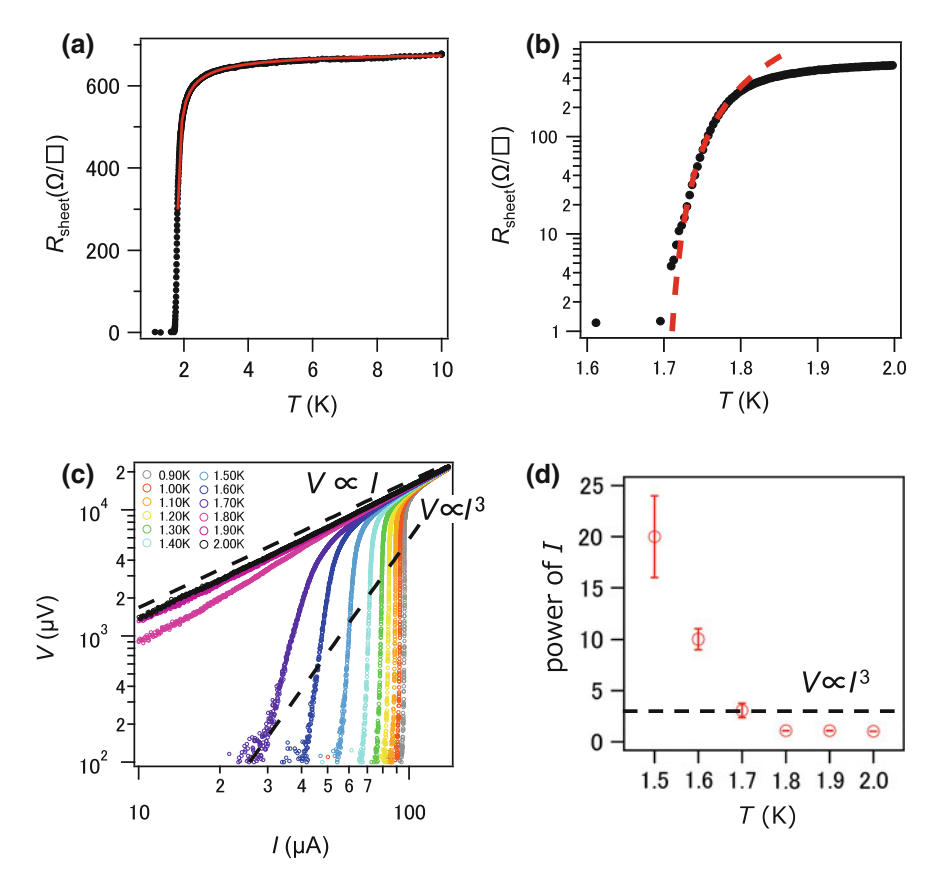


Fig. 5.7 a Summary of the electrical transport properties at the region of the BKT resistive transition without magnetic field. a Temperature dependence of the sheet resistivity in differently prepared sample, plotted in a linear and b semilog scale. The red solid and dashed lines in Fig. a and b are the results of least-squares fit to the Aslamazov-Larkin-Maki-Thompson correction (Eq. 2.139) and to the Halperin-Nelson equation (Eq. 2.141), respectively. c Current-voltage (I - V) characteristics at the different temperatures from 0.90 to 2.00 K plotted on a double logarithmic scale. The black dashed lines indicate $V \propto I$ and $V \propto I^3$ curves. d Fitting results obtained for the exponent a of the I - V curves $V \propto I^a$ at each temperature. The temperature at which $a \sim 3$ is ca. 1.70 K

The successful numerical fitting shown by the red solid line in Fig. 5.7b suggests strong two-dimensionality of the present system and gives a BKT transition temperature $T_{\rm BKT} = 1.714 \pm 0.002$ K by fixing $T_{\rm c}$ at 1.792 K.

Another signature supporting for the BKT transition can be found in the current-voltage (I-V) isotherms measured over a grid of different temperatures near $T_{\rm c}$. Figure 5.7c presents these data plotted in a double-logarithmic scale. Evolution of the isotherms is consistent with change in exponent of power in I-V curves around the critical current expected from the BKT mechanism when the temperature is varied near $T_{\rm c}$. The I-V dependence follows the $V\propto I$ law for the normal state

above T_c , while it becomes $V \propto I^3$ around T_{BKT} and shows abrupt transition to the superconducting state slightly below T_{BKT} . The extracted BKT transition temperature $T_{BKT} \sim 1.7$ K. The power of each I-V curve at $100 \, \mu \text{V}$ is obtained by fitting and plotted as a function of temperature, which is displayed in Fig. 5.7d. The exponent a of $V \propto I^a$ has changed from 1 to 3 around 1.7 K. This temperature is in agreement with the result from Halperin-Nelson fitting in Fig. 5.7b. Although the I-V curve at 1.7 K show $V \propto I^3$ around $100 \, \mu \text{V}$, behavior in the lower voltage is still unclear due to the limit of experimental accuracy at low bias. In the Hg - Xe thin film which is a typical report of BKT transition, the behavior of $V \propto I^3$ was seen from 1 to $100 \, \mu$ V. Even the present system is expected to show $V \propto I^3$ behavior if it is possible to measure lower voltage more accurately.

5.4.3 Discussion

First, let us compare the transition temperature with those in the Table 5.1, which are estimated from the electron-phonon interaction constant λ . The transition temperature obtained from the electrical transport measurement is lower than the temperature expected for the Σ_1' band and higher than those for the other surface bands. It is noted that estimation by λ is an ideal transition temperature, in other words, an upper limit value. In addition, it is generally known that the Debye temperature on the metal adsorption surface is lower than that of the corresponding bulk crystal as mentioned in previous chapter. Hence, the Σ_1' band with $\lambda=1.58$ is considered to be responsible for superconductivity. Since the estimation of the electron-phonon interaction constant by ARPES is influenced by the final state effect as described above, it is difficult to reach to quantitative agreement. However, as far as we consider the transition temperature, the superconductivity is driven by enhanced electron-phonon coupling. Σ_1' is one of a pair state forming inner Fermi surface pair shown in Fig. 5.2c, where the larger spin splitting occurs as $\Delta E_R = 250$ meV.

The second point that should be considered is the upper critical field. According to BCS theory, paramagnetic pair breaking field (Pauli limit) is estimated as $\mu_0 H_p = 1.86 T_c = 4.2$ T, which is much larger than the experimentally extrapolate $\mu_0 H_{c2}(0) = 0.67$ T. This indicates that orbital pair breaking determines the upper critical field in the present system with respect to the perpendicular magnetic field, as in usual two-dimensional superconductors.

In order to observe the suppression of paramagnetic effect arised from the lack of spatial inversion symmetry, it is effective to apply the in-plane magnetic field, which is a condition where orbital-pair destruction is prohibited. When the spatial inversion symmetry is broken, it is expected that the order parameter is spatially modulated with respect to the in-plane magnetic field. Such state is called stripe or helical phase [3, 4, 24] and enhance the in-plane critical magnetic field significantly. If a helical phase is formed in $\sqrt{3} \times \sqrt{3}$ - (Tl, Pb), the limit of upper critical field is expected to increase upto 200 T according to the theory by Dimitrova and Feigel 'man [4].

5.5 Summary

In this study, the 2D compound of 1 ML Tl with 1/3 ML Pb having $\sqrt{3} \times \sqrt{3}$ periodicity on Si(111) appears to be a 2D material which combines together the giant Rashba-type spin splitting (~250 meV) with the superconductivity at sizable transition temperature of 2.26 K. By comparing this transition temperature with the temperature predicted from the electron-phonon interaction found by ARPES, it was found that the strong electron-phonon interaction of one Rashba split surface band causes superconductivity. When the spin orbit interaction energy is larger than the superconducting gap, an opportunity is provided to observe a number of fascination phenomena; In conventional superconductors the electron pairs are in a spin-singlet state with antiparallel spins. If the space-inversion symmetry is broken and magnitude of the spin splitting is sufficiently larger than the superconducting gap, the interband Cooper pairing between electrons in the two spin-split bands is strongly suppressed. As a result, the pairing state in one band is the admixture of the spinsinglet and spin-triplet pairing [1, 2] which leads to the advanced properties some of which have already been considered theoretically [1, 2, 24–28] and experimentally [29]. In particular, it was predicted that in such systems spin magnetic susceptibility becomes anisotropic and Knight shift retains finite and rather high value at T=0 [1, 2]. Furthermore, in-plane magnetic field applied to the 2D superconductor with sizable spin-orbit coupling would induce an in-plane superconducting flow [25]. Strong spin-orbit interaction is expected to broaden the range of existence of the Larkin-Oychinnikov-Fulde-Ferrell phase, which would take the form of periodic stripes running along the field direction on the surface, leading to the anisotropy of its properties [3, 4, 24, 26]. In addition, triplet supercurrent can carry a net spin component and so offer the potential to the superconducting spintronics [28].

References

- 1. L.P. Gor'kov, E.I. Rashba, Phys. Rev. Lett. 87, 037004 (2001)
- 2. V. Edel'shtein, Sov. Phys. JETP 68, 1244 (1989)
- 3. O.V. Dimitrova, M.V. Feigel'man, J. Exp. Theor. Phys. Lett. 78(10), 637 (2003)
- 4. O. Dimitrova, M.V. Feigel'man, Phys. Rev. B 76, 014522 (2007)
- 5. S. Fujimoto, J. Phys. Soc. Jpn. 76, 051008 (2007)
- K. Sakamoto, T. Oda, A. Kimura, K. Miyamoto, M. Tsujikawa, A. Imai, N. Ueno, H. Namatame, M. Taniguchi, P.E.J. Eriksson, R.I.G. Uhrberg, Phys. Rev. Lett. 102(9), 096805 (2009)
- 7. J. Ibañez-Azpiroz, A. Eiguren, A. Bergara, Phys. Rev. B **84**(12), 125435 (2011)
- 8. K. Sakamoto, T.H. Kim, T. Kuzumaki, B. Müller, Y. Yamamoto, M. Ohtaka, J.R. Osiecki, K. Miyamoto, Y. Takeici, A. Harasawa, S.D. Stolwijk et al., Nat. Commun. 4, 2073 (2013)
- S.D. Stolwijk, A.B. Schmidt, M. Donath, K. Sakamoto, P. Krüger, Phys. Rev. Lett. 111(17), 176402 (2013)
- S.D. Stolwijk, K. Sakamoto, A.B. Schmidt, P. Krüger, M. Donath, Phys. Rev. B 90(16), 161109 (2014)
- 11. K. Yaji, Y. Ohtsubo, S. Hatta, H. Okuyama, K. Miyamoto, T. Okuda, A. Kimura, H. Namatame, M. Taniguchi, T. Aruga, Nat. Commun. 1, (2010)

References 91

- 12. S. Hatta, T. Noma, H. Okuyama, T. Aruga, Phys. Rev. B 90, 245407 (2014)
- 13. D.V. Gruznev, L.V. Bondarenko, A.V. Matetskiy, A.A. Yakovlev, A.Y. Tupchaya, S.V. Eremeev, E.V. Chulkov, J.P. Chou, C.M. Wei, M.Y. Lai, et al., Sci. Rep. 4, (2014)
- D. Gruznev, L. Bondarenko, A. Matetskiy, A. Tupchaya, A. Alekseev, C. Hsing, C. Wei, S. Eremeev, A. Zotov, A. Saranin, Phys. Rev. B 91, 035421 (2015)
- A.V. Matetskiy, S. Ichinokura, L.V. Bondarenko, A.Y. Tupchaya, D.V. Gruznev, A.V. Zotov, A.A. Saranin, R. Hobara, A. Takayama, S. Hasegawa, Phys. Rev. Lett. 115(14), 147003 (2015)
- 16. S.H. Uhm, H.W. Yeom, Phys. Rev. B **86**, 245408 (2012)
- 17. C. Kittel, *Introduction to Solid State Physics* (Wiley, 2005)
- 18. M. Yamada, T. Hirahara, R. Hobara, S. Hasegawa, H. Mizuno, Y. Miyatake, T. Nagamura, e-J. Surf. Sci. Nanotechnol. **10**, 400 (2012)
- 19. K. Horikoshi, X. Tong, T. Nagao, S. Hasegawa, Phys. Rev. B 60, 13287 (1999)
- 20. A. Larkin, A. Varlamov, Theory of Fluctuations in Superconductors (Clarendon Press, 2005)
- 21. R.S. Thompson, Phys. Rev. B 1, 327 (1970)
- 22. M. Yamada, T. Hirahara, S. Hasegawa, Phys. Rev. Lett. 110, 237001 (2013)
- 23. B. Halperin, D.R. Nelson, J. Low Temp. Phys. **36**(5–6), 599 (1979)
- 24. V. Barzykin, L.P. Gor'kov, Phys. Rev. Lett. 89, 227002 (2002)
- 25. S.K. Yip, Phys. Rev. B 65, 144508 (2002)
- 26. K. Michaeli, A.C. Potter, P.A. Lee, Phys. Rev. Lett. 108, 117003 (2012)
- 27. J.P.A. Devreese, J. Tempere, C.A.R. Sá de Melo, Phys. Rev. Lett. 113, 165304 (2014)
- 28. J. Linder, J.W. Robinson, Nat. Phys. 11(4), 307 (2015)
- 29. T. Sekihara, R. Masutomi, T. Okamoto, Phys. Rev. Lett. 111, 057005 (2013)

Chapter 6 Intercalation Compounds of Bilayer Graphene

Abstract Study about doping-induced superconductivity in carbon allotropes has long history. Graphene, which is an rapidly growing subject in condensed matter research in this decade, is not the exception. Even though the as-grown graphene is far from superconductivity due to its semimetallic nature, A few groups have succeed to synthesize metal-doped graphene which show sign of superconductivity. Since their research totally differs in not only synthesis but detection method, however, it is still controversial issue to determine the driving force and establishment of superconductivity. In this chapter, the first demonstration of electrical transport measurements on metal-intercalated bilayer graphene is presented, where Ca-intercalated bilayer graphene exhibits superconducting transition at 2 K while Li-intercalated one do not. This result supports the interlayer-band origin of superconductivity, which has been conventionally suggested in graphite intercalation compounds.

Keywords Graphite · Graphene · Intercalation · Superconductivity

6.1 Background

Since graphite was discovered in the 1560s, carbonaceous materials have stimulated the interest of scientists. Various allotropes such as graphite, diamond, fullerene, carbon nanotube, and graphene have been discovered and studied from lots of aspects. Superconductivity is one of the most attractive phenomena among them. In 1965, it was reported by Hannay and colleagues that KC_8 , where potassium atoms intercalate between carbon layers of graphite shows superconductivity below 200 mK [1]. This finding was so striking because neither graphite nor inserted alkali metal show superconductivity as elemental metals. Potassium intercalation can also induce superconductivity to the fullerene at 18 K, as reported by Hebard et al. [2]. Afterwords, $RbCs_2C_{60}$ was demonstrated to be a superconductor with T_c of 33 K by Tanigaki et al. [3]. Several groups reports superconductivity in carbon nanotube, but it is still controversial due to the difference of experimental condition [4]. Boron-doped diamond is found to be a superconductor in 2004 [5].

Hence, most of the carbon allotropes are proved to be superconductors. Generally saying, their origin of superconductivity is understood as the BCS mechanism, so the electron-phonon interaction plays the key to role to develop the superconductivity. High $T_{\rm c}$ of fullerene is driven by its intramolecular vibration and the high density of state. If the diameter of carbon nanotube is sufficiently small, one-dimensional state density divergence occurs and coupling with phonons in the tube diameter direction raise $T_{\rm c}$ up to 64 K [6]. For the case of graphite intercalation compounds, electron-phonon interaction changes according to the intercalate element and composition as described below.

6.1.1 Graphaite Intercalation Compounds

Graphite intercalation compound (GIC) is synthesized by the penetration of metal between carbon layers maintaining the stacked structure of graphite. So far, more than several hundreds of GICs have been discovered and attracted considerable interests for advanced physical properties such as high conductivity and magnetism. Intercalation of group 1–3 metal is especially important for the seeking of superconductivity that many studies have been done to study the effect of electron doping [7]. In 2005, Weller et al. overcame the difficulty to synthesize C_6Yb and C_6Ca , whose T_c are 6.5 K and 11.5 K, respectively [8]. The 11.5 K for C_6Ca was epoch making because it has much higher T_c than any other GIC. Intensive research was conducted to clarify the mechanism of superconductivity in C_6Ca . The temperature dependence of specific heat [9], the magnetic penetration depth [10], and the gap shape of the tunnel spectrum [11] indicates s-wave nature of C_6Ca .

In order to specify the electronic state that is responsible for superconductivity, first-principles calculations were actively carried out. Csányi et al. performed a systematic band calculation on C_6Yb and C_6Ca [12]. According to their calculation, interlayer band (ILB), which is originally unoccupied state in graphite, whose wavefunction is distribute between layers, is filled by electron in superconducting GICs. Although the state has weak characteristics of intercalants' orbital (e.g. 5*d* in C_6Yb case), it is still called ILB for convenience. ILB locates at the Γ point and has free-electron like feature, i.e. parabolic dispersion and circular Fermi surface.

Sugawara et al. measured band dispersion in bulk C_6Ca crystals by the low temperature ARPES. As shown in Fig. 6.1a, a metallic state is observed at the Γ point in addition to the π^* band derived from graphite near the K point. The shape of the Fermi surface at the Γ point is circular, i.e. free electronic like (Fig. 6.1b). It is possible that π^* bands is folded and callapse to Γ point due to Ca-induced $\sqrt{3} \times \sqrt{3}$ Brillouin zone. In that case, however, the Fermi surface shape should be a hexagon. Therefore, it is concluded that this metallic state is ILB rather than π^* band. It is observed that photoelectron spectra of ILB and π^* band discontinuously changes due to the coupling of C_z phonon and C_{xy} phonon π^* band, respectively. This means that the π^* band is two-dimensional, while ILB has a three-dimensional nature, which strongly couple with the phonon in the vertical direction. Furthermore, the temperature dependence of the contraction of the contraction of the phonon in the vertical direction.

6.1 Background 95

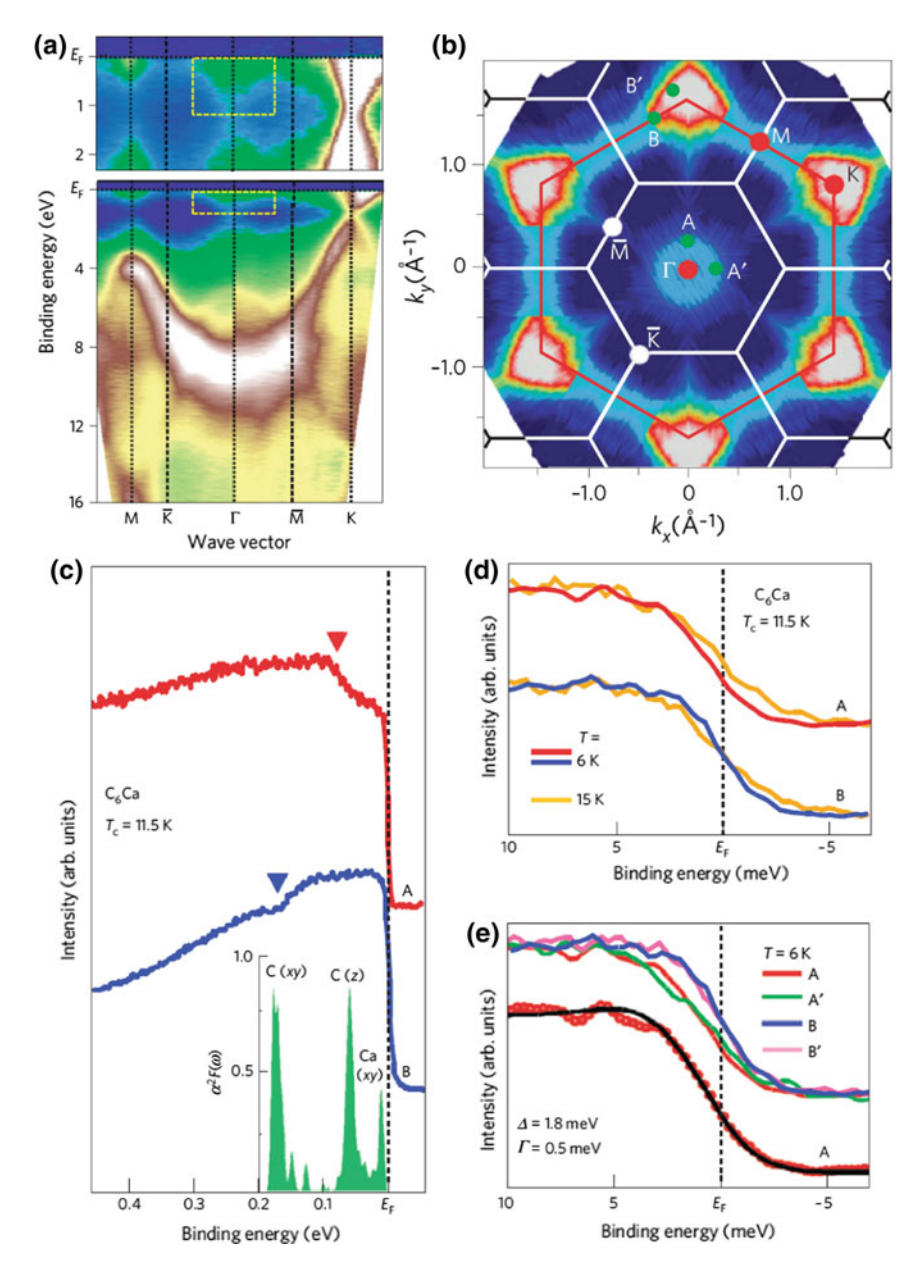


Fig. 6.1 ARPES-experimental result on C_6Ca [46]. a Band dispersion. An interlayer band is observed in the area marked by the dashed frame. b Fermi surface mapping. c Photoelectron spectra at 6 K, measured at the points A and B (red and blue). The green histgram indicates calculated Eliashberg function $\alpha^2 F(\omega)$ as a function of binding energy. d, e Temperature dependence of photoelectron spectrum. A, A', B, B' are the points indicated in b. Reprinted with permission from Ref. [46]

dence of the photoelectron spectrum has also been measured (see Fig. 6.1d). In the π^* band, the Fermi energy does not move from the midpoint of the spectrum edge, and can be explained by the temperature dependence of the Fermi distribution function. On the other hand, in the ILB, the edge of the spectrum shifts at a low temperature (leading edge shift), indicating that the density of state change due to the opening of superconducting gap. The magnitude of the superconducting gap estimated from the shift amount is 2 meV. Also, according to measurements at different positions on the Fermi surface, the superconducting gap is isotropic (see Fig. 6.1e).

However, more recent ARPES measurements showed kink structure in the band dispersion and leading edge shift in the photoelectron spectrum in both ILB and π^* bands. It is claimed that both of the bands contribute to superconductivity [13]. The electron-phonon coupling constants estimated from the kink structure are 0.20 for π^* band $-C_{xy}$ phonon, 0.23 for π^* band C_z phonon, and 0.22 for ILB- C_z phonon. This assertion suggests that graphene sheets themselves may be superconducting.

6.1.2 Metal Doping to Graphene

Graphene is a one-atomic-layer-honeycomb-network of carbon atoms. Since graphene was isolated using Scotch tape by Novoselov et al. in 2004 [14], graphene has been a central research subject in the field of nanomaterials owing to its strong two-dimensional nature and various novel properties such as the massless electrons [15], the high carrier mobility [16] and the remarkable mechanical strength and flexibility [17]. Several methods, such as mechanical exfoliation and epitaxial growth on various substrates [18, 19] have been employed to obtain a high-quality graphene film with a large working area, especially for application to electronic devices.

Superconducting graphene has been a target of intensive studies since the discovery of graphene, because it realizes an intrinsic two-dimensional and self-standing 2D superconductor. Many intensive efforts have been made to fabricate superconducting graphene by doping metals like in bulk GICs. The successful reports are listed in Table. 6.1. The superconductivity in few-layer graphene was reported by Xue and Tiwari et al. [20, 21]. Intercalation of K or Li several layers of graphene was carried out with chemical methods. It is noteworthy that these studies report higher T_c s than those of bulk counterpart. This is said to be low-dimensional effect; In three-dimensional GICs, smaller separation of graphene layer enhances electronphonon coupling, resulting in higher T_c . However, when the distance is too small, the superconductivity is destroyed because a strong confinement of the interlayer state in a narrow region shifts the intercalant band well above the Fermi energy, indicative the non-superconductive condition [22]. The bulk LiC₆ is not superconducting due to the confinement effect. For the case of monolayer graphene, the confinement is removed and empty interlayer state can be returned to the Fermi level, according to the DFT-LDA calculation by Profeta et al. [23]. In this sense, light alcali metals such as Li or K become promising dopant for the superconductivity.

6.1 Background 97

Table 6.1	Summary of previous	reports of superconductivity	in alkaline or alkaline earth doped
graphene			

Thickness	Growth	Dopant	Condition	Method	$T_{c}(K)$	Bulk counterpart $[T_c(K)]$	Refs.
10	Epitaxy	Ca	ex citu	Magnetization	7	CaC ₆ [11 K]	[24]
5	Flake	Li	ex citu	Magnetization	7.4	N/a	[21]
4	Flake	K	ex citu	Magnetization	5.4	KC ₈ [0.8 K]	[20]
1	Epitaxy	Li	in citu	ARPES	5.9	N/a	[29]

It should be noted that, however, they are still not monolayer and the crystal structure is undefined in the ambient condition, since contamination of sample cannot be avoided in such multilayer graphene. For example, in Ref. [24], where intercalation of Ca into 10-layer graphene prepared on SiC by heating it in the melting Li-Ca alloy, the authors claim that it is necessary to protect the sample by intentionally leaving the Li-Ca alloy on the surface to protect the sample during transfer to the magnetization measurement [24]. Therefore, it is uncertain that the enhancement of T_c is originated from the ultrathin-thickness effect. In order to obtain a certain evidence of superconductivity in monolayer graphene, ultra high vacuum is ideal environment from sample fabrication to evaluation. Hence, lots of ARPES measurements have been carried out on metal-doped monolayer graphene. It has been clarified that when the single layer graphene is doped with an alkali metal or an alkaline earth metal, the kink structure is seen in the π^* band, and the electron-phonon interaction increases [25–28]. In particular, it is noteworthy that a recent work by Ludbrook et al. reported enhanced electron-phonon interaction upto $\lambda = 0.58$ by Li doping [29], which is larger than that reported by Fedorov et al. ($\lambda = 0.29$) [27]. The interpretation is as follows; They performed both Li deposition and in situ ARPES measurements at very low temperatures below 8 K, without warming up the sample. At such low temperature, Li orders on the surface without intercalating to the interface between graphene and substrate. According to the theory by Profeta et al., when the adsorption structure of Li with $\sqrt{3} \times \sqrt{3}$ periodicity on the surface of graphene, ILB appears below the Fermi level. As a result, the transition between the π^* band and C_z phonon is strengthens the coupling with the Cz phonon, which increases the total electronphonon interaction [23]. Indeed, in the spectroscopic study of Ludbrook et al., a circular Fermi surface appears at the Γ point, indicating that the ILB is crossing the Fermi level. As a result, the electron-phonon interaction of the π^* band increases, and furthermore, it is claimed that a superconducting gap was observed. Since the $\sqrt{3} \times \sqrt{3}$ ordered structure and these features vanish at the same time when the sample is warmed up, the experimental results are consistent to Profeta's theory.

Despite of novelty of the ARPES study, there remains the difficulty of sample preparation at low temperature. In particular, structural study by scanning probe has never been performed about the metal decoration on graphene. On the other hand, metal intercalation to bilayer graphene has been investigated comprehensively by ARPES and STM as follows.

6.2 Structural Properties of Intercalation Compounds of Bilayer Graphene

6.2.1 Graphene on SiC

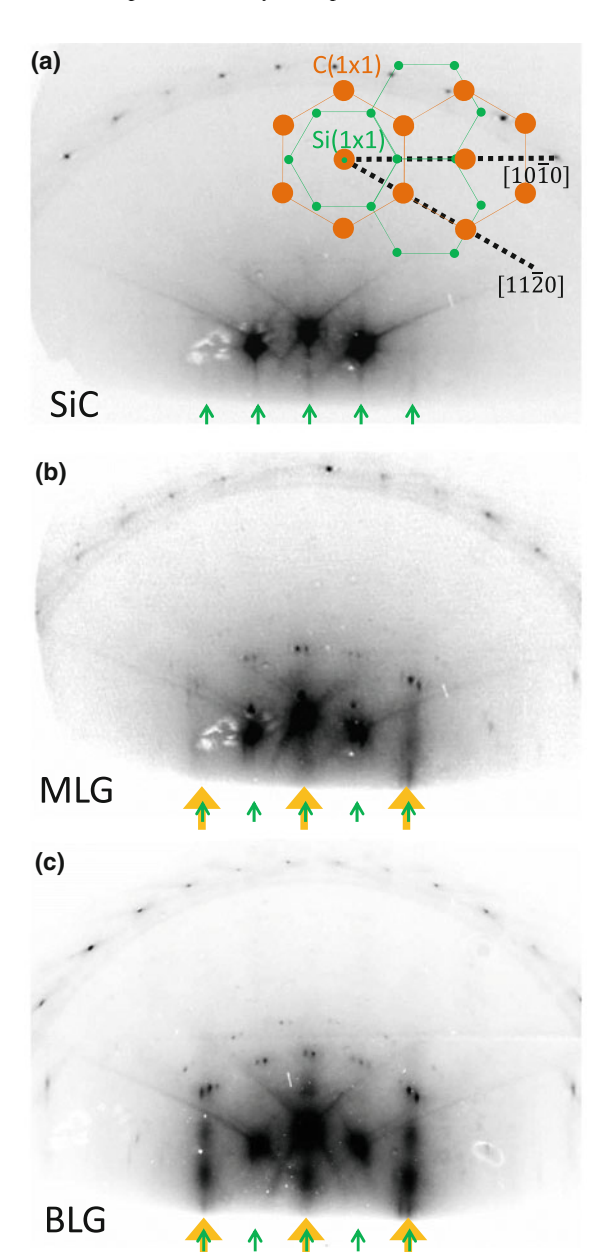
One of the epitaxial methods for preparing large area graphene is to reduce SiC by heating it to 1100° C or higher (desorption method) [30]. Desorption of Si from the topmost surface promotes the reconstruction of remaining carbon into graphene. SiC has a (0001) face (Si face) which is terminated with Si while a (0001) face (C face) terminated with C. When graphene is prepared on the Si surface, free standing graphene is epitaxially grown on the "buffer layer", which is covalently bonded to SiC. It is known that the graphene layer shows metallic conduction, while the buffer layer does not contribute to the conductivity [31]. It is possible to control the number of layers of graphene to be produced by changing the heating temperature and time. Confirmation of the thickness after growth is also done by Raman spectroscopy, electron microscopes, etc. ARPES is also used for the identification because the π band splits depending on the number of layers [32].

From now on, let us focus on graphene grown on SiC(0001). Inset of Fig. 6.2a displays a schematic illustration of surface reciprocal lattice of SiC and graphene. The unit cell of graphene [C(1 \times 1), orange dots] rotates 30° with respect to SiC surface [Si(1 \times 1), green dots]. Figure 6.2a–c shows the RHEED figure of bare SiC, single layer graphene, and bilayer graphene obtained in this study. Since the incident direction of the RHEED electron beam is [11 $\bar{2}$ 0], the diffraction points aligned in the direction of [10 $\bar{1}$ 0] appears on the 0th Laue zone, as indicated by orange [C(1 \times 1)] and green [Si(1 \times 1)] arrows. Comparing the RHEED pattern of single/double layer graphene in Fig. 6.2b, c, double layer one has brighter C(1 \times 1) spot. In addition, one can see the $6\sqrt{3} \times 6\sqrt{3}$ periodic structure due to the commensurate lattice matching between the buffer layer and the SiC substrate.

6.2.2 Atomic Arrangement

When Li and Ca are intercalated into bilayer graphene prepared on SiC, as shown in Fig. 6.3a, they form ordered structure with a periodicity of $\sqrt{3} \times \sqrt{3}$ with respect to the unit cell of graphene. Therefore, the presence or absence of intercalation can be

Fig. 6.2 RHEED patterns on a SiC(0001) -1×1 , b monolayer graphene and ${\bf c}$ bilayer graphene on SiC. The spots pointed by green and orange arrows are originated from 1×1 of SiC [Si(1 × 1)] and graphene $[C(1 \times 1)]$, which are interpleted via schematic reciprocal lattice of graphene on SiC, as shown in the inset of a. The green and orange spots come from 1×1 of SiC [Si(1 × 1)] and graphene $[C(1 \times 1)]$, respectively



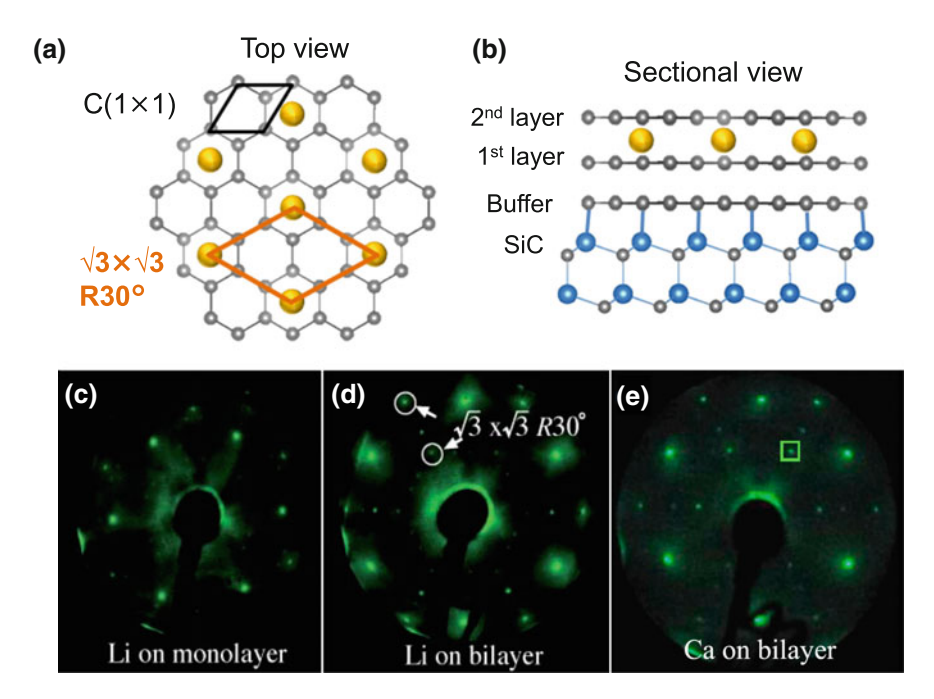


Fig. 6.3 a, **b** Schematic crystal structure of bilayer graphene intercalation compound C_6LiC_6 or C_6CaC_6 on SiC from **a** top view and **b** side view. **c**, **d** LEED patterns. **c** Monolayer graphene after vapor deposition of Li at room temperature on it [33]. **d** C_6LiC_6 [34]. **e** C_6CaC_6 Reprinted with permission from Refs. [33, 34]

determined by electron diffraction. The composition of the intercalated structure of Li and Ca in bilayer graphene is C_6LiC_6 and C_6CaC_6 respectively. When depositing Li at room temperature on the double layer graphene, $\sqrt{3} \times \sqrt{3}$ spot appears in the LEED figure like Fig. 6.3d [33]. Even if the same treatment is applied to single-layer graphene, the $\sqrt{3} \times \sqrt{3}$ structure does not appear (Fig. 6.3c). This suggests that Li forms ordered structure only in between the two graphene layers, not on the topmost surface or around the buffer layer. (see Fig. 6.3b).

Unlike Li, intercalation of Ca cannot be done directly on pristine bilayer graphene [34]. This is because the atomic radius of Ca is 30% larger than that of Li. In the case of bulk Ca-GIC, Ca intercalation is carried out by heating graphite in an alloy of Li and Ca. First, Li intercalates into graphite. It expands the interlayer distance and then Ca can penetrates into graphite, replacing Li. In order to perform Ca intercalation in bilayer graphene, a pseudo-method is taken in ultra-high vacuum. That is, after intercalating Li by vapor deposition at room temperature, Ca is also deposited at room temperature and promotes substitution from Li to Ca by post annealing. Then, $\sqrt{3} \times \sqrt{3}$ spot becomes sharper in the LEED pattern as shown in Fig. 6.3d, e [34].

It was confirmed by the STM measurement that the change in this LEED pattern indicates the substitution of Li to Ca [35]. Figure 6.4 shows the STM images of

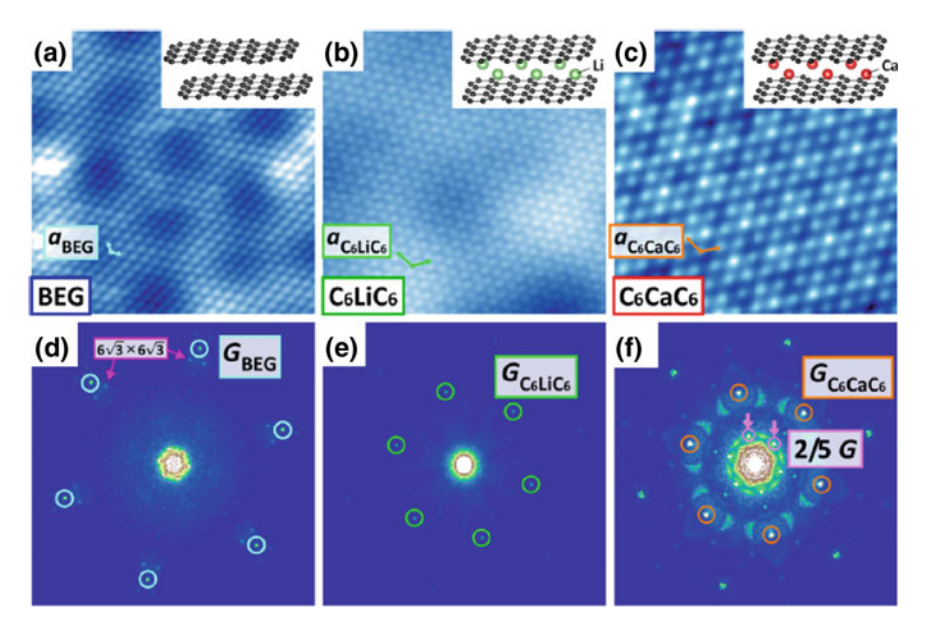


Fig. 6.4 a-c Atomically resolved STM and d-f fast Foulier transformed images of bilayer graphene on SiC (a, d), C_6LiC_6 (b, e) and C_6CaC_6 (c, f)[35]. The scanning area of a-c is 6×6 nm². Schematic illustrations of crystal structures are shown as the inset in a-c. Reprinted with permission from Ref. [35]

pristine bilayer graphene, C₆LiC₆ and C₆CaC₆ in a–c, and their Fourier transformed figure in d-f. The scanning range of all STM images is $6 \times 6 \text{ nm}^2$. In Fig. 6.4a, moiré structure with a large period was clearly observed in addition to the same honeycomb lattice as graphite. From the interference pattern of Fig. 6.4d, it can be seen that moiré has a period of $6\sqrt{3} \times 6\sqrt{3}$ same as the diffraction pattern, so it is derived from the buffer layer. When intercalating Li, moiré disappears and weak $\sqrt{3} \times \sqrt{3}$ structure appears as can be seen in Fig. 6.4e, denoted as $G_{C_6LiC_6}$. This is consistent with the diffraction pattern of Fig. 6.3d. Furthermore, the STM image changes markedly by intercalating Ca. The $\sqrt{3} \times \sqrt{3}$ periodic structure became clear even in the real space image, and the point of 2.5 times period appeared in the Fourier-transformed image Fig. 6.4f, denoted as 2/5 G. Clear observation of $\sqrt{3} \times \sqrt{3}$ pattern in the topographic image suggests a presence of electronic states derived from intercalant near the Fermi surface. In addition, since the ratio 2.5 coincides with the lattice constant difference between the $\sqrt{3} \times \sqrt{3}$ structure and SiC, it was concluded that a charge density wave (CDW) is triggered by the lattice matching condition of C₆CaC₆ with the substrate [35]. Although C₆LiC₆ has the same lattice configuration, CDW is not observed. It comes from the difference of Fermi surface shape as mentioned in the next section.

6.2.3 Electronic Structure

Figure 6.5a-c shows ARPES-obtained band dispersion of bilayer graphene, C_6LiC_6 and C_6CaC_6 [33, 34]. For the bilayer graphene, one can see the π band at the K point and the σ band at the Γ point. The top of the π band, the so-called Dirac point, is located near the Fermi energy. According to the high resolution measurement in the vicinity of E_F , there is a gap of about 0.12 eV with the π^* band. It is known that the interaction with the SiC substrate can not be ignored [33]. The Fermi wave number is $0.05 \, \text{Å}^{-1}$, and the carrier density obtained from the area of the Fermi surface is 0.004 per unit cell. The Fermi velocity of the π^* band is generally 10 ⁶ m/s. Figure 6.5b and c are the band dispersion of C₆LiC₆ and C₆CaC₆, respectively. They shift to the high binding energy side for ca. 1.4 eV, and the metallic state appears at the Γ point. The rigid shift of the bands means electron transfer from Li and Ca to graphene bands. There are two possibilities regarding the state of the Γ point. One is the free electronic state (ILB) that was seen in bulk C₆Ca. Another possibility is π^* bands, which is folded back from K point and appear at the Γ point due to Ca-induced $\sqrt{3} \times \sqrt{3}$ Brillouin zone. Figure 6.5d, e display Fermi surface of C₆LiC₆ and C₆CaC₆, respectively. The hexagon shown by the solid white line is Brillouin zone of C(1×1), while the dotted line is Brillouin zone of the $\sqrt{3} \times \sqrt{3}$ structure. The triangular state seen at point K comes from the π^* band. Compared with the Fermi surface of the corresponding bilayer graphene (shown as the inset of Fig. 6.5d), the Fermi wave number is increased to 0.2 Å^{-1} due to the energy shift of the band, and the area is enlarged and split as can be seen in high resolution measurements [33, 34]. The other state seemingly has a complicated shape, but considering Brillouin zone folding, it can be explained by returning π^* band including snowflake-like state seen at Γ point. However, there is one more state in the case of C_6CaC_6 found by high resolution measurement near the Γ point [34].

As can be seen in Fig. 6.5h and i, there is a parabolic state besides the wrapped π^* band (split to π_{inner}^* and π_{outer}^*). Since there is no difference in shape in $\Gamma - K$ direction (h), $\Gamma - M$ direction (i), it seems an isotropic band, to be considered as the ILB that was seen in C₆Ca. On the other hand, in C₆LiC₆, ILB is absent below Fermi level as shown in Fig. 6.5g. The results of these ARPES measurements are consistent with the calculation results of Mazin [36] and Jishi [37]. Therefore, superconductivity originating in ILB similar to bulk is predicted in C₆CaC₆. It is noteworthy that C₆CaC₆ has ILB below the Fermi level even though Ca density is 1/2 compared to bulk C₆Ca. The carrier density per unit cell obtained from the area of the Fermi surface is 1.07 in C₆LiC₆ and 2.02 in C₆CaC₆ [33, 34]. In addition, the effective mass of ILB is calculated as $m^* = 0.6m_e$ by parabolic fitting [34]. The Fermi wave number is 0.2 Å⁻¹, so the Fermi velocity is obtained as 0.4 × 10⁶ m/s.

The scattering vector of the CDW $(2/5G = q_{\text{CDW}})$ corresponds to the scattering in the π_{inner}^* band as shown in the Fermi surface (Fig. 6.5e white arrow) [35]. Because the Fermi surface of C₆LiC₆ is smaller than that of C₆CaC₆, the scattering in the π_{inner}^* band does not match 2/5G and the CDW does not appear. The STS spectrum

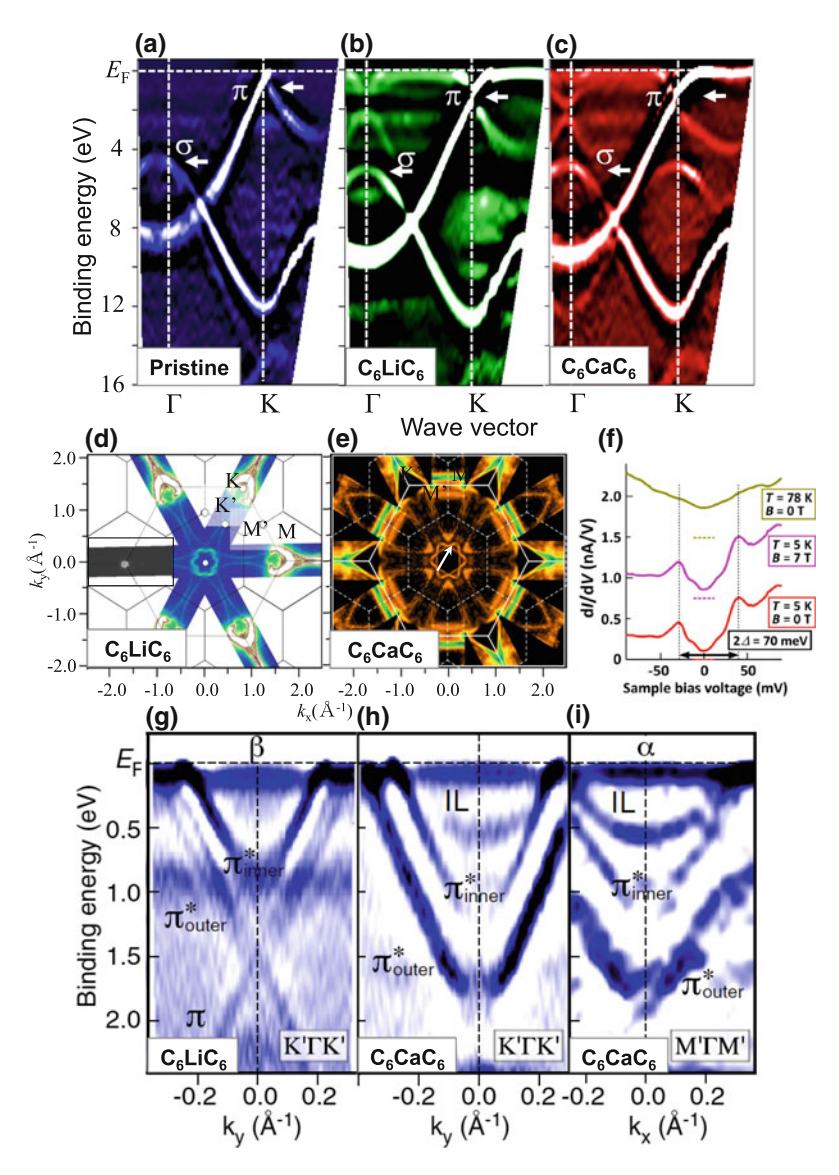


Fig. 6.5 Results of spectroscopic measurements on bilayer graphene and its intercalation compounds [33–35]. **a–c** ARPES-obtained band dispersion in Γ – K direction. **a** double layer graphene, **b** C₆LiC₆ and **c** C₆CaC₆. **d**, **e** Fermi contour mapping by ARPES. The white solid and dotted line corresponds to Brillouin zone of graphene and $\sqrt{3} \times \sqrt{3}$ structure, respectively. **d** C₆LiC₆. The inset is the Fermi side of two-layer graphene. **e** C₆CaC₆. White arrow corresponds to CDW scatter vector. **f** STS spectrum of C₆CaC₆, taken at different temperature and magnetic field. **g–i**, Highly resolved band dispersion near the Γ point by ARPES. **g** C₆LiC₆ in Γ – K direction. h and i, C₆CaC₆ in Γ – K and Γ – M direction. Reprinted with permission from Refs. [33–35]

of C₆CaC₆ at 5 K is displayed in Fig. 6.5f, indicating a gap opening of 70 meV. This is not a superconducting gap because it was observed even under a strong magnetic field of 7 T.

6.3 Purpose of This Study

As described above, for the creation of superconducting graphene, it is pointed the importance of electron occupancy to ILB and the modification of elemental dependence from that of GIC due to the absence of quantum confinement. However, there are only sporadic reports to succeed to make graphene superconductivity and no study has been performed to compare dopant dependence on well-defined sample, under ideal conditions.

In this sense, bilayer graphene is one of the ideal platform to study since the atomic structure and electronic state of the bilayer graphene intercalate compounds are well investigated by ARPES and STM. In particular, with respect to C₆CaC₆, the presence of ILB has been verified experimentally and theoretically [34, 36, 37].

In this research, in situ experimental studies are performed in an ultrahigh vacuum from preparation of Li- and Ca-intercalated bilayer graphene to low temperature measurements, in order to examine the relation between transport properties and the elemental-dependent band structures.

The following results and discussions are based on the content of a published article [38]: "Superconducting Calcium-Intercalated Bilayer Graphene" S. Ichinokura, K. Sugawara, A. Takayama, T. Takahashi and S. Hasegawa: ACS nano 10, 2761-2765 (2016).

6.4 Electrical Transport Studies on Intercalation Compounds of Bilayer Graphene

6.4.1 Sample Preparation

Bilayer graphene was prepared by heating an n-type 6H-SiC (0001) substrate to 1550° C by heating under an Ar atmosphere of 0.1 MPa, and it was identified as bilayer by ARPES observation. After transferring it through the air, it was introduced into the UHV-4PP system equipped with RHEED. The surface was cleaned by annealing at about 400° C for several hours. The RHEED image after cleaning is shown in Fig. 6.6a. C(1 × 1), Si (1 × 1) and $6\sqrt{3} \times 6\sqrt{3}$ periodic spots are observed, same as Fig. 6.2c. SAES-Getters' dispenser is used for Li deposition. Ca is deposited from an alumina effusion cell with tungsten filament for dc current heating. To prevent contamination of highly reactive Ca, the surface oxide layer of Ca is removed in the Ar atmosphere glove box and the cell quickly place in the vacuum. Also, even

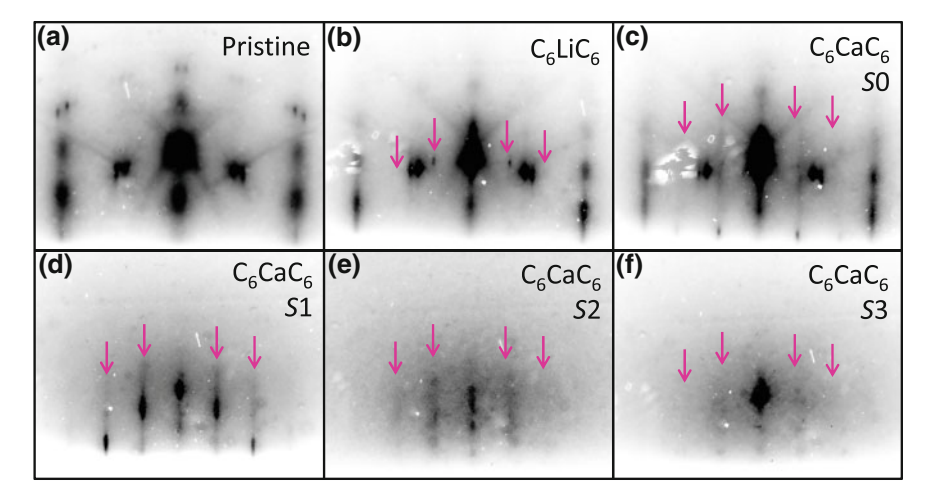


Fig. 6.6 RHEED patterns of bilayer graphene and its intercalation compounds around 0th Laue zone. **a** Pristine bilayer graphene. **b** C_6LiC_6 . **c** C_6CaC_6 made by the single Li-Ca replacing treatment (called S0). **d**, **e** C_6CaC_6 made by repeating the replacement process on three different substrates (called S1-3)

in vacuum, the inner wall is covered with tantalum foil so that Ca does not directly touch the inner wall of the alumina crucible.

When we evaporated Li atoms onto this BLG sheet at room temperature, several sharp $\sqrt{3} \times \sqrt{3}$ spots emerged in the RHEED pattern (pink allows Fig. 6.6b), indicating that Li atoms are regularly intercalated between two adjacent graphene layers. After confirming the growth of Li-intercalated BLG (C₆LiC₆), Ca was deposited on this C₆LiC₆ sheet to replace Li with Ca atoms. During the Ca deposition, we kept the substrate at 150°C, slightly above the Li desorption temperature of 145°C. Since this change was observed with good reproducibility by same procedure, it is thought that it is derived from substitution from Li to Ca. The Ca deposition transformed the $\sqrt{3} \times \sqrt{3}$ spots into streaks (Fig. 6.6c), suggesting that intercalated Li atoms are replaced by Ca atoms. However, not all the area of sample was converted into C₆CaC₆ at this early stage, because repeated cycles of Li and Ca deposition together with annealing made the $\sqrt{3} \times \sqrt{3}$ streaks brighter and brighter. We call the sample at this early stage sample S0. After several cycles of deposition and annealing, we finally obtained the very sharp $\sqrt{3} \times \sqrt{3}$ streaks in the RHEED pattern (Fig. 6.6d), indicative of formation of well-ordered C₆CaC₆ in large area. We call this sample S1. Figure 6.6e and f shows RHEED images of C₆CaC₆ samples S2 and S3 prepared in the same way on other SiC substrates.

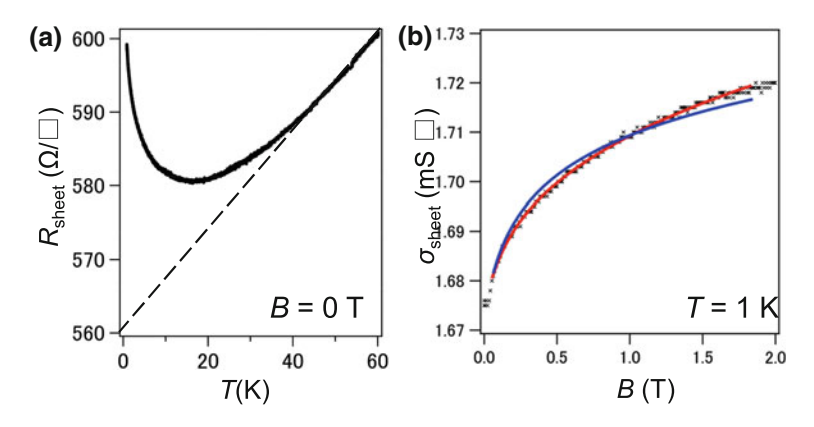


Fig. 6.7 Electrical transport characteristics of bilayer graphene [38]. **a** Temperature dependence displayed as a R-T plot. **b** Magnetic field dependence displayed as a $\sigma-B$ plot. The red and blue solid lines are least-squares fits to the formula Eq. (6.2) with positive and negative signs for the third term, respectively

6.4.2 Results on Pristine Bilayer Graphene

The prepared samples were transferred to a low temperature electric conduction measuring stage at each stage and measurements were carried out at low temperature. First, the measurement results of the sheet resistance of the typical bilayer graphene obtained in this study are shown in Fig. 6.7a. At temperatures higher than 20 K, the resistivity decreases with cooling and metallic behavior is seen. Residual resistance is estimated as ca. $560~\Omega$ if the metallic region is extrapolated to 0 K.

It showed a insulating behavior in which the resistivity increased lower than 20 K. As mentioned in the Sect. 1.1.1, in 2D systems, resistance increases due to weak localization at low temperatures in many cases. The weak localization occurs because standing waves are generated by superposition of time-reversal symmetric backscattering paths. Therefore, if time reversal symmetry is broken by the magnetic field, weak localization is suppressed by Aharonov-Bohm phase. In general, the dependence of the magnetic field on the conductivity is expressed by the following Eq. [39]:

$$\delta\sigma(B) = \frac{e^2}{2\pi^2\hbar} \left[\psi\left(\frac{1}{2} + \frac{\hbar}{4el^2_{\phi}B}\right) - \ln\left(\frac{\hbar}{4el^2_{\phi}B}\right) \right]. \tag{6.1}$$

Here, $\psi(x)$ is the digamma function. In the case of single- and double-layer graphene, this formula is modified as follows [40]:

$$\delta\sigma(B) = \frac{e^2}{\pi^2 \hbar} \left[\mathscr{F} \left(\frac{4e}{\hbar} l_{\phi}^2 B \right) - \mathscr{F} \left(\frac{4e}{\hbar} \frac{B}{1/l_{\phi}^2 + 2/l_i^2} \right) \right]$$

$$\mp 2\mathscr{F} \left(\frac{4e}{\hbar} \frac{B}{1/l_{\phi}^2 + 1/l_i^2 + 1/l_*^2} \right). \tag{6.2}$$

Here, $\mathscr{F}(x) = \ln(x) + \Psi(1/2 + 1/x)$. L_i $(j = \phi, i, *)$ is the relaxation length of phase breaking, inter-valley and intra-valley scattering, respectively. The first term is an ordinary weak localization term, and the second and third term are correction terms due to the effect of the valley degree of freedom in graphene. The sign of the third term is determined by number of layer; negative for monolayer and positive for bilayer. Magnetoresistance measurements were carried out with 1 K and fitted with each relaxation length of the Eq. (6.2) as parameters. The result is shown in Fig. 6.7b. The red line is the result of performing the fitting with the sign of the third term as positive, and reproduces the experimental result well, while good agreement was not obtained when the sign of the third term was taken negative. (The limit of $L_i = L_* = 0$, that is to say to some extent like the blue line in Fig. 6.7b if the second and third terms are zero.) From these analyzes, it was confirmed again that the number of graphene layers used in this study was two. Each relaxation length obtained from the red line fitting is $L_{\phi} = 117 \pm 7$ nm, $L_i = 55 \pm 8$ nm, $L_* = 36 \pm 1$ nm, hence $L_{\phi} > L_i > L_*$. This tendency is the same as a report about single layer graphene on SiC by Lara-Avila et al. ($L_{\phi} \sim 600$ nm, $L_{i} \sim 180$ nm, $L_{*} \sim 20$ nm with 1 K). They also mentions that the momentum relaxation length is about L_* [31] and intravalley scattering originates from irregular potential by donor impurity randomly distributed on SiC [31]. Therefore, it turns out that this determines the mean free path in the bilayer graphene.

6.4.3 Results on C_6LiC_6 and C_6CaC_6

The results of temperature-dependent transport measurements on C_6LiC_6 and C_6CaC_6 (sample S1) are compared in Fig. 6.8. In contrast to the pristine BLG (Fig. 6.7 a), the sheet resistivity of intercalated bilayer graphene is metallic, and their resistance is as low as ca. 10 % of that of pristine bilayer graphene. This is because of the increase of the Fermi-surface volume by the carrier doping from Li or Ca atoms. Actually, according to Refs. [33, 34], the carrier doping by Li and Ca doping is 250 times and 500 times that of the original bilayer graphene when determined from the area of the Fermi surface. However, the increase in conductivity has remained only 10 times. This implies that the mobility is lowered due to defects caused by multi-step intercalation procedure accompanying the heat treatments. Importantly, the transition of sheet resistivity to zero-resistance is clearly seen at around 2 K in C_6CaC_6 , which is the direct evidence for macroscopically coherent superconductivity with $T_c^{zero} = 2$

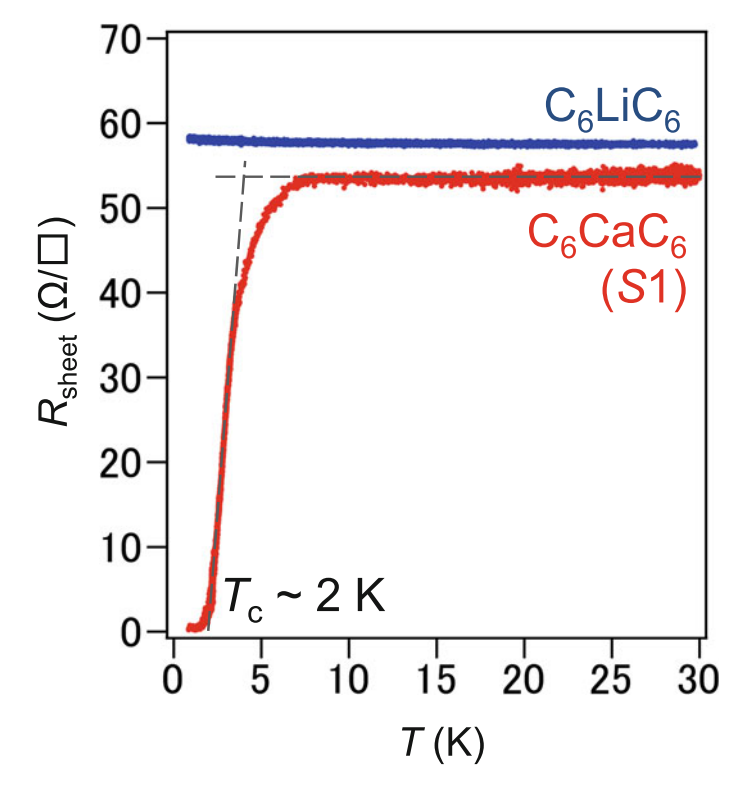


Fig. 6.8 Comparison of temperature dependence of sheet resistance R_{sheet} between $C_6\text{Li}C_6$ (blue) and $C_6\text{Ca}C_6$ (Sample S1, red)[38]. Only $C_6\text{Ca}C_6$ exhibits superconducting transition with $T_c^{onset} = 4 \text{ K}$ and $(T_c^{zero} = 2 \text{ K})$, while $C_6\text{Li}C_6$ shows a slight upturn in resistance at low temperatures

K. It is also noteworthy that C_6LiC_6 shows no sign of superconductivity down to 0.8 K, and instead exhibits a weak localization behavior as evident from a slight upturn in resistance at low temperatures. While the sheet resistance of C_6CaC_6 shows a sharp drop at around 4 K ($T_c^{onset} = 4$ K), it starts to decrease even above 4 K as seen in Fig. 6.7b, qualitatively reproduces the amplitude fluctuation described in the Sect. 2.4.2.

Conversion of the transition temperature $T_c^{zero}=2$ K into a superconducting gap by the formula Eq. (2.132) $\Delta(0)=ak_BT_c(a=1.76-2.2)$ yields $\Delta(0)=0.3-0.4$ meV. Regarding to estimation of the Pippard's coherence length by $\xi_0=\frac{\hbar v_F}{\pi\Delta(0)}$, it is required to have an information about Fermi velocity v_F . According to ARPES, $v_F=1\times10^6$ m/s for π^* band and 0.4×10^6 m/s for ILB. When the π^* (ILB) band is responcible for the superconductivity, the Pippard's coherence length is estimated as $\xi_0=600-700$ (200–300) nm.

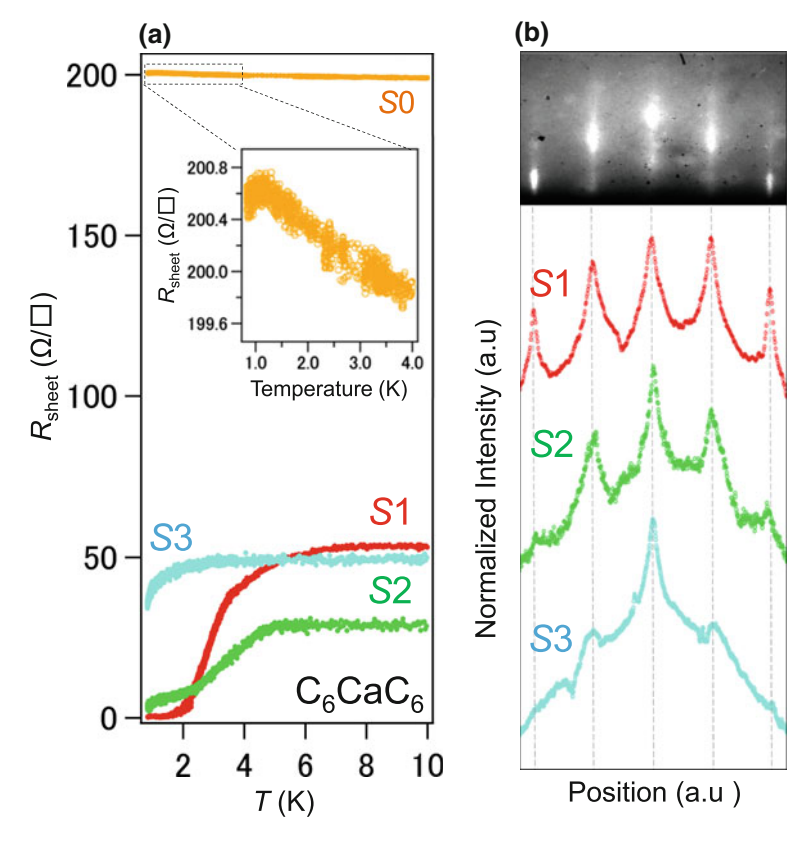


Fig. 6.9 a Comparison of temperature dependence of R_{sheet} among C₆CaC₆ samples S0-3 [38]. Inset shows R_{sheet} of sample S0 from 0.8–4.0 K. **b** Line profiles of RHEED patterns for samples S1–3. The intensity is normalized with the peak height of the central (1×1) streak. The upper column shows the RHEED picture of sample S1

Sample dependence of superconducting property

Figure 6.9a shows the sample-dependent sheet resistivity as a function of temperature. Three samples (S1-3) prepared with the same method as described above reproducibly exhibited superconducting transition. The difference in quality among samples S1-3 is seen in the line profile of RHEED pattern (see Fig. 6.9b), obtained from Fig. 6.6d-f. The central peak is due to the 1 × 1 structure while the side peaks are from the $\sqrt{3} \times \sqrt{3}$ superstructure originating from the intercalated Ca sheet. Figure 6.9a and b show that the sheet resistivity at 0.8 K approaches the zero-resistance when the $\sqrt{3} \times \sqrt{3}$ spot becomes stronger. The fact that S1 with the brightest $\sqrt{3} \times \sqrt{3}$ spot shows a full drop to zero-resistance at 2 K suggests that the ordering in the Ca layer is important to realize the superconductivity. This is confirmed by the experimental fact that the sheet resistivity of sample S0 (early stage sample) shows only a tiny drop near the lowest temperature.

Magnetoresistance of C₆CaC₆

To obtain further evidence for the superconductivity, we conducted magnetoresistance (MR) measurements on C₆CaC₆ (Sample S2), under the magnetic field perpendicular to the sample surface. Figure 6.10a and b show sheet resistivity obtained as a function of temperature at fixed magnetic field and vice versa, respectively. As seen in Fig. 6.10a, the T_c^{onset} is gradually shifted toward lower temperature as the magnetic field is increased. This is consistent to the shift of MR curves depending on temperature in Fig. 6.10b. To see the temperature-dependence of the upper critical field $(H_{c2} = B_{c2}/\mu_0)$, we plot in Fig. 6.11c the magnitude of magnetic field at which the sheet resistance is a half of the normal-state-resistance as a function of temperature. The $\mu_0 H_{c2}$ at 1 K is 100 mT, which is four times larger than that reported in Ca-intercalated 50-layer graphene [24] and is almost the same as that of bulk C₆Ca [8, 41]. We find that the obtained $\mu_0 H_{c2}$ values are well aligned linearly, which suggests that the experimental results can be analyzed in the framework of the GL theory Eq. (2.121). Numerical fittings with the GL theory show that the in-plane GL coherence length at zero Kelvin $\xi(0)$ is 49 ± 1 nm. Although it is thought that variations occur due to the quality of the original bilayer graphene and the heat treatment including intercalation, The GL coherence length of S2 is sufficiently shorter than the Pippard's coherence length of S1, This value is comparable to the momentum relaxation length of pristine bilayer graphene, obtained from the analysis of weak localization in Fig. 6.7a. This indicates that the superconducting coherence length in C₆CaC₆ is limited by scattering at random potential on the SiC surface. However, the $\xi(0)$ in C₆CaC₆ is slightly larger than that of bulk C₆Ca (29–36 nm) [8, 41], probably owing to the high career mobility in graphene. This shows a contrast to the case of surface superconductors such as In on Si(111), where the $\xi(0)$ is \sim 25 nm [42] and much shorter than value of bulk counterpart (250-440 nm)[43]. The upper critical field at absolute zero degree was obtained by extrapolation, then $\mu_0 H_{c2}(0) = 134 \pm 6$ mT was obtained. This is as same order as bulk $C_6Ca \mu_0 H_{c2}(0) \sim 400$ mT [41], but much larger than 50 layered graphene on Ca doped SiC, where $\mu_0 H_{c2}(0) \sim 30$ mT [24]. So systematic thickness dependence cannot be found in these reports.

6.4.4 Discussion

As presented above, only C_6CaC_6 , where ILB is an occupied state becomes superconductivity while pristine bilayer graphene and C_6LiC_6 do not. This result strongly suggests that bilayer graphene conceals the ILB-originated superconductivity in it, which is conventionally thought in GIC as well as graphene.

Here, it is noted that C_6CaC_6 grown on SiC (0001) has been observed as a CDW system at 5 K in the π^* band [35]. In many cases, once CDW occurs it suppresses superconductivity. So Cooper pair formation in the π^* band seem to be hindered by CDW. Therefore, it can be inferred that only the ILB is gapped in the present C_6CaC_6 on SiC. However, in a recent theoretical study without substrate, it was pre-

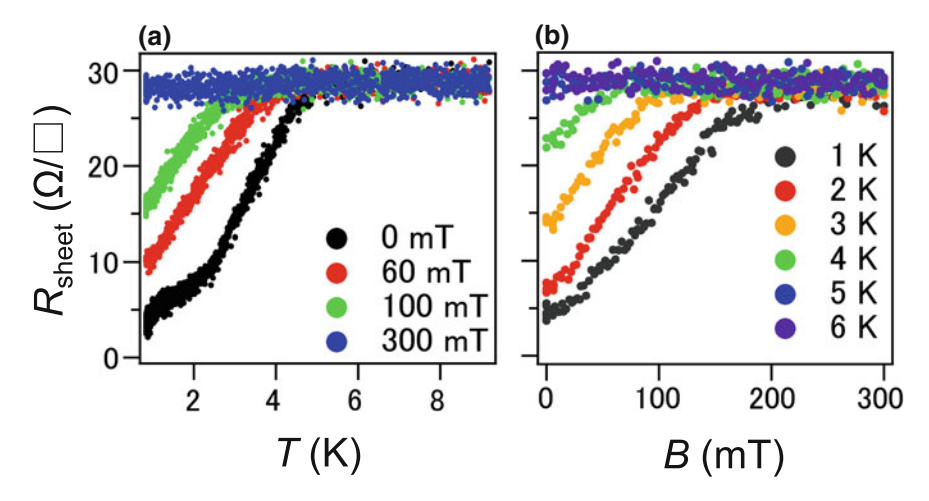
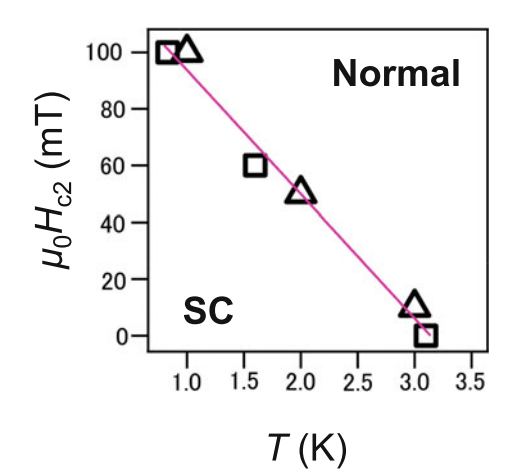


Fig. 6.10 Magnetoresistance of Ca-intercalated bilayer graphene. **a** R_{sheet} of C₆CaC₆ (sample S2) as a function of temperature under different magnetic fields. **b** Same as a as a function of magnetic field for different temperatures. The magnetic field was applied perpendicular to the sample surface

Fig. 6.11 Temperature dependence of the upper critical field $\mu_0 H_{c2}$ obtained from Fig. 6.10 a (squares) and b (triangles). The value of $\mu_0 H_{c2}$ was defined as the magnetic field where $R_{\rm sheet}$ drops to a half of normal-state resistance in a and b. Solid line shows the fit with the Ginzburg-Landau theory Eq. (2.121)



sented that π^* band can also be gapped [44]. Hence, even in C_6CaC_6 , there is a possibility that superconducting gap can be observed in π^* band under the condition that CDW does not appear. Since the CDW is originated from the interference from the buffer layer, free-standing bilayer graphene should be useful, which can be prepared by for example, hydrogen-termination of single-layer graphene on SiC (0001) [45]. Alternatively, in the SiC (0001) surface, that is, the C surface, graphene can be grown without forming the buffer layer. Then, π^* will be opening the gap and T_c is enhanced. Indeed, in Ref. [44], $T_c = 6.8-8.1$ K is predicted.

6.5 Summary

In this study, we fabricated bilayer graphene interlayer compound and observed superconducting transition of $T_c \sim 2$ K on C_6CaC_6 by in situ electrical transport measurements. Decreasing of resistance started from the high temperature side than the transition temperature, which is influence of the amplitude fluctuation, that is, the two-dimensional nature appears qualitatively. On the other hand, the pristine bilayer graphene and C_6LiC_6 showed a weakly localized tendency. The comparison of the superconducting properties among different C_6CaC_6 samples suggests that the superconductivity is derived from $\sqrt{3} \times \sqrt{3}$ —Ca structure and depends on the crystallinity of intercalating Ca atoms. These experimental facts show that even in the bilayer graphene intercalation compound, same as the bulk GIC, ILB needs to be occupied for the superconductivity.

References

- N. Hannay, T. Geballe, B. Matthias, K. Andres, P. Schmidt, D. MacNair, Phys. Rev. Lett. 14, 225 (1965)
- A. Hebard, M. Rosseinky, R. Haddon, D. Murphy, S. Glarum, T. Palstra, A. Ramirez, A. Karton, Nature 350, 600 (1991)
- K. Tanigaki, T. Ebbesen, S. Saito, J. Mizuki, J. Tsai, Y. Kubo, S. Kuroshima, Nature 352(6332), 222 (1991)
- 4. M. Kociak, A.Y. Kasumov, S. Guéron, B. Reulet, I. Khodos, Y.B. Gorbatov, V. Volkov, L. Vaccarini, H. Bouchiat, Phys. Rev. Lett. **86**, 2416 (2001)
- E. Ekimov, V. Sidorov, E. Bauer, N. Mel'Nik, N. Curro, J. Thompson, S. Stishov, Nature 428(6982), 542 (2004)
- 6. R. Barnett, E. Demler, E. Kaxiras, Phys. Rev. B 71, 035429 (2005)
- R.P. Smith, T.E. Weller, C.A. Howard, M.P. Dean, K.C. Rahnejat, S.S. Saxena, M. Ellerby, Phys. C Supercond. Appl. 514, 50 (2015)
- 8. T.E. Weller, M. Ellerby, S.S. Saxena, R.P. Smith, N.T. Skipper, Nature Phys. 1, 39 (2005)
- M. Sutherland, N. Doiron-Leyraud, L. Taillefer, T. Weller, M. Ellerby, S.S. Saxena, Phys. Rev. Lett. 98, 067003 (2007)
- G. Lamura, M. Aurino, G. Cifariello, E. Di Gennaro, A. Andreone, N. Emery, C. Hérold, J.F. Marêché, P. Lagrange, Phys. Rev. Lett. 96(10), 107008 (2006)
- N. Bergeal, V. Dubost, Y. Noat, W. Sacks, D. Roditchev, N. Emery, C. Hérold, J.F. Marêché, P. Lagrange, G. Loupias, Phys. Rev. Lett. 97, 077003 (2006)
- G. Csányi, P. Littlewood, A.H. Nevidomskyy, C.J. Pickard, B. Simons, Nature Phys. 1, 42 (2005)
- S.L. Yang, J. Sobota, C. Howard, C. Pickard, M. Hashimoto, D. Lu, S.K. Mo, P. Kirchmann, Z.X. Shen, Nature Commun. 5 (2014)
- K.S. Novoselov, A.K. Geim, S. Morozov, D. Jiang, Y. Zhang, S. Dubonos, I. Grigorieva, A. Firsov, Science 306, 666 (2004)
- K. Novoselov, A.K. Geim, S. Morozov, D. Jiang, M. Katsnelson, I. Grigorieva, S. Dubonos, A. Firsov, Nature 438, 197 (2005)
- K.S. Novoselov, Z. Jiang, Y. Zhang, S. Morozov, H. Stormer, U. Zeitler, J. Maan, G. Boebinger, P. Kim, A. Geim, Science 315, 1379 (2007)
- 17. C. Lee, X. Wei, J.W. Kysar, J. Hone, Science 321, 385 (2008)

References 113

 K.S. Kim, Y. Zhao, H. Jang, S.Y. Lee, J.M. Kim, K.S. Kim, J.H. Ahn, P. Kim, J.Y. Choi, B.H. Hong, Nature 457, 706 (2009)

- 19. S. Bae, H. Kim, Y. Lee, X. Xu, J.S. Park, Y. Zheng, J. Balakrishnan, T. Lei, H.R. Kim, Y.I. Song et al., Nature Nanotechnol. 5, 574 (2010)
- M. Xue, G. Chen, H. Yang, Y. Zhu, D. Wang, J. He, T. Cao, J. Am. Chem. Soc. 134, 6536 (2012)
- A.P. Tiwari, S. Shin, E. Hwang, S.G. Jung, T. Park, H. Lee, arXiv preprint arXiv:1508.06360 (2015)
- Z.H. Pan, J. Camacho, M. Upton, A. Fedorov, C. Howard, M. Ellerby, T. Valla, Phys. Rev. Lett. 106, 187002 (2011)
- 23. G. Profeta, M. Calandra, F. Mauri, Nature Phys. 8, 131 (2012)
- K. Li, X. Feng, W. Zhang, Y. Ou, L. Chen, K. He, L.L. Wang, L. Guo, G. Liu, Q.K. Xue et al., Appl. Phys. Lett. 103, 062601 (2013)
- 25. A. Bostwick, T. Ohta, T. Seyller, K. Horn, E. Rotenberg, Nature Phys. 3, 36 (2007)
- M. Bianchi, E. Rienks, S. Lizzit, A. Baraldi, R. Balog, L. Hornekær, P. Hofmann, Phys. Rev. B 81, 041403 (2010)
- A. Fedorov, N. Verbitskiy, D. Haberer, C. Struzzi, L. Petaccia, D. Usachov, O. Vilkov, D. Vyalikh, J. Fink, M. Knupfer, et al., Nature Commun. 5 (2014)
- 28. C. Hwang, D.Y. Kim, D.A. Siegel, K.T. Chan, J. Noffsinger, A.V. Fedorov, M.L. Cohen, B. Johansson, J.B. Neaton, A. Lanzara, Phys. Rev. B 90, 115417 (2014)
- B. Ludbrook, G. Levy, P. Nigge, M. Zonno, M. Schneider, D. Dvorak, C. Veenstra, S. Zhdanovich, D. Wong, P. Dosanjh et al., Proc. Natl. Acad. Sci. 112, 11795 (2015)
- K.V. Emtsev, A. Bostwick, K. Horn, J. Jobst, G.L. Kellogg, L. Ley, J.L. McChesney, T. Ohta, S.A. Reshanov, J. Röhrl et al., Nature Mater. 8, 203 (2009)
- 31. S. Lara-Avila, A. Tzalenchuk, S. Kubatkin, R. Yakimova, T. Janssen, K. Cedergren, T. Bergsten, V. Fal'ko, Phys. Rev. Lett. 107, 166602 (2011)
- T. Ohta, A. Bostwick, J.L. McChesney, T. Seyller, K. Horn, E. Rotenberg, Phys. Rev. Lett. 98, 206802 (2007)
- 33. K. Sugawara, K. Kanetani, T. Sato, T. Takahashi, AIP Adv. 1, 022103 (2011)
- 34. K. Kanetani, K. Sugawara, T. Sato, R. Shimizu, K. Iwaya, T. Hitosugi, T. Takahashi, Proc. Natl. Acad. Sci. 109, 19610 (2012)
- 35. R. Shimizu, K. Sugawara, K. Kanetani, K. Iwaya, T. Sato, T. Takahashi, T. Hitosugi, Phys. Rev. Lett. 114, 146103 (2015)
- 36. I. Mazin, A. Balatsky, Philos. Mag. Lett. 90, 731 (2010)
- 37. R. Jishi, D. Guzman, H. Alyahyaei, arXiv preprint arXiv:1107.1845 (2011)
- 38. S. Ichinokura, K. Sugawara, A. Takayama, T. Takahashi, S. Hasegawa, ACS Nano 10(2), 2761 (2016)
- 39. S. Hikami, A.I. Larkin, Y. Nagaoka, Progr. Theor. Phys. **63**, 707 (1980)
- E. McCann, K. Kechedzhi, V.I. Fal'ko, H. Suzuura, T. Ando, B. Altshuler, Phys. Rev. Lett. 97, 146805 (2006)
- 41. N. Emery, C. Hérold, M. d'Astuto, V. Garcia, C. Bellin, J. Marêché, P. Lagrange, G. Loupias, Phys. Rev. Lett. 95, 087003 (2005)
- 42. M. Yamada, T. Hirahara, S. Hasegawa, Phys. Rev. Lett. 110, 237001 (2013)
- 43. R.D. Chaudhari, J.B. Brown, Phys. Rev. 139, A1482 (1965)
- 44. E. Margine, F.G. Henry Lambert, Scient. Rep. 6 (2016)
- 45. K. Sugawara, T. Sato, K. Kanetani, T. Takahashi, J. Phys. Soc. Jpn. 80, 024705 (2011)
- 46. K. Sugawara, T. Sato, T. Takahashi, Nature Phys. 5, 40 (2009)

Chapter 7 Conclusion

Abstract The present study contains three different two-dimensional superconductors described in Chaps. 4–6. This chapter is devoted to sum up them by comparison of the results from a view point of two-dimensional nature and electronic structures, which is experimentally observed by angle resolved photoemission spectroscopy. In the latter half, future perspective is presented, where conceivable idea to develop the field of atomic layer superconductor, believed to be pioneered by the present study.

Keywords Band structure • Two-dimension • Superconductivity

7.1 General Statement

7.1.1 Electronic Structure and Superconductivity

Since the conventional two-dimensional superconductors were amorphous thin films, they do not have well-defined band structure. It becomes possible to discuss the relation between electronic quantum state and the superconducting property by employing single-crystal like epitaxial films on ultraclean semiconductor surfaces. In this study, electrical conduction measurements were intensively performed on systems where metallic band dispersions were confirmed and superconductivity was expected by ARPES, in terms of electron-phonon coupling.

In thallium-based overlayers on Si(111), the Tl biatomic layer (Chap. 4) and the Tl-Pb monatomiclayer compound (Chap. 5), it was found that the metallic states has strong electron-phonon interaction by temperature dependent ARPES measurements. The fact that superconductivity is actually developed in these systems indicates the capability of temperature-dependent ARPES measurements for prediction of the ground state, even if it is out of the available temperature range. Estimation of the transition temperature using the McMillan equation is also effective to discuss the relation between electron-phonon coupling and superconductivity. However, in order to obtain a quantitative agreement with the experimental value, it is necessary to clarify the Debye temperature on the surface by measurement or calculation.

116 7 Conclusion

On the other hand, we had a more qualitative discussion on bilayer graphene intercalation compounds. That is, it was experimentally clarified that the emergence of superconductivity is driven by electron filling of the "interlayer band".

In particular, in the ARPES-transport combined study on the Tl-Pb monatomiclayer compound, coexistence of the Rashba effect and superconductivity was directly evaluated for the first time. Even though the relation between these two ideas has not yet been clarified, it provided us several experimental advantages; First, this material can be grown easily with usual MBE equipment. Second, both the superconducting gap and the energy of the Rashba effect are accessible by various experimental methods, promising for a breakthrough in the near future.

7.1.2 Two-Dimensionality

In all the superconducting transitions observed in this study, a decrease in resistance was observed from a temperature higher than $T_{\rm c}$. This is thought to be the influence of the amplitude fluctuation, originated from low dimensionality. In the Tl-Pb alloy, quantitative agreement was obtained by numerical fitting with the Eq. (2.139), which is based on theories by Aslamazov-Larkin and Maki-Thompson. In the bilayer Tl, the resistance curve was reproduced by incorporating the localization effect in addition to Aslamazov-Larkin term.

As an influence of phase fluctuation, a "tail" near zero resistance was also observed in each material, which is thought to be the resistance due to the magnetic flux generated by the decoupled vortex pairs, in accordance with the Berezinskii-Kosterlitz-Thouless (BKT) mechanism. For both Tl-based surface structures, least-square fitting worked well by Halperin-Nelson equation Eq. (2.141). In the Tl-Pb compound, $V \propto I^3$ was also found in the current-voltage characteristics near the BKT transition temperature by the H-N fitting. However, it was not a clear signal since it was almost buried in noise. A problem remains in the measurement accuracy in the low bias region.

With the Ca-intercalated bilayer graphene, we could obtained quantitative agreement with the data and the theories above. This may be because superconducting transition is broaden by non-superconductive region, which is unintentionally remained even after the intercalation process.

Another phenomena typical for two-dimensional system is superconductor-insulator transition (SIT). Among the three system, only the biatomic-layer Tl showed the magnetic field induced SIT. This is because it is a dirty superconductor which has a normal state resistivity close to the quantum critical point, while Tl-Pb alloy and C_6CaC_6 have much lower ones. In Tl bilayer, the SIT was intermediated by a metallic behavior. Such a state has been observed in a ultrathin flakes of NbSe₂ [1] and ionic liquid gated ZrNCl [2]. Since they have single crystaline, it has been claimed that metallic state requires good crystallinity and low normal resistance. This is inconsistent to the present result. The origin of the metallic state is still open question and Tl bilayer should be an example to activate the discussion.

7.2 Outlook

The three materials found to have superconductivity are expected to show lots of exotic phenomena in terms of lack of symmetry and the unique Fermi surface topologies. Although the electrical transport measurement with application of out-of-plane magnetic field is the simplest test on unidentified superconductors, it is insufficient to detect detailed properties of the superconductivity. Further studies from different aspects are required. The direct measurement of the superconducting gap by spectroscopic technique gives the information of binding mechanism in Cooper pair formation. At least, it is expected to appear the influence of strong electron-phonon interaction. The most suitable option is ultralow-temperature STM/S at present, which is used for demostration of the complex mechanism to develop high-temperature superconductivity in such as the cuprates. From the wavenumber-integrated spectrum, we can discuss the anisotropy of superconducting gap function, the background conductance, the dip-hump feature above the gap, the zero-bias conductance peak and spatial homogeneity. It is interesting to observe the superconducting gap of Tl-Pb alloy, which has two-couples of spin splitting Fermi surfaces, possibly to show a mixed superconducting state of spin singlet and triplet components.

Investigation of deeper insight in those superconductivity requires developing of novel vacuum systems. ARPES is the most direct experimental device to see the structure of the Fermi surface, including superconducting gap resolved in wavenumber space. However, compare to STM, ARPES system has less compatibility with cryostat. There are quite limited groups to achieve the PES measurement at several kelvin in the world. As far as the $T_{\rm c}$ in the target superconducting system is comparable to the accessible temperature, we have to wait for the further improvement of low-temperature ARPES. Applying in-plane magnetic field is another experimental challenge to probe the electromagnet response resulting from the unusual Fermi surface texture. It is possible to convert the superconducting magnet inside a bath cryostat from single axis model to multiple axis one. However, the in-plane axis capability of such vector magnet is only about 1 T, which is much smaller than the paramagnetic limit of the Cooper pair in the Tl-Pb compound or C_6CaC_6 . So it is more effective to change the direction of sample, to be applied in-plane magnetic field by superconducting solenoid.

The superconducting material systems in this theses are based on semiconductor substrates such as silicon and its carbide. This is an advantage towards not only devise application but also high-temperature superconductivity in terms of electron-phonon coupling because the semiconductors have high Debye temperature. So as a matter of the extension of material engineering in this study, I would like to propose to import various carbon nanostructures. First, graphene is still promising platform of superconductivity with abundant physics and possible transition at a high-temperature by its remarkable Debye temperature of 2800 K [3]. As mentioned in Sect. 6.1.2, doping of alkali metal is thought to be effective to induce superconductivity in graphene while bulk graphite and the bilayer graphene in this study have a high transition temperature when Ca atoms are intercalated. In order to solve this contradiction,

118 7 Conclusion

systematic study should be performed on single- to several-layer graphene about alkali-metal-modification to the crystal structure, electron state and electrical transport property. According to a previous study [4], it is possible to dope K and Ca to both side of graphene. Then, an extended van Hove singularity occurs at the Fermi surface. Although this measurement was performed at room temperature, it predicts superconductivity driven by the direct Coulomb interaction at low temperature. Other nano-allotropes, fullerene and carbon nanotube have been already reported to be superconductivity by doping, as 3D crystalized fullerene [5, 6] and aggregate of nanotube [7], respectively. By using the growth technique in UHV, it seems possible to promote their self-assembling into a form of well defined 2D network on substrates and dope the alkali metals without contamination by air. Superconductivity in such 2D systems are challenging subject. Diamond, a 3D bulk crystal of carbon is also interesting. In the case of diamond, it can be used as a substrate instead of silicon. It is pointed out that superconductivity in surface epitaxial thin films is affected by phonons of the substrate [8]. Diamond has been expected to be high-temperature bulk superconductor for a long time due to its Debye temperature of 2200 K. Therefore, its surface should provide an opportunity to glow novel superconducting 2D structure. For example, the Rashba effect can coexist if adsorption of heavy metal seems possible.

As other effect of substrate, charge transfer etc. are well known to affect superconducting properties. In other words, *interface* plays important role. Interfacial superconductivity is already attracts considerable attention in oxide systems [9]. *Surface* superconductivity has a lot of overlapping idea with it. For the device application, surface superconductor has to be protected by some capping material to be put out from vacuum chamber. I propose that surface superconductors should be regarded as a beginning of interfacial designning to be buried in material. Such build-in interface superconductors is able to be investigated by bulk-measurement system including magnetization measurement and ultra-high magnetic fields generated by pulse system. Here, *interface* is not limited to hetero junction of solids. Considering the recent development of ionic liquid engineering, liquid-solid interface has unexplored potential for material science.

This research is an example showing that macroscopic physical properties are developed from nanotechnological engineering. I believe that superconductivity with high transition temperature and critical magnetic field will be realized by further refinement in the future.

References

- A. Tsen, B. Hunt, Y. Kim, Z. Yuan, S. Jia, R. Cava, J. Hone, P. Kim, C. Dean, A. Pasupathy, Nature Phys. (2015)
- 2. Y. Saito, Y. Kasahara, J. Ye, Y. Iwasa, T. Nojima, Science 350, 409 (2015)
- 3. M.S. Fuhrer, Physics **3**, 106 (2010)
- J.L. McChesney, A. Bostwick, T. Ohta, T. Seyller, K. Horn, J. González, E. Rotenberg, Physical review letters 104(13), 136803 (2010)

References 119

 A. Hebard, M. Rosseinky, R. Haddon, D. Murphy, S. Glarum, T. Palstra, A. Ramirez, A. Karton, Nature 350, 600 (1991)

- K. Tanigaki, T. Ebbesen, S. Saito, J. Mizuki, J. Tsai, Y. Kubo, S. Kuroshima, Nature 352(6332), 222 (1991)
- M. Kociak, A.Y. Kasumov, S. Guéron, B. Reulet, I. Khodos, Y.B. Gorbatov, V. Volkov, L. Vaccarini, H. Bouchiat, Phys. Rev. Lett. 86, 2416 (2001)
- 8. L. Wang, X. Ma, Q.K. Xue, Supercond. Sci. Technol. 29(12), 123001 (2016)
- 9. N. Reyren, S. Gariglio, A. Caviglia, D. Jaccard, T. Schneider, J. Triscone, Appl. Phys. Lett. 94, 112506 (2009)

Curriculum Vitae

Satoru Ichinokura

Department of Physics, University of Tokyo 7-3-1 Hongo Bunkyo-ku, Tokyo 113-0033 Japan

Email: ichinokura@surface.phys.s.u-tokyo.ac.jp¹

Appointments

JSPS Post-doctoral Researcher, National Institute for Materials Science (Apr. 2017–)

Prof. Takashi Uchihashi

JSPS Post-doctoral Researcher, University of Tokyo (Apr. 2016–)

Prof. Shuji Hasegawa

Education

Doctor of Philosophy (Ph.D.) in Physics, University of Tokyo (2013–2016), advisors Prof. Shuji Hasegawa

Master of Science (MSc) in Physics, Tohoku University (2011–2013) Bachelor of Science (BSc) in Physics, Tohoku University (2007–2011)

Teaching

Technical assistant of experiment training for bachelor students at Tohoku university (2011–2012)

Technical assistant of experiment training for bachelor students at University of Tokyo (2014–2015)

International Center for Materials Nanoarchitectonics, National Institute for Materials Science 1-1, Namiki, Tsukuba, Ibaraki 305-0044, Japan Email: ICHINOKURA.Satoru@nims.go.jp.

¹Present address:

[©] Springer Nature Singapore Pte Ltd. 2018

122 Curriculum Vitae

Awards

Tohoku University GCOE Research Grant (April 2012–March 2013)

Travel award from Surface Science Society of Japan (November 2014)

Student award from Surface Science Society of Japan (May 2015)

JSPS Research fellowship for young scientists (April 2015–March 2017)

Graduate School of Science award from School of Science, The University of Tokyo (March 2016)

Presentation award from Surface Science Society of Japan (April 2016)

JSPS Research fellowship for young scientists (April 2017–)

Research Interests

Research field: surface physics & nanotechnology

Physical interests: low-temperature & low-dimensional physics, superconductivity, spintoronics

Target materials: semiconductors & its metal-induced surface reconstructions, atomic-scale thin layer systems such as graphene & transition metal dichalcogenides

Experimental techniques: electrical transport measurements & scanning tunneling microscopy under ultralow temperature & high magnetic field